Computational modelling of Nematic liquid crystal defects in devices and fiber processing

Gino De Luca

Doctor of Philosophy

Department of Chemical Engineering

McGill University

Montreal, Quebec, Canada

September 2007

A thesis submitted to the Faculty of Graduate and Postdoctoral Studies in partial fulfillment of the requirements for the degree of Doctor of Philosophy

Your file Votre référence
ISBN: 978-0-494-38580-7
Our file Notre référence
ISBN: 978-0-494-38580-7

DEDICATION

To my parents,

for their unconditional support throughout the years

CONTRIBUTIONS OF THE AUTHOR

I, Gino De Luca, the author of this dissertation choose the manuscript-based thesis option according to the guidelines for thesis preparation given by the faculty of graduate studies and research of McGill University. Contents of chapters 2 to 7 of the present thesis are adopted or revised from published papers that have been published in scientific journals under the normal supervision of my research supervisor Professor Alejandro D. Rey, who is also a co-author. In Chapter 2, all the experimental work was done by our collaborators at the Georgia Institute of Technology who are co-authors of the corresponding paper.

COPYRIGHT CLEARANCE

I, Alejandro D. Rey, hereby give copyright clearance of the papers I co-authored with Gino De Luca for usage in is doctoral thesis. The *extent of my contribution* to the following manuscripts is that of a research director. I provided general research directions and supervision throughout the duration of this Ph.D. thesis.

Chapter 2: *Microscopic observations and simulations of Bloch walls in nematic thin films*, Jian Zhou, Jung O. Park, G. De Luca, Alejandro D. Rey, and Mohan Srinivasarao, Physical Review Letters, 97(15), (2006)

Chapter 3: *Modelling of Bloch inversion wall defects in nematic thin films*, G. De Luca, A.D. Rey, Modelling and Simulation in Materials Science and Engineering, 14(8), (2006)

Chapter 4: *Dynamic interactions between nematic point defects in the spinning extrusion duct of spiders*, G. De Luca, A.D. Rey, The Journal of Chemical Physics, 124(14), (2006); Also selected by the Virtual Journal of Biological Physics Research, 11(8), (2006)

Chapter 4: *Biomimetics of spider silk spinning process*, G. De Luca, A.D. Rey, Design and Nature III, C.A. Brebbia, WIT Press IBT Global, London, 127-136 (2006), ISSN: 1743-3541 & ISBN: 1-84564-166-3

Authorization from: *Physical Review Letters* (American Physical Society), Chapter 2.

As the author, can I include my article or a portion of my article in my thesis or dissertation?

Yes, the author has the right to use the article or a portion of the article in a thesis or dissertation without requesting permission from APS, provided the bibliographic citation and the APS copyright credit line are given on the appropriate pages.

http://forms.aps.org/author/copyfaq.html

Authorization from: *The Journal of Chemical Physics* (American Institute of Physics), Chapter 4.

AMERICAN INSTITUTE OF PHYSICS LICENSE TERMS AND CONDITIONS

May 30, 2007

This is a License Agreement between Gino De Luca ("You") and American Institute of Physics ("American Institute of Physics"). The license consists of your order details, the terms and conditions provided by American Institute of Physics, and the payment terms and conditions.

License Number: 1718841246918
License date: May 30, 2007
Licensed content publisher: American Institute of Physics
Licensed content title: Dynamic interactions between nematic point defects in the spinning extrusion duct of spiders
Licensed content author: Gino De Luca and Alejandro D. Rey
Type of Use: Republish Entire Article
Requestor Type: Author
Title of your work: PhD Thesis
Publisher of your work: McGill University
Publication date of your work: 07/01/2007
American Institute of Physics -- Terms and Conditions: Permissions Uses

American Institute of Physics ("AIP") hereby grants to you the non-exclusive right and license to use and/or distribute the Material according to the use specified in your order, on a one-time basis, for the specified term, with a maximum distribution equal to the number that you have ordered. Any links or other content accompanying the Material are not the subject of this license.

1. You agree to include the following copyright and permission notice with the reproduction of the Material: "Reprinted with permission from [FULL CITATION]. Copyright [PUBLICATION YEAR], American Institute of Physics." For an article, the copyright and permission notice must be printed on the first page of the article or book chapter. For photographs, covers, or tables, the copyright and permission notice may appear with the Material, in a footnote, or in the reference list.
2.If you have licensed reuse of a figure, photograph, cover, or table, it is your responsibility to ensure that the material is original to AIP and does not contain the copyright of another entity, and that the copyright notice of the figure, photograph, cover, or table does not indicate that it was reprinted by AIP, with permission, from another source. Under no circumstances does AIP, purport or intend to grant permission to reuse material to which it does not hold copyright.
3.You may not alter or modify the Material in any manner. You may translate the Material into another language only if you have licensed translation rights. You may not use the Material for promotional purposes. AIP reserves all rights not specifically granted herein.
4.The foregoing license shall not take effect unless and until AIP or its agent, Copyright Clearance Center, receives the Payment in accordance with Copyright Clearance Center Billing and Payment Terms and Conditions, which are incorporated herein by reference.
5.AIP or the Copyright Clearance Center may, within two business days of granting this license, revoke the license for any reason whatsoever, with a full refund payable to you. Should you violate the terms of this license at any time, AIP, American Institute of Physics or Copyright Clearance Center may revoke the license with no refund to you. Notice of such revocation will be made using the contact information provided by you. Failure to receive such notice will not nullify the revocation.
6. AIP makes no representations or warranties with respect to the Material. You agree to indemnify and hold harmless AIP, American Institute of Physics, and their officers, directors, employees or agents from and against any and all claims arising out of your use of the Material other than as specifically authorized herein.
7.The permission granted herein is personal to you and is not transferable or assignable without the prior written permission of AIP. This license may not be amended except in a writing signed by the party to be charged.
8.If purchase orders, acknowledgments or check endorsements are issued on any forms containing terms and conditions which are inconsistent with these provisions, such inconsistent terms and conditions shall be of no force and effect. This document, including the CCC Billing and Payment Terms and Conditions, shall be the entire agreement between the parties relating to the subject matter hereof.

This Agreement shall be governed by and construed in accordance with the laws of the State of New York. Both parties hereby submit to the jurisdiction of the courts of New York County for purposes of resolving any disputes that may arise hereunder.

Authorization from: *The Journal of Chemical Physics* (American Institute of Physics), Chapter 6.

AMERICAN INSTITUTE OF PHYSICS LICENSE TERMS AND CONDITIONS

May 30, 2007

This is a License Agreement between Gino De Luca ("You") and American Institute of Physics ("American Institute of Physics"). The license consists of your order details, the terms and conditions provided by American Institute of Physics, and the payment terms and conditions.

License Number: 1718841093387

License date: May 30, 2007
Licensed content publisher: American Institute of Physics

Licensed content title: Ringlike cores of cylindrically confined nematic point defects
Licensed content author: Gino De Luca and Alejandro D. Rey
Type of Use: Republish Entire Article
Requestor Type: Author
Title of your work: PhD Thesis
Publisher of your work: Mc Gill University
Publication date of your work: 07/01/2007
American Institute of Physics -- Terms and Conditions: Permissions Uses

American Institute of Physics ("AIP") hereby grants to you the non-exclusive right and license to use and/or distribute the Material according to the use specified in your order, on a one-time basis, for the specified term, with a maximum distribution equal to the number that you have ordered. Any links or other content accompanying the Material are not the subject of this license.

1. You agree to include the following copyright and permission notice with the reproduction of the Material: "Reprinted with permission from [FULL CITATION]. Copyright [PUBLICATION YEAR], American Institute of Physics." For an article, the copyright and permission notice must be printed on the first page of the article or book chapter. For photographs, covers, or tables, the copyright and permission notice may appear with the Material, in a footnote, or in the reference list.
2.If you have licensed reuse of a figure, photograph, cover, or table, it is your responsibility to ensure that the material is original to AIP and does not contain the copyright of another entity, and that the copyright notice of the figure, photograph, cover, or table does not indicate that it was reprinted by AIP, with permission, from another source. Under no circumstances does AIP, purport or intend to grant permission to reuse material to which it does not hold copyright.
3.You may not alter or modify the Material in any manner. You may translate the Material into another language only if you have licensed translation rights. You may not use the Material for promotional purposes. AIP reserves all rights not specifically granted herein.
4.The foregoing license shall not take effect unless and until AIP or its agent, Copyright Clearance Center, receives the Payment in accordance with Copyright Clearance Center Billing and Payment Terms and Conditions, which are incorporated herein by reference.
5.AIP or the Copyright Clearance Center may, within two business days of granting this license, revoke the license for any reason whatsoever, with a full refund payable to you. Should you violate the terms of this license at any time, AIP, American Institute of Physics or Copyright Clearance Center may revoke the license with no refund to you. Notice of such revocation will be made using the contact information provided by you. Failure to receive such notice will not nullify the revocation.
6. AIP makes no representations or warranties with respect to the Material. You agree to indemnify and hold harmless AIP, American Institute of Physics, and their officers, directors, employees or agents from and against any and all claims arising out of your use of the Material other than as specifically authorized herein.
7.The permission granted herein is personal to you and is not transferable or assignable without the prior written permission of AIP. This license may not be amended except in a writing signed by the party to be charged.
8.If purchase orders, acknowledgments or check endorsements are issued on any forms containing terms and conditions which are inconsistent with these provisions, such inconsistent terms and conditions shall be of no force and effect. This document, including the CCC Billing and Payment Terms and Conditions, shall be the entire agreement between the parties relating to the subject matter hereof.

This Agreement shall be governed by and construed in accordance with the laws of the State of New York. Both parties hereby submit to the jurisdiction of the courts of New York County for purposes of resolving any disputes that may arise hereunder.

Authorization from: *The Journal of Chemical Physics* (American Institute of Physics), Chapter 7.

AMERICAN INSTITUTE OF PHYSICS LICENSE TERMS AND CONDITIONS

May 30, 2007

This is a License Agreement between Gino De Luca ("You") and American Institute of Physics ("American Institute of Physics"). The license consists of your order details, the terms and conditions provided by American Institute of Physics, and the payment terms and conditions.

License Number: 1787230030930
License date: Sep 13, 2007
Licensed content publisher: American Institute of Physics

Licensed content title: Point and ring defects in nematics under capillary confinement
Licensed content author: Gino De Luca and Alejandro D. Rey
Type of Use: Republish Entire Article
Requestor Type: Author
Title of your work: PhD Thesis
Publisher of your work: McGill University
Publication date of your work: 07/01/2007
American Institute of Physics -- Terms and Conditions: Permissions Uses

American Institute of Physics ("AIP") hereby grants to you the non-exclusive right and license to use and/or distribute the Material according to the use specified in your order, on a one-time basis, for the specified term, with a maximum distribution equal to the number that you have ordered. Any links or other content accompanying the Material are not the subject of this license.

1. You agree to include the following copyright and permission notice with the reproduction of the Material: "Reprinted with permission from [FULL CITATION]. Copyright [PUBLICATION YEAR], American Institute of Physics." For an article, the copyright and permission notice must be printed on the first page of the article or book chapter. For photographs, covers, or tables, the copyright and permission notice may appear with the Material, in a footnote, or in the reference list.
2.If you have licensed reuse of a figure, photograph, cover, or table, it is your responsibility to ensure that the material is original to AIP and does not contain the copyright of another entity, and that the copyright notice of the figure, photograph, cover, or table does not indicate that it was reprinted by AIP, with permission, from another source. Under no circumstances does AIP, purport or intend to grant permission to reuse material to which it does not hold copyright.
3.You may not alter or modify the Material in any manner. You may translate the Material into another language only if you have licensed translation rights. You may not use the Material for promotional purposes. AIP reserves all rights not specifically granted herein.
4.The foregoing license shall not take effect unless and until AIP or its agent, Copyright Clearance Center, receives the Payment in accordance with Copyright Clearance Center Billing and Payment Terms and Conditions, which are incorporated herein by reference.
5.AIP or the Copyright Clearance Center may, within two business days of granting this license, revoke the license for any reason whatsoever, with a full refund payable to you. Should you violate the terms of this license at any time, AIP, American Institute of Physics or Copyright Clearance Center may revoke the license with no refund to you. Notice of such revocation will be made using the contact information provided by you. Failure to receive such notice will not nullify the revocation.
6. AIP makes no representations or warranties with respect to the Material. You agree to indemnify and hold harmless AIP, American Institute of Physics, and their officers, directors, employees or agents from and against any and all claims arising out of your use of the Material other than as specifically authorized herein.
7.The permission granted herein is personal to you and is not transferable or assignable without the prior written permission of AIP. This license may not be amended except in a writing signed by the party to be charged.
8.If purchase orders, acknowledgments or check endorsements are issued on any forms containing terms and conditions which are inconsistent with these provisions, such inconsistent terms and conditions shall be of no force and effect. This document, including the CCC Billing and Payment Terms and Conditions, shall be the entire agreement between the parties relating to the subject matter hereof.

This Agreement shall be governed by and construed in accordance with the laws of the State of New York. Both parties hereby submit to the jurisdiction of the courts of New York County for purposes of resolving any disputes that may arise hereunder.

ACKNOWLEDGMENTS

First of all, I wish to thank my research supervisor, Professor Alejandro D. Rey, for his confidence and for giving me the opportunity to pursue graduate studies at McGill University. I would also like to thank him very much for his constant encouragement, interest and support throughout the completion of this Ph.D. thesis. I will always be indebted for what I learnt from him about dedication and perseverance in research.

I am also thankful to the Natural Science and Engineering Research Council of Canada and the Department of Chemical Engineering of McGill University for their financial support without which the completion of this Ph.D. would not have been possible.

I would also like to extend my appreciation to the following people:

- Benjamin Wincure with whom I had regular conversations on 'research' and who often helped me clarifying and expressing ideas and concepts.
- My research group colleagues for providing an everyday peaceful and enjoyable workplace and also for all the pleasant time and discussions we had during our occasional get-togethers. I wish them all great success in their future.
- My family and friends for their constant and indispensable support, encouragement and understanding.

ABSTRACT

This thesis uses multiscale computational modelling to find the fundamental principles that govern defects forming during the operation of new electro-optical devices and the processing of spider silk fibers. The generalized approach developed in this thesis bridges engineering devices and biological processes based on liquid crystalline materials.

Three types of defects are encountered: inversion walls, lines and points. Inversion wall defects are found in the electro-optical device when a nematic thin film undergoes a temperature-induced surface anchoring transition. Point defects naturally occur in the tubular extrusion duct of spiders, while line defects present close topological connections with point defects and are widespread in many high-performance industrial fibers. Three models are used in this thesis and their usage is dependent on the characteristics of the defects studied.

In the case of inversion wall defects, computational modelling is used to verify, complement and analyze experimental measurements made with fluorescence confocal polarizing microscopy by our collaborator at the Georgia Institute of Technology. The various simulation results agree and explain very well experimental observations and provide a thorough understanding of the wall defects behavior. A computational technique is developed to enable the precise determination of the interaction between the liquid crystal and the device substrate. Understanding the behavior of wall defects and estimating interfacial properties are indispensable to the development and optimization of the electro-optical device as they affect properties like temperature

of operation, switching voltages and response time.

Computational modelling is also used to investigate the behavior of nematic point defects confined in cylindrical cavities as observed along spiders' spinning apparatus, and to examined textural connections with other well know structures seen in industrial fibers. The various scenarios investigated include: interactions between point defects, topological transformations between point, line and ring defects as well as interactions between ring defects. The simulation results agree and complement previous investigations but also offer a new fundamental understanding on the nature and stability of defects in cylindrical cavities. Understanding the behavior of nematic point and line defects in cylindrical geometries is important as they play a fundamental role in the processing of natural and industrial high-performance fibers.

ABRÉGÉ

Cette thèse emploie la modélisation multi-échelles par ordinateur pour trouver les principes fondamentaux qui gouvernent les défauts se formant durant l'utilisation de nouveaux appareils électro-optiques et le traitement de fibres de soie d'araignées. L'approche généralisée développée dans cette thèse connecte les dispositifs d'ingénierie et les procédés biologiques au travers des matériaux liquides cristallins.

Trois types de défauts sont rencontrés : parois d'inversions, lignes et points. Les parois d'inversions sont retrouvés dans les dispositifs électro-optiques quand un fin film nématique subie une transition de température à sa surface. Les défauts points surviennent naturellement dans le canal d'extrusion tubulaire des araignées tandis que les défauts lignes, présentent de proches connexions topologiques avec les défauts points et sont répandus dans de nombreuses fibres industrielles à hautes performances. Trois modèles sont utilisés dans cette thèse et leur usage dépend des caractéristiques des défauts étudiés.

Dans le cas des défauts parois d'inversions, la modélisation par ordinateur est utilisée pour vérifier, complémenter et analyser des mesures expérimentales faite en microscopie confocale à fluorescence polarisée par nos collaborateurs à l'institut de Technologie de Géorgie. Les différents résultats de simulations sont en accord et expliquent très bien les observations expérimentales et fournissent une compréhension approfondie du comportement des défauts parois. Une nouvelle technique de calcul est développée pour permettre la détermination précise de l'interaction entre le cristal liquide et le substrat du dispositif. Comprendre le comportement des défauts

parois et estimer les propriétés interfaciales sont indispensable au développement et à l'optimisation du dispositif électro-optique tandis qu'ils affectent des propriétés tel que la température d'usage, les tensions de changement d'états et les temps de réponses.

La modélisation par ordinateur est aussi utilisée pour étudier le comportement des défauts points confinés dans des cavités cylindriques tel qu'observé le long de l'appareil de filage des araignées, et pour examiner les connections texturales avec d'autres structures observées dans les fibres industrielles. Les différents scenarios étudiés comprennent: les interactions entre défauts points, les transformations topologique entre les défauts points, lignes et annulaires ainsi que les interactions entre les défauts annulaires. Les résultats de simulations sont en accord et complémentent les investigations précédentes mais offrent aussi une nouvelle compréhension fondamentale sur la nature et la stabilité des défauts dans les cavités cylindriques. Comprendre le comportement des défauts points et lignes dans les géométries cylindriques est important étant donné que ces derniers jouent un rôle fondamentale dans le traitement des fibres haute-performances naturelles et industrielles.

TABLE OF CONTENTS

LIST OF FIGURES

CHAPTER 1
General introduction

1.1 Scope of the thesis

Nematic liquid crystals are functional materials used in various electro-optical devices such as displays and light valves whose functionality depends on the substrate-liquid crystal interface [1, 2]. Continuous demand to increase the performance-to-price ratio drives the intense research to unravel the principles that control the interactions between the devices' substrate and the liquid crystal. These interactions can be regulated by temperature, chemistry, and interface topography [1,2]. In many instances, temperature changes in interfacial conditions lead to changes in the nematic liquid crystal molecular orientation and to the concomitant generation and trapping of defects and textures [3, 4]. These defects and textures in turn change the optical characteristics of the electro-optical device and hence predicting when and how they nucleate and behave is an integral part of development and optimization. In addition, when generated under certain controlled conditions, these defects and textures can be used to characterize the physical interactions between the liquid crystal and the substrate [5–10]. Knowing these interactions is necessary to tune the various characteristics of the device (e.g. functioning voltage, response time, etc.). The measurement of these interactions usually requires the determination of an experimental signal in conjunction with an accurate model equation. Inaccurate model equations lead to inaccurate interaction values. In this thesis, we use computer modelling and

simulations to study defects and textures occurring in a nematic liquid crystal-based system whose geometry, boundaries, temperature and material conditions, replicate an experimental setup aimed at the development of a new nematic thin film used in an electro-optical device. The simulation results are validated with experimental data through an external collaboration. Additionally, a new accurate computational technique to quantify the liquid crystal-substrate interaction is proposed.

Nematic liquid crystals are also widely used as structural precursor materials in the manufacturing of high performance fibers, such as Kevlar and carbon fibers [11–14]. Continuous incentive due to environmental restrictions as well as the evolution of green manufacturing has fueled the search for material production systems that avoid high temperature and corrosive solvents. Biomimetics, or systematic technology transfer from nature to engineering, is being used around the world to search for new technologies and processing methods to manufacture super-fibers like Kevlar using aqueous solvents and room temperature. Spider silk biospinning has been considered for some time a natural material manufacturing system that provides the basis for green fiber manufacturing [15–21]. Large efforts to understand, mimic, and use the protein chemistry of the spider silk precursors have been made [17, 22]. On the other hand, the engineering fiber manufacturing principles embedded in the silk biospinning process remain poorly understood [15,18,23,24]. It is well-known that the spider silk precursor becomes a liquid crystalline material during the early extrusion process [11, 15, 16, 19–30]. The emergence of the liquid crystalline state is considered to be an essential feature that leads to a super-tough and strong silk fiber. The liquid crystal silk precursor forms under the severe constraints of narrow and highly

curved micron-sized capillary ducts that feed the fiber spinning apparatus. The interactions between the liquid crystal and the wall of the narrow capillary lead to characteristic defects and textures, detectable by optical microscopy [18,21,23,24,27, 28]. These optical measurements provide significant additional evidence on the state of the spider silk precursor. It is widely believed that the presence of these defects and textures play a crucial role in delaying premature solidification due to high alignment in the liquid crystal state. Currently, the emergence, character and stability of these spider silk's textures in the capillary duct remain poorly understood. This thesis presents a systematic computational study of the nature, emergence, and stability of these textures arising in spider silk precursors. In addition, various topological transformations occurring between the textures observed in other nematic-based high performance fibers are examined. The simulations are validated through the open biological, physical, chemical, and mathematical literature. The results offer new knowledge on nematic texturing in cylindrical capillaries and should be useful to synthetic fiber spinning technology.

Overall, this thesis offers an integrated view of how defects and textures play a crucial role in the operation and processing of systems involving nematic liquid crystals, in flat and curved interfaces as well as in melt and in solution states.

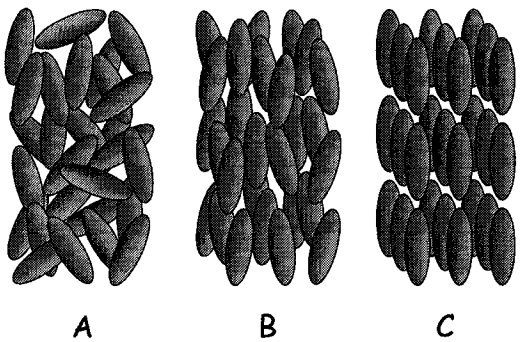

Figure 1–1: Schematic arrangements of molecules in an isotropic liquid (A), a liquid crystal (B) and solid crystal (C).

1.2 Background on liquid crystals

1.2.1 What are liquid crystals?

The term liquid crystals may at first sound both intriguing and confusing. While it appears somehow self-contradictory, the designation is really an attempt to describe particular states or phases of matter that are of great scientific and technological importance today.

The difference between crystals and liquids, the two most common condensed matter phases, is that the molecules in a crystal are ordered whereas in a liquid they are not. The order in a crystal is usually both positional and orientational, in that the molecules are constrained both to occupy specific lattice sites and to point their molecular axes in specific directions. The molecules in liquids, on the other hand, do not display any long range order. Interestingly, many phases with more order than present in liquids but less order than in crystals also exist in nature. Some of these intermediate phases or mesophases are called liquid crystals, since they share properties normally associated with both liquids and crystalline solids [2–4].

The molecules in all liquid crystal mesophases flow much like the molecules of a liquid, but they maintain some degree of orientational order and sometimes some positional order too. Figure 1–1 illustrates the order in the liquid, liquid crystal and solid phases. The amount of order in a liquid crystal is quite small as compared to a crystal. Indeed, there is only a slight tendency for the molecules to point more in one direction rather than others or to spend more time in various positions than others. Yet this small amount of order renders liquid crystal mesophases anisotropic (their physical properties differ from one direction to another). It is this combination of liquid-like fluidity and solid-like anisotropy that makes liquid crystal mesophases an important phase of matter both scientifically and technologically [2–4].

1.2.2 Discovery of liquid crystals

The discovery of liquid crystals is usually attributed to the Austrian Scientist Friederich Reinitzer. In 1888, he experimented with a substance related to cholesterol and noted that it had two melting points. At 145.5°C it melted from a solid to a cloudy liquid and at 178.50°C it turned into a clear liquid. He also observed some unusual color behavior upon cooling; first a pale blue color appeared as the clear liquid turned cloudy and a second bright-blue violet color was present as the cloudy liquid crystallized. Reinitzer sent samples of its substance to Otto Lehmann, a professor of natural philosophy (physics) in Germany. Lehmann was one of the people studying the crystallization properties of various substances and Reinitzer wondered whether what he observed was related to what Lehmann was reporting. Lehmann had constructed a polarizing microscope with a stage on which he could

precisely control the temperature of his samples. This instrument allowed him to observe the crystallization of the sample under controlled conditions. Lehmann observed Reinitzer's substance with his microscope and noted its similarity to some of his samples. He first referred to them as soft crystals; later he used the term crystalline fluids. As he became more convinced that the opaque phase was a uniform phase of matter sharing both properties of liquids and solids, he began to call them liquid crystals [2–4].

1.2.3 The different type of liquid crystals

Many different types of liquid crystals have been identified since the discovery of the first mesophase by Reinitzer and Lehmann and their classification is itself a field of research in constant evolution. Liquid crystals can however be classified according to i) what triggers their emergence, ii) to the nature of their building-blocks, called mesogens, and iii) to their organizations or structures.

Liquid crystals are generally classified as either thermotropics or lyotropics. Thermotropic liquid crystals emerge from pure chemical systems and their order is primarily affected by changes in the temperature. On the other hand, lyotropic liquid crystals are multi-component systems which exhibit their mesomorphic behaviour as the concentration of one or more of their components is varied.

Various types of molecules can form liquid crystal phases. What they all have in common is that they are anisotropic. Either their shape is such that one of their molecular axis is very different from the other two or in some cases different parts of the molecules have different solubility properties. In either case, the

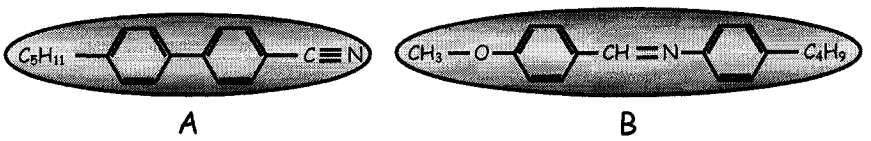

Figure 1–2: Typical rod-like mesogens. (A) p-pentyl-p'-cyanobiphenyl (5CB) and (B) n-(p-methoxybenzylidene)-p-butylaniline (MBBA).

interactions between these anisotropic molecules promote orientational order and sometimes positional order in an otherwise fluid phase. Basically, liquid crystal phase-forming systems may be composed of small organic molecules, of polymers or of amphiphiles [2–4].

Liquid crystals made from small organic molecules. Systems of small organic molecules forming liquid crystal phases usually belong to the class of thermotropics. The most common type of molecules that form liquid crystal phases is a rod-shaped molecule (i.e., one molecular axis is much longer than the other two). Such rod-like compounds are called calamitic liquid crystals. It is important that the molecules be fairly rigid for at least some portion of their length, since they must maintain an elongated shape in order to produce interactions that favor alignment [2, 31, 32]. Figures 1–2(a) and 1–2(b) give the chemical structures of two common rod-like molecules called p-pentyl-p'-cyanobiphenyl (5CB) and n-(p-methoxybenzylidene)-p-butylaniline (MBBA), respectively.

Thermotropic systems composed of small rod-like organic molecules generally form two different families of organizations, known as nematic and smectic phases. The nematic phase is the simplest liquid crystal phase. In this phase the molecules maintain a preferred orientational direction but have no positional order. The other

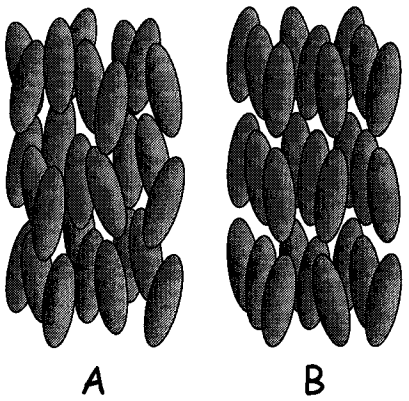

Figure 1–3: Organizations of rod-like molecules in nematic (A) and smectic-A (B) mesophases.

organization common to systems of rod-like molecules is the smectic phase. In this phase, there is one dimensional positional order in addition to orientational order. Molecules are grouped on a series of equidistant parallel layers where they are free to move. Smectic liquid crystals with their layered structure are the most ordered and viscous mesophases. Twelve different types of smectic mesophases have been identified to this day. They usually bear the labels A, B, C, ..., L according to their chronological order of discovery [2, 31, 32]. Figure 1–3 provides a schematic representation of nematic and smectic-A organizations of rod-like structural units.

Generally, if the molecules that form a liquid crystal phase are chiral (i.e., lack inversion symmetry or mirror image) then macroscopic chiral phases exist. They are chiral versions of nematic and smectic phases. The essential organizational difference between ordinary (non-chiral) and chiral phases, is that in chiral phases,

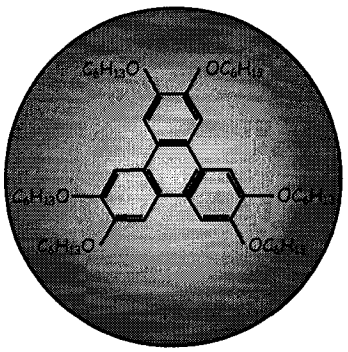

Figure 1–4: The discotic molecule C6OTP.

the molecules' preferred direction rotates throughout the sample. The distance required for a full rotation is the pitch of the phase. Chiral nematic mesophases are often called cholesterics since these organizations were first observed in cholesterol derivatives, however the historical term is misleading since many other materials can exhibit chiral or twisted nematic phases [2, 31, 32].

Disc-like molecules (i.e., molecules with one molecular axis much shorter than the other two) also form liquid crystal phases. Such compounds are called discotic liquid crystals, and again rigidity in the central part of the molecules is essential [2–4, 32]. Figure 1–4 provides the chemical structure of a typical discotic mesogens by the name of 2, 3, 6, 7, 10, 11-hexakishexyloxytriphenylene (C6OTP).

Thermotropic systems constituted of small disc-like organic mesogens also form nematic and smectic arrangements. In nematic discotic phases, the molecules move about quite randomly, but on an average, the axis perpendicular to the plane of each molecule tends to orient along a preferred common direction. In smectic discotic phases, often called columnar phases, the molecules exhibit some degree of positional

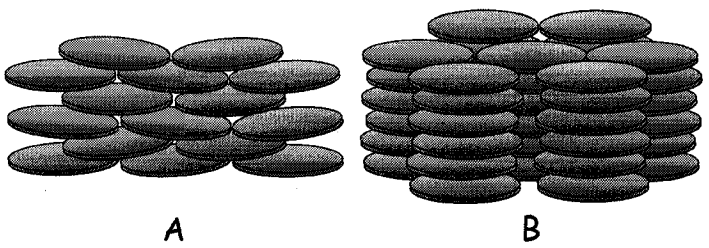

Figure 1–5: Molecular arrangements in the nematic discotic and columnar mesophases.

order as most of the molecules tend to position themselves in columns. In addition, those columns tend to arrange into hexagonal lattices [2–4,32]. Figure 1–5 illustrates the arrangement of the molecules in the nematic discotic and columnar phases. Chiral nematic discotic phases may also be found in nature. Finally, it is worth noticing that while some compounds exhibit only one liquid crystal mesophase (e.g., PAA) others display several (e.g., cholesteryl myristate).

Liquid crystals made from polymers. Polymers are macromolecules that form when chemical reactions link shorter molecules together. Essentially two main types of polymers may give rise to liquid crystal phases. The first type is main chain polymers which are composed of fairly rigid monomers resembling the previously discussed rod and disc-like mesogens and connected end to end by flexible segments. Although these long polymers may move around and collide with each other in the liquid crystal phases, the rigid rod and disc-like units tend to remain pointing in one common direction. The second type of polymers forming liquid crystal phases are side chain polymers which are composed of one single completely flexible polymer with rigid mesogenic units attached as side chains along its length by other short flexible

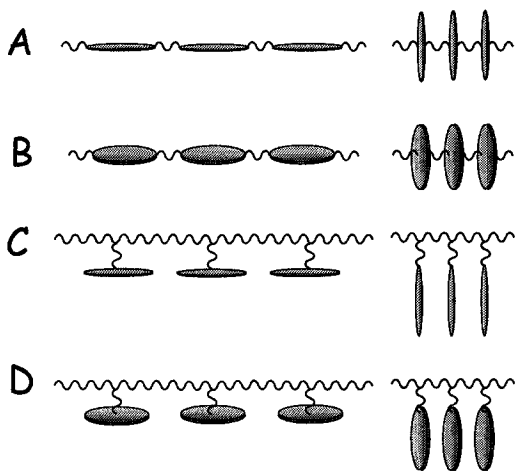

Figure 1–6: Different types of polymers forming liquid crystals. (A) Main-chain polymer made of rod-like units; (B) Main-chain polymer made of disc-like units; (C) Side-chain polymer made of rod-like units; (D) Side-chain polymer made of disc-like units.

segments. In liquid crystal phases, the long flexible parts of these polymers wind by however, the rigid mesogenic units attached to them tend to show orientational order [2, 11, 12]. Figure 1–6 illustrates types of polymers capable of forming liquid crystal mesophases.

As in the case of liquid crystal phases formed from small organic molecules, polymer-based liquid crystal phases can be either thermotropic or lyotropic. Thermotropic liquid crystals are often referred as polymer melts whereas lyotropic polymer liquid crystals are denoted as polymer solutions [11, 12, 33]. In addition to these similarities with small mesogens systems, polymer liquid crystals also form similar arrangements namely: nematic and smectic phases (possibly chiral).

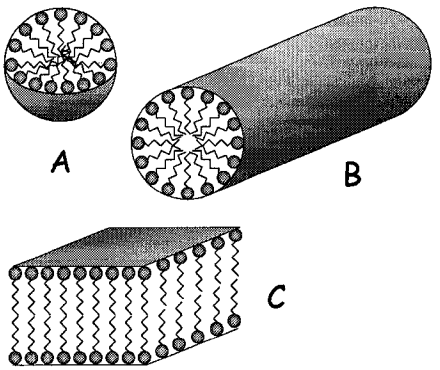

Figure 1–7: (A) Spherical, (B) rod-like and (C) plane-like amphiphilic units.

Liquid crystals made from amphiphiles. Amphiphiles are molecules that combine a hydrophobic (water-fearing) group at one end and a hydrophilic (water-loving) group at the other end. Amphiphilic or amphipathic molecules also known as surfactants (i.e., surface active agents) may form ordered structures in both polar and non-polar solvents. These types of liquid crystals belong to the class of lyotropics. Soaps and phospholipids are two important examples of amphiphiles leading to liquid crystal phases [2–4]. Amphiphilic molecules form liquid crystal phases that are slightly different from the liquid crystals formed by small organic molecules and polymers. When dissolved, at low concentration, in a polar solvent such as water, the hydrophobic 'tails' assemble together and present the hydrophilic 'heads' to the solvent. The resulting structure for soap molecules is called a micelle and for phospholipids it is called a vesicle (inverted-micelle). There is orientational and sometimes positional order of the molecules within these structures, but there is no ordering of the micelles or the vesicles themselves. At higher concentrations, the spherical micelles and vesicles may transform into rod-like or even disc-like amphiphilic units

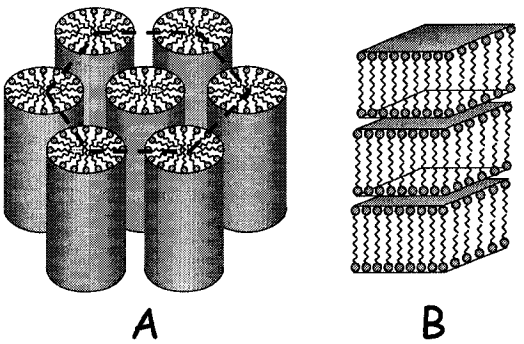

Figure 1–8: Hexagonal (A) and lamellar (B) phases of rod-like and plane-like amphiphilic units, respectively.

or else in flat bilayers [2–4]. Figure 1–7 gives the representations of some possible amphiphilic arrangements. At very high concentration (~50%), these various amphiphilic units combine to form larger liquid crystal phases. One example is the hexagonal phase, which possesses a hexagonal arrangement of long cylindrical rods of amphiphilic molecules. Other examples include the lamellar and cubic phases of bilayers and spherical units, respectively [2–4]. Figure 1–8 provides schematics of the hexagonal and lamellar phases.

1.2.4 Where are liquid crystals involved?

Even though liquid crystals are fluids, the existence of orientational order ensures that all directions in the material are not equivalent. This anisotropy has a profound effect on the mechanical, electrical, magnetic and optical properties of the various phases making them useful structural and functional materials. Indeed liquid

crystalline phases play a significant role in our everyday life; not only they are becoming an increasing part of our high-tech environment but also they are indispensable to any biological systems.

Displays. Undoubtedly, liquid crystals are best known for their successful electro-optical applications which started in the mid-1960s and which now represent a multi-billion US-$ global market. Though initially appeared in wrist-watches, calculators and clocks, liquid crystals are now being used for all kinds of advanced domestic applications, like cell phones, cameras, automobile dashboards, switchable window panels, laptops and other flat panel displays [2]. Their advantage was first their low power consumption and small size; now they are competitive with other technologies for attractiveness, ease of viewing, cost and durability.

Electro-optical applications may use nematic or smectic liquid crystal phases as well as their twisted counterparts. These applications are based on the fact that the liquid crystal mesogens can be oriented by low external electric fields (a phenomenon known as Freedericksz transition) and therefore can disrupt the anisotropic optical property of the mesophases [2].

Sensors. Liquid crystals are also used in various sensors, mostly temperature sensors [2]. Applications include: fever thermometers, hot warning indicators, monitoring devices for packaging of child food, portable battery tester, mood rings, color changing jewelry, decorative wall coverings, etc. Temperature sensitive films have also been developed to detect local heating due to the presence of radiation or certain vapors, or due to the poor electrical connections on circuit boards. Medical thermography remains the most important liquid crystal sensor application as it

provides an aid in the diagnosis of circulatory problems and cancerous growths while being able to map the local temperature variations of the skin. These thermo-optical devices are usually based on chiral nematic liquid crystals and their associated capability to reflect different colors as the length of their pitch varies with temperature. The pitch can also vary with concentration and pressure that provides the basis for other sensors.

Fibers. One of the best examples of fiber formed from a liquid crystal phase is the ultra-high strength polyamide Kevlar [2,11,12]. Although slightly denser than nylon, Kevlar is roughly thirty times stronger. In fact pound per pound, Kevlar is stronger than steel (steel is five times denser). A few of Kevlar's applications include ropes and cables; tires; protective and performance apparels; friction products and gaskets; composites; adhesives and sealants.

Kevlar is formed from a lyotropic liquid crystal phase that is produced by dissolving a polyamide in sulphuric acid. The solution is then extruded in such a way that the polymer chains acquire significant orientational order. Finally, the fluid is solidified by removing the solvent. The orientational order of the main chain is 'frozen in' during this last step providing the fiber its ultra-high strength.

Surfactants. Surfactants are wetting agents that lower the surface tension of a liquid, allowing easier spreading, and lower the interfacial tension between two liquids. Surfactants play an important role in many practical applications and products, including detergents and emulsifiers. The detergent industry produces soaps, powders, creams, and foaming agent of all kinds. On the other hand, in the food industry, emulsifiers serve to maintain texture, color, flavor or viscosity. Emulsifiers

are used in mayonnaise, salad dressings, marshmallow, whipped cream, beer, cheese, ice cream, and jelly. Another use of surfactants is in the oil recovery industry. Surfactants are used to trap the oil located in porous rocks prior pumping. There are also medical applications like surfactant-assisted drug release strategies. In all those applications the surfactants form a lyotropic liquid crystal phase at sufficiently high concentrations [2–4].

Biology. Living organisms are composed of cells which constitute the various organs and perform varied functions of life. Clearly, for these functions to occur the cells must have a form and a structure and there must be mechanisms by which materials enter and leave the cells. The medium which provides the cell a structure and allows the selective transportation of materials between cells is the plasma membrane. The cells utilize the properties of the plasma membrane to organize the environment and appropriate interactions between the cells. Plasma membranes are made of phospholipids that have a structure resembling soaps and detergent surfactants where the molecules are amphiphilic. Biological membranes are lyotropic liquid crystals generated by the dissolution of phospholipids in water [2–4]. Many biological polymers also form lyotropic phase, including cellulose, polypeptides, DNA, and linear viruses like tobacco mosaic virus.

1.3 Background on the modelling and simulations of nematic defects and textures

The importance of nematic liquid crystals in the realm of science and engineering has grown remarkably fast in view of the fact that even their existence as a phase of matter was not recognized until the end of the 19^{th} century. Due to their unique

combination of fluidity and partial orientational ordering, nematic liquid crystals are used in a number of technological applications and are omnipresent in nature.

As any ordered media nematic liquid crystals often contain sharp, localized distortions called defects that are of various dimensionality [2–4, 11, 31, 32]. The distribution of these defects, called texture, usually has a profound impact on the structure and therefore on the physical properties of a given system. In some cases they can be rather detrimental while in other cases they are desirable. Due to the liquid character of the medium, nematic defects can move under the effect of elastic forces until they reach some equilibrium position that minimizes their associated distortion free energy.

In order to eventually remove or more generally control these defects and hence optimize the performances of a nematic-based system, it is imperative to thoroughly understand their static and dynamic properties. In this thesis modelling and simulations of nematic defects and textures is performed to achieve that goal and therefore, this section gives an overview of the invoked theoretical background.

1.3.1 Basic description of orientational order in terms of the director field n(r)

Order in nematic liquid crystals is purely orientational. Considering a microscopic region of a nematic sample containing a sufficiently large number of molecules, orientational order is materialized by the tendency that mesogens have to roughly orient their long axis in parallel along a common direction while keeping their centers of mass randomly distributed as in ordinary liquids [31, 32]. This average preferred orientation, along which the molecules point, is commonly referred as the director

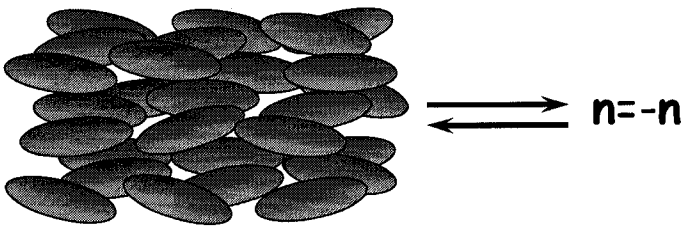

Figure 1–9: The basic *order parameter* of nematics: the director **n**. The director is a headless unit vector giving the average preferred orientation of the molecules in microscopic region of the sample.

of the mesophase and is often denoted by the unit vector **n**. The director **n** is the basic *order parameter* used to model orientational order in a nematic phase. A quintessential property of ordinary, non-ferroelectric, nematic mesophases is that their constituent molecules are non-polar and therefore there is no physical difference between the states $-\mathbf{n}$ and **n**. As it will be soon apparent this equivalence has profound impact on the symmetry of the defects and their associated textures. Figure 1–9 illustrates the concept of director in a microscopic region of a nematic sample constituted of rod-like molecules.

Defining a director at every spatial position **r** of the nematic system (i.e. defining the director field $\mathbf{n}(\mathbf{r})$), leads to a macroscopic description of orientational order [31, 32]. In absence of any perturbing external forces (electric, magnetic or flow fields), the orientational order in a nematic sample is completely determined by the shape of its container and its anchoring (i.e. surface-imposed molecular orientation) [3, 4]. When, for example, a nematic sample is sandwiched between two parallel flat plates with identical anchoring conditions and forms a thin film, the orientation of

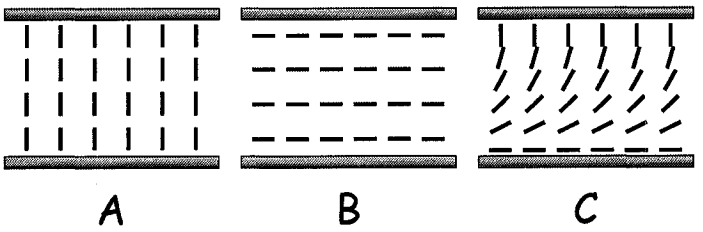

Figure 1–10: Homeotropic (A), planar (B) and bended (C) configurations. The short black segments represent headless local directors. (A) and (B) are homogeneous director fields while (C) is heterogeneous.

the molecules at equilibrium is homogeneous and solely determined by the surface-imposed molecular orientation. This phenomenon is due to the fact that the nematic orientational order is *long-range*.

However, if the same nematic sample is now sandwiched between two parallel flat plates imposing mutually different molecular orientations, the bulk orientational order cannot be any longer homogeneous. In such a case, the molecules must progressively vary their orientation throughout the sample in order to satisfy the different orientational constraints imposed by the top and bottom surfaces. Accordingly, all the local directors undergo smooth progressive orientational variations in space. Figure 1–10 exemplifies the different situations described above by means of director fields.

1.3.2 Nature of defects and textures in nematics

The generic term *defect* usually designates a local imperfection that breaks the order of the molecular arrangement in an ordered medium. In nematic liquid crystals, defects break the rotation symmetries and can be simply seen as local, small-scale,

sharp distortions of the orientational order [34, 35]. Much like as in the case of global, large-scale, gentle deformations considered in the previous section, defects often originate from an incompatibility between geometric and anchoring constraints as well as from the possible presence of orientationally disturbing external forces. Defects often also show up during phase transition-related phenomena such as the nucleation and growth of isolated nematic domains in an isotropic phase or in the front propagation of a nematic phase in an isotropic phase.

Nematic liquid crystals exhibit an extremely rich variety of defects which can occur in the bulk as well as at the surface of the material (only bulk defects are discussed in this thesis). These defects are generally classified according to their dimensionality and to the nature of their core. Nematic defects can be zero-dimensional, one-dimensional or two-dimensional and consequently be in the form of points, lines or walls, respectively. Then depending on whether or not a director field $\mathbf{n}(\mathbf{r})$ can be defined in their core, they are termed singular or non-singular [31, 32, 34–37].

Line defects. The most common type of defect found in nematics is the line defect and nearly all of them are singular. Singular line defects are often referred as *disclinations* [31, 32, 34–36]. Various types of disclinations are found in nematic samples. Of particular interest in this thesis are the so-called *wedge disclinations.*

Wedge disclinations are planar director field configurations which, away from their singular core, can be described by the director field $\mathbf{n} = (\cos\phi, \sin\phi, 0)$ with $\phi = M\theta + \phi_0$ and $\theta = \arctan(\frac{y}{x})$. In these expressions ϕ is a function giving the angle made by the director field with respect to the x-axis while M and ϕ_0 are constants

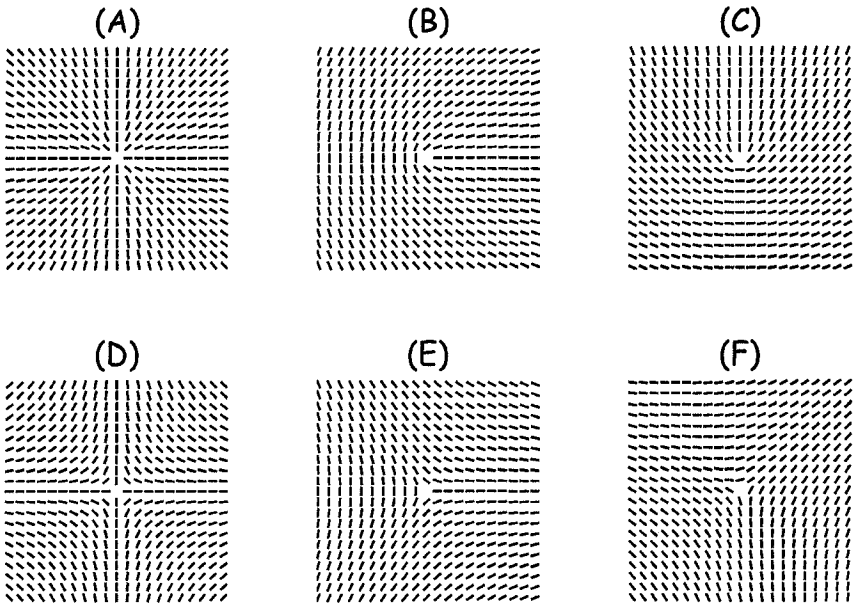

Figure 1–11: Director configurations around various wedge disclinations (singular line defects). (A) $M = +1$, (B) $M = +1/2$, (C) $M = +1/2$ & $\phi_0 = \pi/4$, (D) $M = -1$, (E) $M = -1/2$ and (F) $M = -1/2$ & $\phi_0 = \pi/3$. Note that no director can be defined in the core of the various disclinations.

corresponding to the *strength* of the disclination and the angle made by the tangent of the director when $\phi = 0$, respectively [31, 32, 35, 37].

The magnitude of the strength M corresponds to the number of π rotation made by the director when encircling the core of the disclination anticlockwise. The values taken by the strength $|M|$ are multiples of $\frac{1}{2}$. The sign of the strength M is positive or negative according to anticlockwise or clockwise rotation of the director when encircling the defect core [31, 32, 35]. Figure 1–11 gives schematic representations of the most common wedge disclinations found in nematics in terms of their director fields.

The study of defects has played an important role in understanding the structure and physical properties of liquid crystals. In fact the observation and identification of defects in a polarizing microscope enabled Friedel to elucidate the different structures of liquid crystals and to classify them [3, 4, 31, 38].

The generic term *texture* was initially coined to denote a particular *signature* left by an arrangement of defects in a nematic sample observed under polarized light [31, 32, 34–36]. Today, the term texture is however also often employed in a broader sense to designate the particular director field adopted by a liquid crystal in a given geometry, which can be ironically defect-free sometimes [11].

The two textures that have permitted the identification of the nematic mesophase are the *Threaded* and *Schlieren* textures [3, 4, 31, 38]. In the Threaded texture that can be observed in thick nematic samples, the wedge disclinations are roughly parallel to the surfaces and appear as freely floating flexible filaments. The visibility of the filaments or threads in polarized and unpolarized transmitted light microscopy is due to their high phase contrast with respect of the rest of the bulk material (i.e. the threads scatter light strongly). The Threaded texture is the one that gave the nematic phase its name, from $\nu\eta\mu\alpha$ (nema), the Greek word for *thread.* The Schlieren texture also known as *Nuclei texture* is usually observed in rather thin nematic samples using polarized light microscopy. In this texture, the signature of the wedge disclinations, which are roughly perpendicular to the sample surfaces, consists of dark brushes connected to points called nuclei. The black stripes (extinctions of light) correspond to the regions where the nematic directors are either parallel or perpendicular to the plane of the analyzer or polarizer. Moreover, the number of black

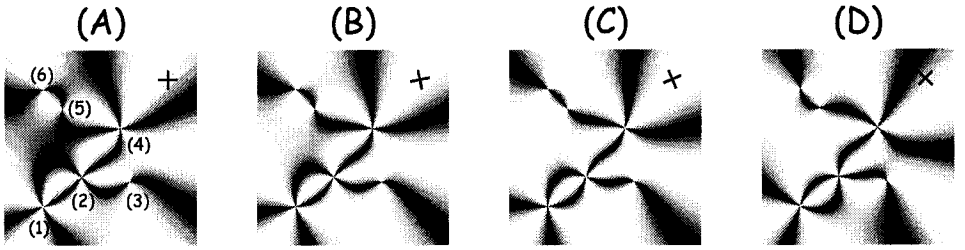

Figure 1–12: Computed Schlieren texture for different orientations of the ensemble polarizer-analyzer (indicated by the cross). The following disclination strengths can be identified: (1) $M = -1$, (2) $M = +1$, (3) $M = -1/2$, (4) $M = -1$, (5) $M = +1/2$ and (6) $M = -1/2$. All the disclinations are running out-of-the visualization plane going through the nuclei.

brushes emanating from the nuclei and their sense of rotation as the polarizer and analyzer are rotated at unison gives the strength of the line defect [39]. The magnitude of the disclination strength is given by the relation: $|M| = \frac{\text{Number of brushes}}{4}$. The sign of the strength is then determined to be positive or negative according to the rotation of the brushes with or against the direction of the ensemble polarizer-analyzer, respectively. The nuclei or meeting points of the brushes remain unaffected by the rotation of the polarizer-analyzer ensemble [3, 4, 31, 32, 36, 39]. Figure 1–12 shows a Schlieren texture computed from a given director field for different orientations of the ensemble polarizer-analyzer.

The sum over all disclination strengths (including their sign) of a very large sample usually tends to vanish. Typically, two connected disclinations have opposite signs. Note that due to the mobile character of their medium, disclinations may move within the sample and therefore their overall distribution is generally not a

static feature. Disclinations of opposite signs attract each other while those of equal signs repel [3,4].

If two disclinations of opposite signs but same strength eventually merge they annihilate to yield a uniform defect-free sample area. However, if two disclinations have opposite signs but different strengths they form a new defect whose strength is equal to the sum of the strengths of the two original defects (i.e. the sum of the strength is always conserved). Furthermore, a disclination of strength $|M| > 1/2$ can, under certain conditions, dissociate into two disclinations [3,4,39].

Now more specifically, depending on its energetic cost to the system, a $|M| = 1$ singular line defect can: a) remain as disclination, b) dissociate into two $|M| = 1/2$ singular line defects or c) can transform into a non-singular $|M| = 1$ line defect. The latter process is known as *escape into the third dimension* and is of particular interest in this thesis. It consists in the progressive bending of the director field out-of-the plane perpendicular to the original disclination line [40–42]. The resulting director configuration or texture is easily recognized in nematic-filled cylindrical capillaries with cavity walls imposing a radial anchoring. In such a case the director field can be parametrized in cylindrical coordinates as: $\mathbf{n} = (\cos\Phi, 0, \sin\Phi)$ with $\Phi = \pm 2 \arctan\left(\frac{R}{r}\right) \mp \frac{\pi}{2}$ and R standing for the radius of the cavity. Figure 1–13 provides the director fields corresponding to the singular and non-singular $|M| = 1$ line defects that can be found in a cylindrical cavity.

Point defects. In addition to line defects, nematic liquid crystals can also exhibit point defects. These defects often referred as *hedgehogs* but also sometimes as *monopoles* or *umbilics* are always singular [3,4]. There are two types of point defects

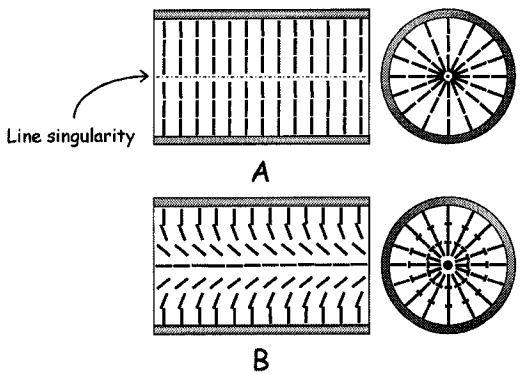

Figure 1–13: Director fields corresponding to the *planar radial with line defect* (PRLD) and *escape radial* (ER) textures. The PRLD texture (A) contains a singular line defect running along the cavity axis while the ER texture (B) is continuous. In both cases the strength of the line defect is however $M = +1$. The *head-nail* convention, where the head of the nail is farthest from the reader, is used to show the tilting of the directors.

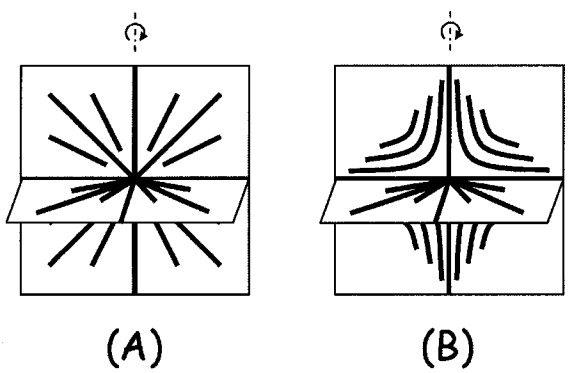

Figure 1–14: Schematics of the $M = +1$ radial (A) and $M = -1$ hyperbolic (B) hedgehogs using flux lines. The flux lines are everywhere tangent to the director field. Note that the origin points are singular.

that are of interest in this thesis: the *radial hedgehog* and the *hyperbolic hedgehog.* The director fields corresponding to the radial and hyperbolic hedgehogs can be defined, away from their singular cores, by the expressions: $\mathbf{n} = (x, y, z)/\sqrt{x^2 + y^2 + z^2}$ and $\mathbf{n} = (-x, -y, z)/\sqrt{x^2 + y^2 + z^2}$, respectively. Figure 1–14 shows schematic of the two type of hedgehogs using the *flux lines.* The flux lines are everywhere tangent to the director field [43]. The radial point defect has a pure radial structure and any cross section containing the central singularity exhibits the director pattern of the $M = +1$ wedge disclination line previously described. On the other hand, the hyperbolic point defect has a mixed nature since its director field in the plane $z = 0$ also corresponds to the $M = +1$ wedge disclination configuration, its $x = 0$ and $y = 0$ planes correspond to the $M = -1$ wedge disclination pattern. Like the wedge disclinations, the point defects carry a strength M. The radial and hyperbolic hedgehogs respectively carry the strength $M = +1$ and $M = -1$ [3, 4].

An intuitive way to create a radial hedgehog is to place a nematic sample in a sphere whose surface is enforcing a radial anchoring. This occurs naturally when a nematic forms small droplets in a non-miscible fluid, for example. Another possible occurrence of point defects is when two non-singular defect lines meet in a cylindrical capillary and they have opposite escape directions. In such a situation, both the radial and hyperbolic hedgehogs are formed. The texture formed by an alternative distribution of point defects in a cylindrical cavity is called *escape radial with point defects* (ERPD). This texture presented in figure 1–15 is of fundamental importance to this thesis (see Chapter 4 to 7) as it has been observed along the spinning extrusion duct of spiders [18, 25, 27, 44].

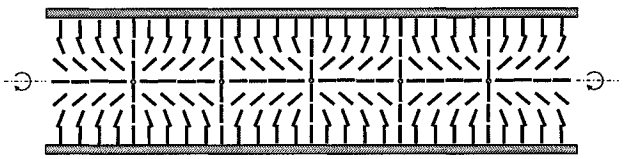

Figure 1–15: The escape radial with point defects (ERPD) texture occurring in nematic-filled cylindrical cavities with sidewalls enforcing homeotropic anchoring. A singular point defect is formed at every junction of two oppositely oriented escaped domains.

When two point defects of $|M| = 1$ strengths but opposite signs merge together, they annihilate and give a non-singular $M = +1$ line defect or escape line defect. Another interesting feature of point defects that is of particular interest to this thesis is their connection to $|M| = 1/2$ wedge disclinations. Indeed, $|M| = 1/2$ wedge disclination loops or rings can emerge out of $|M| = 1$ point defects [45–48]. In such a process the total strength or charge of the defect is conserved. This intimate relationship between point and loop singularities raises the question: Do point defects exist or are they loops which are simply too small to be discerned as such? This puzzling question is studied in this thesis and answers are presented in chapters 6 and 7. Figure 1–16 pictures the broadening of singular point defects into disclination loops of half-integer strength.

Wall defects. The last class of defects encountered in nematics and encountered in this thesis is the wall defects (Chapters 2 & 3). In the field of nematic defects, the term *wall* is often used to describe a steep but continuous re-orientation of the director field by an angle of π radians involving a plane and hence wall defects are often referred as *inversion walls* [4, 6, 8, 34, 49]. Inversion walls alone are non-singular defects but their structures may involve singular wedge disclinations

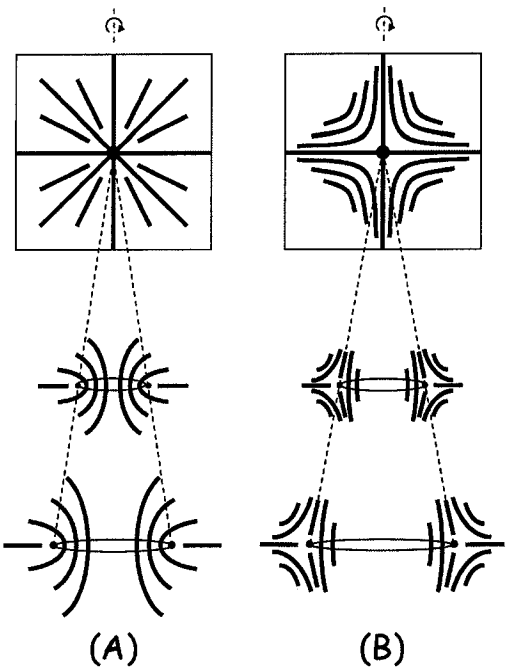

Figure 1–16: Broadening of singular point defects into disclination rings or loops of strength $M = \pm 1/2$. (A) the $M = +1$ radial hedgehog splits into a $M = +1/2$ disclination loop and (B) the $M = -1$ hyperbolic hedgehog splits into a $M = -1/2$ disclination loop.

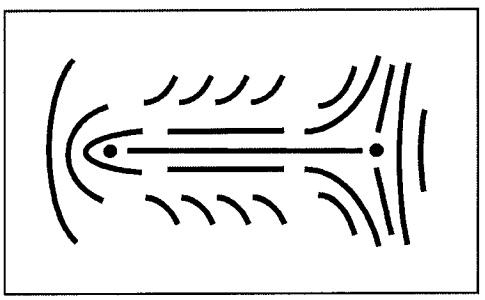

Figure 1–17: Schematic of a typical inversion wall defect between two $|M| = 1/2$ disclinations (running out of the drawing plane). The plane of wall is perpendicular to the drawing plane. On crossing the wall the director continuously rotates by π radians.

of various strengths. Despite that wall defects can occur strictly in the bulk of a nematic sample, they often occupy the entire cross section reaching the top and bottom surfaces (This is the case of wall defects studied in this thesis). Given the close relationship to surfaces and disclinations, a particular wall defect is often given several different names throughout the literature [4, 6, 36, 49, 50]. An example of an inversion wall defect is given in figure 1–17.

1.3.3 Free energy minimization

In a homogeneous nematic mesophase, all the local directors are aligned in parallel. This equilibrium configuration of the system corresponds to a state of minimum free energy. However, in most circumstances, the shape of the container, the anchoring as well as the possible presence of external disturbing forces are such that the orientational order of the nematic phase is distorted and the orientation of the local directors are no longer spatially invariant. In order to determine the

orientation taken by the local directors in such case, one needs to minimize the free energy of the system [3, 4, 43, 51].

The total free energy F of a bounded nematic system is given by the sum of bulk and surface terms: $F = \int_V f_b dV + \int_S f_s dS$. In its simplest form, the functional f_b relating the bulk elastic free energy of the system to the nematic director field gradients reads: $f_b = \frac{K}{2}(\nabla \mathbf{n}) : (\nabla \mathbf{n})^T$, where K is a positive material dependent elastic constant. This last expression is known as the Frank-Oseen elastic free energy [3, 4, 43, 51]. The standard expression used for surface free energy density, f_s, is due to Rapini and Papoular and reads: $f_s = \frac{W}{2}\left[1 - (\mathbf{n} \cdot \mathbf{e})^2\right]$, where W is the surface anchoring strength and $\mathbf{e}$ is a unit vector representing the easy axis or preferred orientation of the nematic director at the surface [3, 4, 52].

The basic system of equations leading to the equilibrium configuration of the director field is obtained from variational calculus (i.e. Euler-Lagrange equation) and reads:

$$\textbf{(Model I)} \begin{cases} \frac{\partial f_b}{\partial \mathbf{n}} - \nabla \cdot \frac{\partial f_b}{\partial \nabla \mathbf{n}} = -K\nabla^2 \mathbf{n} = \lambda_b \mathbf{n} & \text{On } \Omega \\ \frac{\partial f_s}{\partial \mathbf{n}} + \mathbf{N} \cdot \frac{\partial f_b}{\partial \nabla \mathbf{n}} = -W(\mathbf{n} \cdot \mathbf{e})\,\mathbf{e} + \mathbf{N} \cdot K\nabla \mathbf{n} = \lambda_s \mathbf{n} & \text{On } \partial\Omega \end{cases} \tag{1.1}$$

In this system of equations, λ_b and λ_s are Lagrange multipliers introduced to fulfill the unit length constraint of the nematic director $\mathbf{n}$ in the bulk and at the surface; $\mathbf{N}$ is a unit vector representing the surface normal while Ω and $\partial\Omega$ respectively represent the computational domain and its boundary. Model I, given by system 1.1, is used in chapter 2 and 3 to simulate and analyze the continuous structure of inversion wall defects occurring in a nematic thin film.

As explained in the previous section, no director field can be defined in the core of a singular nematic defect. If in such case it is still possible to do various analytical calculations excluding the core region of the defect, it is however not practically possible to perform any serious computer simulations. The reason for this is that trying to assign a director in the singular region leads to infinite director gradients and therefore an infinite elastic energy. One simple way to remedy this problem is to allow the director field to relax from its unit length constraint in the singular region [53,54]. Assuming that anchoring strength is infinite and that therefore surface molecular orientation is fixed, the dynamic evolution of the director field toward its equilibrium configuration can be written using this approach as:

$$\textbf{(Model II)} \begin{cases} \gamma \frac{\partial \mathbf{n}}{\partial t} = \nabla \cdot \frac{\partial f_b}{\partial \nabla \mathbf{n}} - \frac{\partial f_b}{\partial \mathbf{n}} = K \left[\nabla^2 \mathbf{n} - \frac{(\mathbf{n}^2 - 1)\mathbf{n}}{\delta^2} \right] & \text{On } \Omega \\ \mathbf{n} = \mathbf{n_0} & \text{On } \partial\Omega \end{cases} \tag{1.2}$$

In this equation, γ is a constant related to the rotational viscosity of the director and δ is a penalty parameter related to the size of the defect core. This approach is used in chapter 5 to simulate the collective interaction between point defects along a nematic cylindrical capillary.

1.3.4 Continuous description of orientational order in terms of the tensor order parameter field Q(r)

So far the *order parameter* use to describe the *orientational order* in the nematic phase has been a unit vector called director and denoted by **n**. Using this approach however may present two serious problems depending on the nature of defects involved in the texture. The first potential flaw is, as mentioned in the previous

section, that the director field cannot be defined when modelling a texture containing singular defects. The second problem with this vectorial approach is that $M = \pm 1/2$ line defects cannot be described as the $\mathbf{n}(\mathbf{r}) = -\mathbf{n}(\mathbf{r})$ restriction on the director field is not retained after discretization of the Laplacian operator appearing in the governing equations. [Model I (cf. system 1.1) and II (cf. system 1.2).] A simplistic approach to palliate the former problem consists of abandoning the Lagrange multipliers and add a penalty term instead so that the unit norm of the director field is only satisfied away from singular regions. This technique is particularly useful when dealing with singular defect where a detailed analysis of the defect core structure and energy is not necessary. The technique is however not applicable when dealing with $M = \pm 1/2$ line defects.

A more physically sound approach to treat nematic defects and textures is to use the *tensor order parameter* $\mathbf{Q}(\mathbf{r})$ [3,4,31,33,55,56]. Using the $\mathbf{Q}(\mathbf{r})$-tensor as the order parameter presents several advantages: the first being that it is continuous in any type of defect; the second is that it automatically retains the head-tail invariance of the director ($\mathbf{n}(\mathbf{r}) = -\mathbf{n}(\mathbf{r})$); finally in contrast to the director $\mathbf{n}(\mathbf{r})$ that can only describe uniaxial ordering, the tensor order parameter $\mathbf{Q}(\mathbf{r})$ can also describe isotropic as well as biaxial symmetries. The fact that $\mathbf{Q}$ can describe isotropic states is particularly useful when one is, for example, interested in investigating ordering evolution during phase transitions. On the other hand biaxial states are common in the vicinity of defect cores as they help lower the free energy of the system. The tensor order parameter $\mathbf{Q}(\mathbf{r})$ is a real symmetric and traceless tensor and has therefore, in the most general situation, five independent degrees of freedoms (in contrast, the

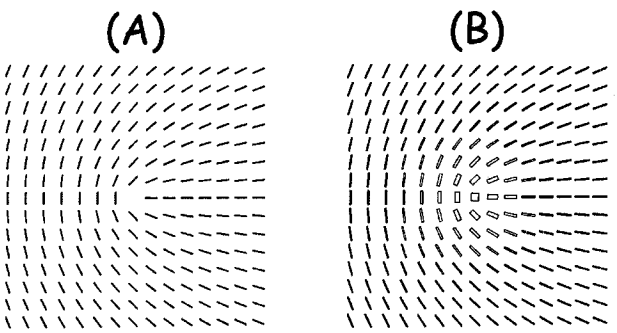

Figure 1–18: Non-continuous (A) vs. continuous (B) description of orientational order around a $M = +1/2$ wedge disclination. Orientation and amplitude of boxes are given by the eigenvectors and corresponding eigenvalues, respectively. The inner core of the defect as well as its periphery are uniaxial (boxes with one distinct edge) while the circular transition region is biaxial (boxes with two distinctive edges).

director $\mathbf{n}(\mathbf{r})$ has only two). It can be represented, in terms of its eigensystem as follows: $Q_{ij} = \mu_n n_i n_j + \mu_m m_i m_j + \mu_l l_i l_j$. In this expression, $\mathbf{n}$, $\mathbf{m}$ and $\mathbf{l}$ are unit eigenvectors forming an orthogonal triad and μ_n, μ_m and μ_l are their corresponding eigenvalues. The eigenvalues μ_i $(i = 1, 2, 3)$ of the tensor order parameter are restricted by: $-1/3 \leq \mu_i \leq 2/3$ and $\mu_n + \mu_m + \mu_l = 0$. The director triad and the eigenvalues characterize the orientation and the strength of alignment of the phase respectively. The largest eigenvalue in magnitude or absolute value, μ_n, gives the strength of ordering along the uniaxial director $\mathbf{n}$. The second μ_m and third μ_l eigenvalues correspond respectively to the biaxial directors $\mathbf{m}$ and $\mathbf{l}$ $(\mathbf{l} = \mathbf{n} \times \mathbf{m})$. Figure 1–18 compares representations of orientational order around a typical disclination line using the vectorial $(\mathbf{n}(\mathbf{r}))$ and tensorial $(\mathbf{Q}(\mathbf{r}))$ approaches.

In the case of strong anchoring conditions, surface orientation is fixed as any deviations can cause a disproportionate energy penalty to the system. Therefore surface

free energy does not need to be taken into account in the free energy minimization process. The bulk free energy density of a nematic system expressed in terms of the tensor order parameter, which is commonly referred as the Landau-de Gennes free energy, is given by the sum of a homogeneous f_h and a gradient f_g contribution (i.e. $f_b = f_h + f_g$) [3, 4, 31, 56]. The homogeneous free energy density describes short-range ordering effects and it penalizes any deviations from the equilibrium uniaxial ordering and reads: $f_h = \frac{A}{2}Q_{ij}Q_{ji} - \frac{B}{3}Q_{ij}Q_{jk}Q_{ki} + \frac{C}{4}(Q_{ij}Q_{ji})^2$, where A is a function of the thermodynamic driving force (i.e temperature or concentration), and B and C are positive thermodynamic constants describing the equilibrium nematic order. The gradient free energy density is an analogue to the Frank-Oseen bulk free energy which penalizes the long-range variations of the tensor order parameter $\mathbf{Q}$. In its simplest form it is given by: $f_g = \frac{L}{2}\nabla_k Q_{ij}\nabla_k Q_{ij}$, where L is an elastic constant.

The dynamic equation describing the relaxation of the tensor order parameter $\mathbf{Q}(\mathbf{r}, t)$ towards an equilibrium value that minimizes the total free energy under the different constraints (shape and size of the container, anchoring at its surface, etc.) is then given by [3, 4, 31, 56]:

$$\textbf{(Model III)} \begin{cases} \eta\frac{\partial Q_{ij}}{\partial t} = -(AQ_{ij} - BQ_{ik}Q_{kj} + CQ_{lm}Q_{ml}Q_{ij}) + L\nabla^2 Q_{ij} & \text{On } \Omega \\ Q_{ij} = Q^0_{ij} & \text{On } \partial\Omega \end{cases} \tag{1.3}$$

In the above equation, η is a constant related to rotational viscosity. Model III is employed in chapters 4, 6 and 7 to analyze textures composed of singular line and point defects.

1.4 Motivation and objectives

Two different problems involving defects and textures in liquid crystal-based applications are examined in this thesis. Both the problems involve nematic phases of rod-like mesogens in confined geometries. The first problem deals with a polymer-dispersed liquid crystal (PDLC) film that forms the basis for electro-optical applications such as displays or smart windows (light shutters).

PDLC systems are liquid crystal-polymer composites where in general 50-80 wt% of low molecular weight liquid crystalline material is dispersed in a continuous polymer matrix. The liquid crystalline domains normally have a droplet-like morphology but larger cellular (polygonal shape) morphology may also be found instead. PDLC applications are based on the ability that the mesogens of a nematic phase have to align under an electric field. In a typical application, a thin PDLC film (few microns thick) is deposited between clear plastic covers coated with a very thin layer of conducting material.

Transmission of light through a PDLC thin film depends primarily on scattering which in turn depends upon the difference in refractive index between the liquid crystal dispersed phase and their environment. In the 'field-on' state the dispersed liquid crystal phase is forced to orient uniformly and therefore there is very little difference in the refractive indexes and consequently the material appears transparent. However, in the 'field-off' state, the dispersed liquid crystalline material is not constrained to orient in a particular direction and therefore there is a considerable

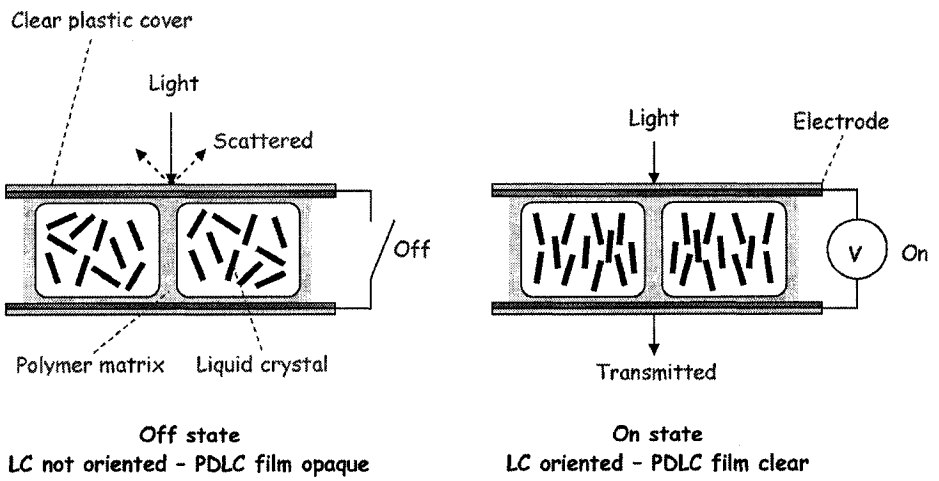

Figure 1–19: Cartoon giving the basic functioning of a PDLC film design for electro-optical applications.

difference in the refractive indices and hence strong scattering. The film in the field-off state therefore looks milky. Figure 1–19 illustrates the basic functioning of a PDLC-based electro-optical device.

Anchoring or the surface preferential orientation adopted by the mesogens plays a significant role in the preparation and the operation of these electro-optical devices. Indeed, in the absence of any external electric field, the bulk orientation of the mesogens is completely determined by their anchoring at the confining boundaries. This anchoring may be perpendicular (homeotropic), parallel (planar) or tilted with respect to the surface. Various mechanical and chemical techniques are available to control the orientation of the molecules at the surface [9,10,32,39]. Transitions from one anchoring condition to another may occur when certain parameters of the systems are changed. In this first part of the thesis (Chapters 2 and 3), the focus is on a

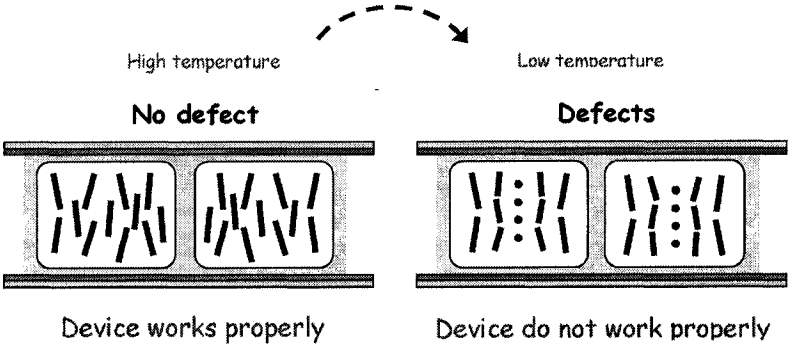

Figure 1–20: Cartoon illustrating the apparition of wall defects in the PDLC film and subsequent ill-functioning of the device due to a temperature driven anchoring transition.

defect structure known as inversion wall that frequently arises during a temperature-driven anchoring transition in a polymer composite film destined for new electro-optical applications (cf. figure 1–20). The objective of the work is to explain various experimental observations made by confocal polarizing microscopy and provide a fundamental understanding of interface-induced defect formation processes of direct impact to electro-optical materials and devices.

The second defect-centered problem examined in this thesis concerns the bio-spinning of spider silk. Spider silk has mechanical properties that are comparable or even superior to the best man-made superfiber: Kevlar. However, in contrast to this industrial high-performance aramid-based fiber, spider silk is ecological and biodegradable. It is manufactured in an aqueous environment (Kevlar is dissolved in sulphuric acid) under benign processing conditions, including ambient temperature and pressure. Accordingly, there is a considerable interest in understanding the design and processing details of silk-precursor materials. Doing so may eventually

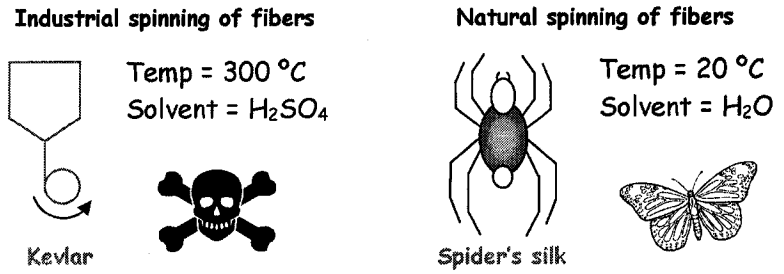

Figure 1–21: Cartoon comparing the spinning technologies of industry and nature for high-performance liquid crystal based-fibers.

lead to the development of environmentally friendly processes for the fabrication of new high-performance fibers. Figure 1–21 show a pictorial comparison between Kevlar and silk fibers.

The spinning apparatus of spiders basically consist of three major regions: a tail where the silk precursor material is synthesized, a central bag where it is stored in a concentrated solution, and a spinning extrusion duct from which the silk fiber is drawn. Spider silk, like Kevlar fiber, is spun from a lyotropic nematic liquid crystalline precursor. The emergence of this mesophase is due to the high concentration of rod-like molecules or aggregates in the watery dope solution. The processing of silk is also known to involve strong changes in orientational order of the nematic liquid crystal phase. These changes are extremely important as they affect the processability of the silk precursor as well as they determine the microstructural details of the solidified fiber and hence its remarkable mechanical properties. Of particular interest is the presence of a series of point defects in the tubular extrusion duct [18, 27]. These defects seem to disappear on approaching the very end of the spinning duct to give a predominantly axial structure. This structure is then retained in the solidified

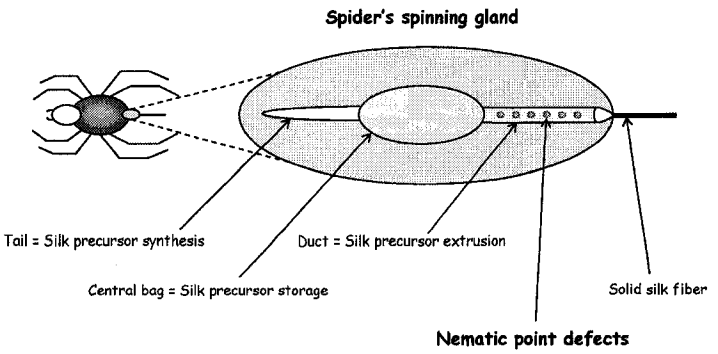

Figure 1–22: Schematic view of the spider silk spinning apparatus.

fiber. Whether the presence of point defects along the extrusion duct of the spinning apparatus of spiders is an 'accident of nature' or a 'necessary ingredient' of the bio-spinning process is unknown at this time. Nevertheless, a better understanding of the overall process is required to improve the actual industrial spinning technique that is unable to produce synthetic fibers with mechanical properties as competitive as the one produced by spiders. In the second part of the thesis (Chapters 4 to 7, the focus is on the static and dynamic properties of nematic point defects confined in cylindrical geometries as they arise along spider extrusion duct. Figure 1–22 provides a diagram of the silk spinning gland.

The unifying theme of this thesis is emergence, stability, and interaction of defects with other defects and with the confining substrates, in engineering devices (PDLCs) and biological processes (silk bio-spinning). In PDLC, the defects of interest are 2D continuous inversion walls, and in the spider spinning process they are singular and non-singular disclination lines and point defects. Hence this thesis covers all the possible defects found in nematic media: 0D, 1D, 2D, singular and

non-singular. The role of substrate-liquid crystal interactions and substrate curvature in the engineering device and in the biological process is also important. In the electro-optical device, the substrate geometry is flat and the defect-nucleation process is driven by a transient re-orientation driven by changes at the interfaces. In the bio-spinning process, the substrate is highly curved and the defect-nucleation process is due to a permanent strong anchoring on a curved interface.

1.5 Methodology and organization

In this thesis, modelling and simulations are used to investigate the behavior of defects and textures in two different nematic-based systems. With the availability of affordable computer power, this approach is becoming increasingly popular and is regularly used to explain and complement available experimental results. One of the forces of the modelling and simulation approach is that it can overcome length and time scales issues that often render experimentations difficult or even impossible to realize. Modelling and simulations is also able to predict scenarios not (yet) realizable in experiments and allow to formulate new hypotheses relatively fast and easily. In the specific study of nematic defects and textures, analytical and numerical solutions are often indispensable to interpret experimental results obtained from complicated *visualizing* techniques such as nuclear magnetic resonance (NMR) or fluorescence confocal polarizing microscopy (FCPM). Three different models are used to simulate the behavior of defects and textures. The choice of model is motivated by the singularity, strength and details of the defect core to be analyzed.

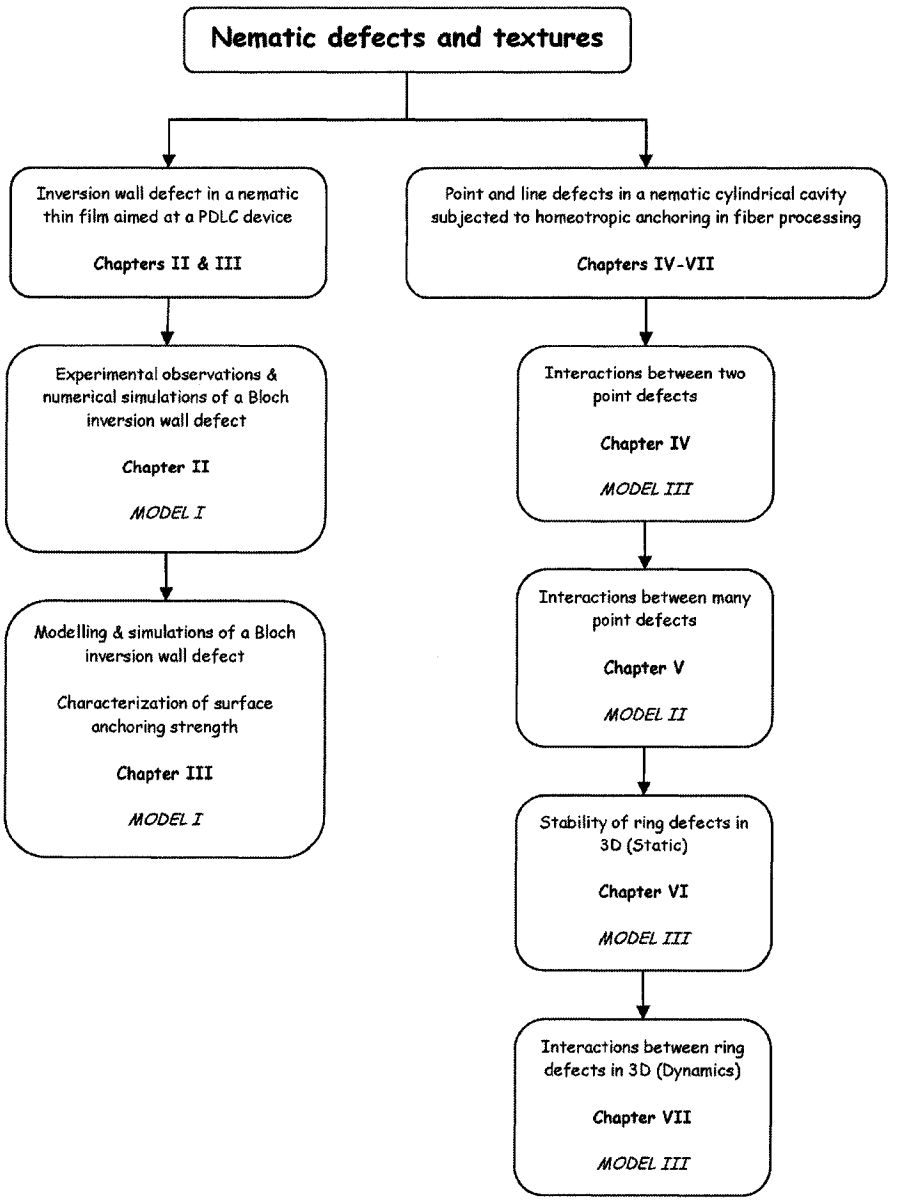

Figure 1–23: Thesis organization.

The organization of this thesis is summarized in figure 1–23. Chapters 2 and 3 treat the problem of inversion wall defects in a polymer-liquid crystal composite thin film intended for a new PDLC-based optical device using the director model I. Chapter 2 presents the published work stemming from a collaboration with the research group of Professor Mohan Srinivasarao at the Georgia Institute of Technology in Atlanta [57]. In this work, the Georgia Tech group contributes the visualization and characterization of the inversion wall defect using fluorescence confocal polarizing microscopy while the computational analysis is my work. Chapter 3 is based on another publication [58] and presents a deeper, more detailed modelling and simulation analysis of the inversion wall problem. An new analytical expression is provided to estimate the anchoring strength at liquid crystal-polymer interfaces. Chapters 4 to 7 concern nematic point and line defects in a cylindrical cavity enforcing homeotropic (i.e. radial) anchoring and is motivated by the need for a better understanding of the texturing undergone by the spider silk precursor throughout a micron-sized tubular extrusion duct. The content of chapter 4 originates from publications [59] and investigates the interactions between two oppositely charged point defects using the Landau-de Gennes tensor approach (Model III). Chapter 5 from [60] considers the interactions between many point defects randomly distributed along the axis of cylindrical cavity subjected to homeotropic anchoring using the director model II. Chapter 6 presents a detailed three-dimensional static study of nematic point, line and ring defects confined in a cylindrical geometry using the Landau-de Gennes model III. This work appears in [61]. The content of chapter 7, which appears in [62], provides a three-dimensional dynamic analysis of ring and point defects using tensor

model III. Finally, chapter 8 summarizes the conclusions and offers the contributions to original knowledge of the thesis. Recommendations for future investigations are also proposed.

REFERENCES

[1] P.S. Drzaic, editor. *Liquid crystal dispersions.* World Scientific Publishing Company, Singapore, 1995.

[2] P.J. Collings. *Liquid crystals: nature's delicate phase of matter.* Princeton University Press, Princeton, NJ, 2001.

[3] M. Kleman and O.D. Lavrentovich. *Soft Matter Physics: An Introduction.* Springer, New York, 2002.

[4] P. Oswald and P. Pieranski. *Nematic and cholesteric liquid crystals: concepts and physical properties illustrated by experiments.* CRC Press, 2005.

[5] K. Okubo, M. Kimura, and T. Akahane. Measurement of genuine azimuthal anchoring energy, in consideration of liquid crystal molecular adsorption on alignment film. *Japan. J. Appl. Phys.*, 42:6428, 2003.

[6] G. Ryschenkow and M. Kleman. Surface defects and structural transitions in very low anchoring energy nematic thin-films. *J. Chem. Phys.*, 64:404, 1976.

[7] A. Sugimura, K. Matsumoto, O.Y. Zhongcan, and M. Iwamoto. Anomalous anchoring effect of nanopolyimide langmuir-blodgett films in a twisted nematic liquid-crystal cell. *Phys. Rev. E*, 54:683, 1996.

[8] V. Vitek and M. Kleman. Surface disclinations in nematic liquid-crystals. *J. Phys. Paris*, 36:59–67, 1975.

[9] H. Yokoyama. Surface anchoring of nematic liquid-crystals. *Mol. Cryst. Liq. Cryst.*, 165:265–316, 1988.

[10] A.A. Sonin. *The surface physics of liquid crystals.* Gordon and Breach, Amsterdam, 1995.

[11] A.M. Donald, A.H. Windle, and S. Hanna. *Liquid crystalline polymers.* Cambridge University Press; 2 edition, 2006.

[12] R.G. Larson. *The structure and rheology of complex fluids.* Oxford University Press, New York, 1999.

[13] L.H. Peebles. *Carbon Fibers - Formation, Structure, and Properties.* CRC, Boca Raton, 1995.

[14] J.E. Zimmer and J.L. White. *Advance in liquid crystals*, volume 5. New York: Academic Press, 1982.

[15] E. Atkins. Silk's secrets. *Nature*, 424:1010, 2003.

[16] J.M. Gosline, M.E. DeMont, and M.W. Denny. The structure and properties of spider silk. *Endeavour*, 10(1):37–43, 1986.

[17] T. Scheibel. Protein fibers as performance proteins: new technologies and applications. *Curr. Opin. Biotech.*, 16:427–433, 2005.

[18] F. Vollrath and D.P. Knight. Liquid crystalline spinning of spider silk. *Nature*, 410:541–548, 2001.

[19] R.F. Foelix. *Biology of spiders.* Oxford University Press, New York, 1996.

[20] J. Turner and C. Karatzas. *Natural fibers, plastics and composites*, chapter 1, Advanced spider silk fibers by biomimicry, pages 11–23. Kluwer Academic Publishers, Dordrecht, 2004.

[21] C. Viney, A.E. Huber, D.L. Dunaway, K. Kerkam, and S.T. Case. *Silk polymers: materials science and biotechnology*, chapter 11, Optical characterization of silk secretions and fibers, pages 120–136. American Chemical Society, Washington, DC, 1993.

[22] T. Scheibel. Spider silks: recombinant synthesis, assembly, spinning, and engineering of synthetic proteins. *Microb. Cell Fact.*, 3:14, 2004.

[23] H.-J. Jin and D.L. Kaplan. Mechanism of silk processing in insects and spiders. *Nature*, 424:1057–1061, 2003.

[24] K. Kerkam, C. Viney, D. Kaplan, and S. Lombardi. Liquid crystallinity of natural silk secretions. *Nature*, 349:596–598, 1991.

[25] D.P. Knight and F. Vollrath. Liquid crystals and flow elongation in a spider's silk production line. *Proc. R. Soc. Lond. B*, 266:519–523, 1999.

[26] F.K. Ko and J. Jovicic. Modeling of mechanical properties and structural design of spider web. *Biomacromolecules*, 5:780–785, 2004.

[27] J.E. Lydon. Silk: the original liquid crystalline polymer. *Liq. Cryst. Today*, 13(3):1–13, 2004.

[28] F. Vollrath. Strength and structure of spiders silks. *Rev. Mol. Biotech.*, 74:67–83, 2000.

[29] C.L. Craig. *Spiderwebs and silk.* Oxford University Press, New York, 2003.

[30] S.A. Wainwright, W.D Biggs, J.D. Currey, and J.M. Gosline. *Mechanical Design in Organims.* Princeton University Press, Princeton, NJ, 1982.

[31] P.G. de Gennes and J. Prost. *The physics of liquid crystals.* Oxford University Press, New York, 1995.

[32] S. Chandrasekhar. *Liquid crystals.* Cambridge University Press, Cambridge, 1992.

[33] M. Doi. *The Theory of Polymer Dynamics.* Oxford University Press, New York, 1998.

[34] M. Kleman. *Liquid Crystallinity in polymers*, chapter 10, Defects and textures in liquid crystalline polymers, pages 365–394. VCH, NY, 1991.

[35] Y. Bouligand. *Physical properties of liquid crystals*, chapter Defects and textures, page 304. Whiley-VCH, Weinhem, 2003.

[36] D. Demus and L. Richter. *Textures of liquid crystals.* Verlag Chemie, New York, 1978.

[37] S. Chandrasekhar and G.S. Ranganath. The structure and energetics of defects in liquid-crystals. *ADVANCES IN PHYSICS*, 35(6):507–596, 1986.

[38] G. Friedel. The mesomorphic states of matter. *Ann. Phys.*, 18(2):273474, 1922.

[39] I. Dierking. *Textures of liquid crystals.* Wiley-VCH Verlag, 2003.

[40] P.E. Cladis and M. Kleman. Non-singular disclinations of strength s=+1 in nematics. *J. Phys.*, 33(5-6):591, 1972.

[41] C.E. Williams, P.E. Cladis, and M. Kleman. Screw disclinations in nematic samples with cylindrical symmetry. *Mol. Cryst. Liq. Cryst.*, 21(3-4):355–373, 1973.

[42] C. Williams, .P Pieranski, and P. E. Cladis. Nonsingular s=+1 screw disclination lines in nematics. *Phys. Rev. Lett.*, 29(2):90, 1972.

[43] I.W. Stewart. *The static and dynamic continuum theory of liquid crystals: a mathematical introduction.* Taylor & Francis, 2004.

[44] T. Asakura, K. Umemura, Y. Nakazawa, H. Hirose, J. Higham, and D. Knight. Some observations on the structure and function of the spinning apparatus in the silkworm bombyx mori. *Biomacromolecules*, 8(1):175–181, 2007.

[45] M. Kleman and O.D. Lavrentovich. Topological point defects in nematic liquid crystals. *Philos. Mag.*, 86(25-26):4117–4137, 2006.

[46] O.D. Lavrentovich, T. Ishikawa, and E.M. Terentjev. Disclination loop in mori-nakanishi ansatz: Role of the divergence elasticity. *Mol. Cryst. Liq. Cryst.*, 299:301–306, 1997.

[47] O.D. Lavrentovich and E.M. Terentiev. Phase-transition with the change of symmetry of topological point-defects (hedgehogs) in a nematic liquid-crystal. *Zh. Eksp. Teor. Fiz.*, 91:2084–2096, 1986.

[48] H. Mori and H. Nakanishi. On the stability of topologically non-trivial point-defects. *J. Phys. Soc. Japan*, 57:1281–1286, 1988.

[49] M. Kleman. *Points, lines and walls: in liquid crystals, magnetic systems and various ordered media.* John Wiley & Sons Inc, 1982.

[50] J. Nehring and A. Saupe. Schlieren texture in nematic and smectic liquid-crystals. *J. Chem. Soc. Faraday Trans. II*, 68(590):1, 1972.

[51] G. Barbero and L.R. Evangelista. *An elementary course on the continuum theory for nematic liquid crystals.* World Scientific Publishing, Singapore, 2000.

[52] A. Rapini and M. Papoular. Distorsion d'une lamelle nmatique sous champ magntique. conditions d'ancrage aux parois. *J. Phys. Coll.*, 30-C4:54, 1969.

[53] C. Liu and N.J. Walkington. Approxiamtion of liquid crystal flows. *SIAM J. Numer. Anal.*, 37:725–741, 2000.

[54] P. Yue, J.J. Feng, C. Liu, and Shen J. A diffuse-interface method for simulating two-phase flows of complex fluids. *J. Fluid Mech.*, 515:293–317, 2004.

[55] B.J. Edwards and A.N. Beris. Order parameter representation of spatial inhomogeneities in polymeric liquid-crystals. *J. Rheo.*, 33:1189–1193, 1989.

[56] A.N. Beris and B.J. Edwards. *Thermodynamics of Flowing Systems.* Oxford University Press, New York, 1994.

[57] J. Zhou, J.O. Park, G. De Luca, A.D. Rey, and M. Srinivasarao. Microscopic observations and simulations of blochwalls in nematic thin films. *Phys. Rev. Lett.*, 97:157801, 2006.

[58] G. De Luca and A.D. Rey. Modelling of bloch wall defects in nematic thin films. *Modelling Simul. Mater. Sci. Eng.*, 14:1397–1407, 2006.

[59] G. De Luca and A.D. Rey. Dynamic interactions between point defects in the spinning extrusion duct of spiders. *J. Chem. Phys.*, 124:144904, 2006.

[60] G. De Luca and A.D. Rey. Structure evolution of spider silk liquid crystalline precursor material. In C.A. Brebbia, M.E. Conti, and E. Tiezzi, editors, *Management of Natural Resources, Sustainable Development, and Ecological Hazards*, pages 381–392. WIT Press IBT Global, 2007.

[61] G. De Luca and A.D. Rey. Ringlike cores of cylindrically confined nematic point defects. *J. Chem. Phys.*, 126:094907, 2007.

[62] G. De Luca and A.D. Rey. Point and ring defects in nematics under capillary confinement. *J. Chem. Phys.*, 127(10), 2007.

CHAPTER 2
Microscopic Observations and Simulations of Bloch Walls in Nematic Thin Films

2.1 Summary

We study Bloch walls defects formed by quenching nematic thin films from planar anchoring to homeotropic anchoring through a temperature-driven anchoring transition. The director profiles of the walls are directly visualized using fluorescence confocal polarizing microscopy, and shown to agree well with the simulation based on the Frank elasticity theory. A pure twist wall exists if the ratio of sample thickness, to surface extrapolation length, p, is smaller than or close to 1; while a diffuse Bloch wall is obtained if p is much greater than 1.

2.2 Introduction

A nematic liquid crystal (LC) possesses long range orientational order along a direction $\mathbf{n}$, known as the director. A wall defect in a nematic phase is a two dimensional defect that separates regions with different director orientation, which usually forms during a fast realignment process. One such example is the Freedericksz transition, where the LC director is realigned by an external field perpendicular to the original alignment [1]. The director can rotate in two opposite directions ($\mathbf{n} = -\mathbf{n}$) in response to the applied field, thus leading to a 180° inversion wall [1,2]. Fig. 2–1(a) shows a schematic director configuration of the so-called Bloch wall [3] consisting of

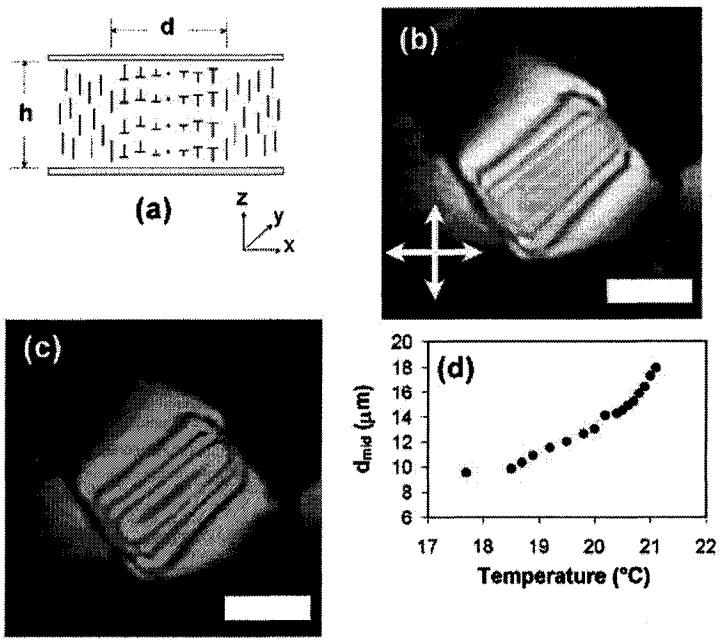

Figure 2–1: (a): A pure twist Bloch wall with the wall thickness d (parallel to x), in a nematic film of thickness h (parallel to z). The head of the nail sign, T, represents the end of the nematic director below the paper plane. (b) and (c): Microscope images (under crossed polarizers and at 45° to the incident polarization) of a Bloch wall in a film of TL205 (h=15 μm) in the xy-plane with (b) white light and (c) monochromatic (532 nm) illumination. The scale represent 10 μm. (d): Wall thickness d_{mid} at $z = 0$ as a function of temperature near the homeotropic-to-planar anchoring transition ($T_t = 21$°C).

180° twist deformation along the x direction. In this figure, d is the Bloch wall thickness and h is the sample thickness. Helfrich first theoretically described the director configuration of inversion walls formed due to the application of a magnetic field [4]. Such wall defects are usually unstable and collapse on themselves in a short time, can be stabilized by the bounding surfaces. Ryschenkow and Kleman first reported that Bloch walls were formed in nematic thin films due to temperature-driven anchoring transitions and remained stable due to weak homeotropic or tilted anchoring [5]. They proposed that the polar anchoring strength (W_p) can be estimated from the geometry of the wall: $W_p \sim K_2 h/d^2$, where K_2 is the twist elastic constant of the nematics. They predicted and experimentally demonstrated that when the surface extrapolation length b (defined as K_2/W_p) is $\geq h$, a pure twist wall is obtained, while a diffuse Bloch wall is obtained when $b \ll h$,. In practice, the wall thickness d, instead of b, may be compared with h to judge which regime the wall belongs to, because d is easily obtained from a microscopic observation. We know of no instances where such a diffuse Bloch wall has been observed.

With the help of fluorescence confocal polarizing microscopy (FCPM), one is able to observe three-dimensional nematic director configuration [6–8]. In the first part of this letter, we show direct visualization of two types of Bloch walls, pure twist walls and diffuse walls, using FCPM technique. This is followed by a simulation of the evolution of the Bloch walls with varying anchoring strengths using Frank elasticity. These simulations agree remarkably well with the experimental FCPM observation.

2.3 Materials and methods

Nematic fluids we used were TL205 (birefringence $\Delta n = 0.22$) and MLC6608 ($\Delta n = 0.083$) from EMerck Industries. Acrylate monomers, n-octyl acrylate, isobonyl acrylate, isooctyl acrylate, and 1,1,1-trimethylol propane triacrylate (Scientific Polymer Products) were used without further purification. The amount of triacrylate was about 10 wt% of the total monomer, which provides the rigidity of LC-polymer composite films through crosslinking reaction. The films were prepared by photopolymerization-induced phase separation reported previously [9]. Such films contain polygonal LC domains of 30-50 μm in width. The film thickness was controlled by glass microbeads of standard sizes (Duke Scientific, 5 and 15 μm in diameter). Bloch walls were formed by quenching a film with a planar alignment from relatively high temperature to homeotropic alignment through a temperature driven transition [8–11].

About 0.003 wt% of a fluorescent dye, pyrromethene 546 (Exciton), was also added to the pre-polymerization mixtures to help the characterization of the director-field using FCPM. The fluorescence transition dipole of the dye was found to align parallel to the local nematic director [7]. The intensity of the fluorescence is maximum when the polarization of the excitation beam, **E**, is parallel to **n**, and minimum when **E** is perpendicular to **n**, with the ratio of 2.2. The dye was excited using Ar^+ laser at 488 nm and the fluorescence was collected at 520-560 nm.

2.4 Results an discussions

A Bloch wall in a composite film of TL205 and poly(isooctyl acrylate) between crossed polars, shows symmetric and parallel color bands with respect to the center yz plane of the wall [Fig. 2–1(b)] when a white light source is used. The color sequence from either edge of the wall to the central plane follows that of the Michel-levy birefringence chart [5, 12]. In monochromatic light, the wall between crossed polarizers shows interference fringes parallel to the wall [Fig. 2–1(c)]. When the wall is perpendicular/parallel to the polarizer, it shows no (best) imaging contrast on removal of the analyzer. This is due because the largest variation in refractive index is obtained when the polarization of light is parallel to the wall. A structure with such a refractive index variation functions as a lens [13] and generates a thin bright line. All of the above observations confirm that the defect is a Bloch wall.

In addition, when the films with Bloch walls are heated close to the homeotropic-to-planar anchoring transition temperature (T_t), the thickness of wall d continuously expands [Fig. 2–1(d)], indicating a decrease in the anchoring strength near T_t.

We choose the low birefringence MLC6608 LC to avoid or minimize optical aberrations in confocal imaging [7, 11, 14] and Bloch walls in MLC6608 + poly(isooctyl acrylate) were imaged using FCPM. By controlling the film thickness relative to the width of the wall, the two types of Bloch walls proposed by Ryschenkow and Kleman were realized, Fig. 2–2.

Fig. 2–2(a) presents the xy and xz optical sections of a pure twist Bloch wall in a 8 μm thick film. The fluorescence emission of the dye is proportional to its absorbance, which in turn depends on the average orientation of the absorption

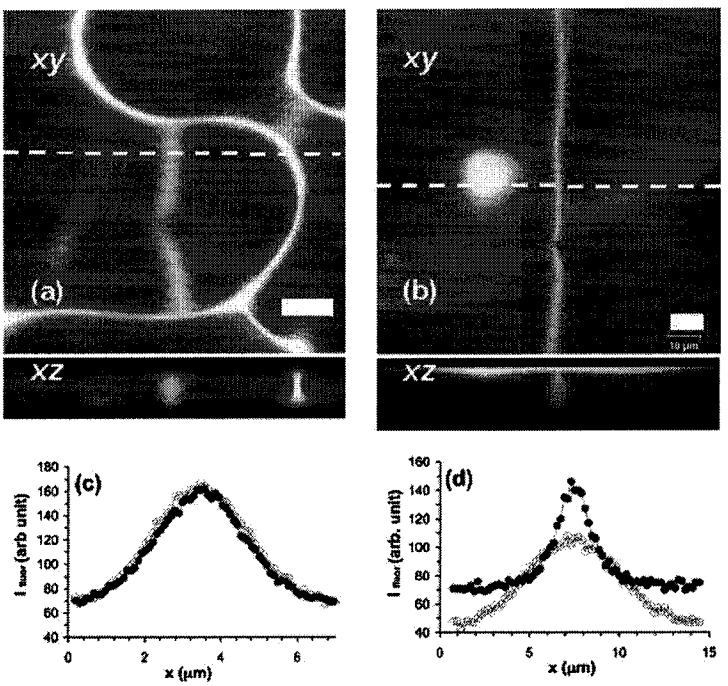

Figure 2–2: Confocal fluorescence images (xy and xz sections) of two Bloch walls: (a) with the extrapolation length (c.a. 4.5 μm) comparable to the sample thickness (8.0 μm); and (b) with the extrapolation length much smaller than the sample thickness (18 μm). The xz section is along the dashed line shown in the xy section which was located 1 μm below the top LC/polymer interface. (c): The fluorescence intensity profiles across the wall in (a) at a depth of 1 μm (•) and 4 μm (○) respectively below the top interface. (d): The fluorescence intensity profiles across the wall in (b) were taken at 1 μm (•) and 5 μm (○) below the top interface. The excitation polarization in (a) and (b) is along y axis. The scale bars shown in (a) and (b) represent 10 μm.

dipoles of the dye molecules with respect to the polarization of the excitation **E**. Since the absorption dipole of the dye is parallel to the local LC director, the measured fluorescence intensity provides us information on the director orientation. The spatial orientation of a nematic director can be specified by two angles: tilt angle ϕ (ϕ = 0 along the substrate normal direction), and azimuthal angle θ (θ = 0 along the orientation of the wall projection in xy plane). Since the azimuthal angle of the director within a Bloch wall is zero, the angle between the director (or the absorption dipole of the dye) and **E** equals $\pi/2 - \theta$ in Fig. 2–2. This simplified relation between the fluorescence intensity of the dye and the orientation of the director, $\mathbf{n}(\theta)$ is described by [15], $I_{fluor}(\theta) \propto I_{em}(\theta) \propto A(\theta) \propto \sin^2(\theta)$ where I_{fluor} is the fluorescence intensity collected by the detector,I_{em} is the emission intensity of the dye, and A is the dye absorbance.

As shown in Fig. 2–2(c), the profiles of the fluorescence intensity across the wall at different depths of the film (open and filled circles) almost overlap with each other, which suggests that the director variation along z axis, $\partial\theta/\partial z$, is negligible [5]. The wall therefore contains only twist deformation, i.e. it is a pure twist wall. Here the wall thickness d (ca. 6 μm) is comparable with the thickness h (8 μm).

Fig. 2–2(b) shows the confocal images of a Bloch wall in a 18 μm-thick film which was made from the same film recipe as Fig. 2–2(a). However, d is a function of z, smallest near both top and bottom substrates, and largest at the middle depth of the film, i.e., showing a barrel-like profile in the xz optical section. The difference between the fluorescence intensity profiles across the wall at different depths (Fig. 2–2(d)) suggests that $\partial\theta/\partial z \neq 0$. In this case, d near either of the substrate is

much smaller than h. Therefore, our result is consistent with Kleman's prediction: a diffuse wall is more stable when the surface extrapolation length b is much smaller than the thickness h.

We now proceed to the simulations of our experiments based on Frank elasticity of the nematic fluid which is expressed as $F = \int_v f_b dv + \int_s f_s ds$. According to Frank's coming formalism, the bulk elastic free energy density, in the one constant approximation, can be written as [1] $f_b = \frac{k}{2}(\nabla \mathbf{n}) : (\nabla \mathbf{n})^T$, where k is a material-dependent elastic constant. The surface free energy density can be derived from Rapini-Papoular expression and reads: $f_s = \frac{w}{2}[1 - (\mathbf{n} \cdot \mathbf{e})^2]$ [16], where w is the surface anchoring strength and $\mathbf{e}$ a unit vector giving some preferred orientation of the nematic director at the surface also called easy axis. Any deviation of the director $\mathbf{n}$ from $\mathbf{e}$ leads to a free energy penalty proportional to w.

A key length scale for this problem is b which is defined as the ratio of bulk to surface energy densities $b = k/w$. According to the continuum theory, the thermodynamically stable states of a system are the ones characterized by free energy minima [17]. In order to study the effect w on the equilibrium structure of Bloch walls, we therefore need to seek director fields that minimize the total free energy. The equations governing this problem are derived using variational calculus [18].

The computational domain considered is a simple 2D slice taken along the thickness of the nematic thin film in the $x - z$ plane. The Euler-Lagrange equation associated with the variational problem is [1]:

$$\frac{\partial f_b}{\partial \mathbf{n}} - \nabla \cdot \frac{\partial f_b}{\partial \nabla \mathbf{n}} = \lambda_b \mathbf{n} \tag{2.1}$$

Where, λ_b is a Lagrange multiplier introduced to fulfill the unit length constraint of $\mathbf{n}$. This equation is numerically solved subject to general boundary conditions:

$$\frac{\partial f_s}{\partial \mathbf{n}} + \nu \cdot \frac{\partial f_b}{\partial \nabla \mathbf{n}} = \lambda_s \mathbf{n} \tag{2.2}$$

where ν is the outward unit normal to the surface and λ_s is the surface Lagrange multiplier [18,19]. In order to facilitate the analysis of the simulation results, the set of equations are non-dimensionalized. The reference length scale in this problem is the thickness of the film and therefore we define the dimensionless position vector as $\bar{r} = r/h$. The key parameter in this problem then becomes the dimensionless surface anchoring strength defined as $p = h/b = (hw)/b$.

The boundaries conditions on the sides of the computational domain are considered to be of the Neumann type to emulate an infinitely wide sample and remove or neglect any lateral surface torques. On the upper and lower surfaces, Eqs. (2.1) and (2.2) are solved with different dimensionless surface anchoring strengths and an easy direction normal to the surfaces.

We examine the structure of an 180° twist wall when the dimensionless surface anchoring strength is $p = 1$. Fig. 2–3(a) shows that for this value of p, the director orientation in the wall is almost independent of the nematic film thickness. The structure of this quasi pure Bloch wall is more easily seen from Fig. 2–3(b), which shows the profiles of n_y, at surface and middle depth of the sample. The profiles of n_y found in Fig. 2–3(b) agree very well with the fluorescence intensity profiles obtained experimentally (Fig. 2–2(c)), where the surface anchoring strength was close to 1.

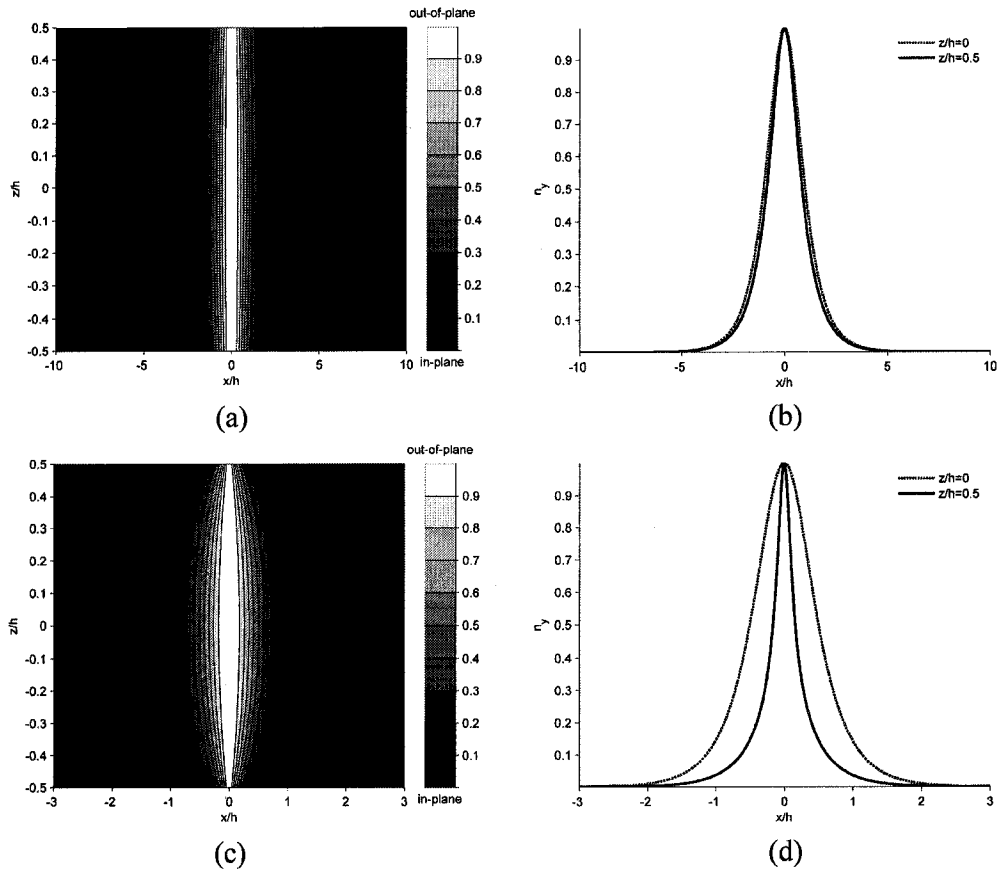

Figure 2–3: (a) Surface plot of the component n_y, when the surface anchoring strength p is equal to 1. The director field is nearly uniform throughout the sample thickness. (b) Profiles of n_y at the surface ($z/h = 0.5$) and midplane ($z/h = 0$) when $p = 1$. (c) and (d) same type of plots for the case $p = 10$ under a strong anchoring.

Figs. 2–3(c) and 2–3(d) present director configurations obtained with for $p = 10$, i.e. strong anchoring. Fig. 2–3(c) illustrates that, as the deviation from the easy axis becomes more costly, the wall deforms in a barrel-like fashion. The wall is clearly wider at middle depth than at surfaces and is referred as diffuse. Fig. 2–3(d) presents two profiles of n_y through the thickness of the film illustrating the net variations of the wall width. Results in Fig. 2–3(d) are consistent with the fluorescence intensity profile shown in Fig. 2–2(d). In the case of $p < 1$, the simulation reveals that there are no variations of the director orientation through the thickness of the nematic film. The 180° twist wall is accordingly a pure Bloch wall and the profiles of ny component at the top surface and the middle plane perfectly coincide as no variations of θ occur. The Bloch wall thickness was much larger than that of the case of $p = 1$, confirming its increase with the anchoring strength decrease.

2.5 Conclusions

In summary, we have shown using FCPM and numerical simulation that when $d \sim h$, a pure twist wall results and when $d < h$ a diffuse wall with a barrel-like profile results. This behavior can be easily understood by looking at the free energy expressions at the surface and in the bulk. The surface energy is minimized as the thickness of the wall becomes smaller, while the bulk elastic energy decreases with decreasing gradients of the director orientations and therefore extends the thickness of the wall. These conflicting mechanisms for the minimization of the system free energy leads to the diffuse Bloch wall structure experimentally observed.

REFERENCES

[1] P.G. de Gennes and J. Prost. *The physics of liquid crystals.* Oxford University Press, New York, 1995.

[2] L. Leger. Walls in nematics. *Mol. Cryst. Liq. Cryst.*, 24(1-2):33–44, 1973.

[3] M. Kleman. *Points, lines and walls.* John Wiley & Sons, New York, 1983.

[4] W. Helfrich. Alignment-inversion walls in nematic liquid crystals in presence of a magnetic field. *Phys. Rev. Lett.*, 21:1518, 1968.

[5] G. Ryschenkow and M. Kleman. Surface defects and structural transitions in very low anchoring energy nematic thin-films. *J. Chem. Phys.*, 64:404, 1976.

[6] D. Voloschenko and O.D. Lavrentovich. Optical vortices generated by dislocations in a cholesteric liquid crystal. *Opt. Lett.*, 25:317, 2000.

[7] I.I. Smalyukh, S.V. Shiyanovskii, and O.D. Lavrentovich. Three-dimensional imaging of orientational order by fluorescence confocal polarizing microscopy. *Chem. Phys. Lett.*, 336:88, 2001.

[8] J Zhou. *Polymer dispersed liquid crystals and Microscopy of Liquid Crystals.* PhD thesis, Georgia Institute of Technology, USA, 2004.

[9] J. Zhou, D.M. Collard, J.O. Park, and Srinivasarao M. Control of the anchoring behavior of polymer-dispersed liquid crystals: Effect of branching in the side chains of polyacrylates. *J. Am. Chem. Soc.*, 124:9980, 2002.

[10] K.R. Amundson and M. Srinivasarao. Liquid-crystal-anchoring transitions at surfaces created by polymerization-induced phase separation. *Phys. Rev. E*, 58:R1211, 1998.

[11] J. Zhou, D.M. Collard, J.O. Park, and M. Srinivasarao. Control of anchoring of nematic fluids at polymer surfaces created by in situ photopolymerization. *J. Phys. Chem. B*, 109:8838, 2005.

[12] F.D. Bloss. *Optical Crystallography.* Mineralogical Soc. Am., Washington, D.C., 1999.

[13] M. Srinivasarao and J.O. Park. Magnetic field induced instabilities in nematic solutions of polyhexylisocyanates. *Polymer*, 42:9187–9191, 2001.

[14] Y. Song. *Study of dye diffusion in fibers by laser scanning confocal microscopy.* PhD thesis, North Carolina State University, 1999.

[15] D. Axelrod. *Methods in Cell Biology*, volume 30. Academic, San Diego, 1989.

[16] A. Rapini and M. Papoular. Distorsion d'une lamelle nmatique sous champ magntique. conditions d'ancrage aux parois. *J. Phys. Coll.*, 30-C4:54, 1969.

[17] G. Barbero and L.R. Evangelista. *An elementary course on the continuum theory for nematic liquid crystals.* World Scientific Publishing, Singapore, 2000.

[18] I. Dahl and A.D. Demeyere. On higher-order variational analysis in one-dimensions and 3-dimensions for soft boundaries. *Liq. Cryst.*, 18:683, 1995.

[19] A. Sugimura, K. Matsumoto, O.Y. Zhongcan, and M. Iwamoto. Anomalous anchoring effect of nanopolyimide langmuir-blodgett films in a twisted nematic liquid-crystal cell. *Phys. Rev. E*, 54:683, 1996.

CHAPTER 3
Modelling of Bloch inversion wall defects in nematic thin films

3.1 Summary

We study the influence of anchoring strength on the structure of Bloch inversion wall defects occurring in nematic thin films during fast temperature-driven anchoring transitions. Numerical simulations show that when the surface extrapolation length b is greater than or comparable to the film thickness h, the wall is homogeneous with a pure twist structure. On the other hand, when the extrapolation length b is smaller than the sample thickness h, the wall is heterogeneous with a barrel-like structure. These results are in very good agreement with recent experimental observations made with fluorescence confocal polarizing microscopy. Additionally, we derive a simple analytical relation to predict the structure of the inversion wall defect in the homogeneous, pure twist, regime. This relation can be used along with optical measurements to simply estimate surface anchoring strengths.

3.2 Introduction

The long range orientational order of nematic liquid crystal systems can be described by a unit vector $\mathbf{n}$, called director, which define the local mean molecular orientation [1]. The structure of nematic films primarily result from a competition between intrinsic ordering and induced surface or interfacial effects but can also be further affected by external applied forces such as electric, magnetic and flow

fields [2]. Given their high sensitivity, nematic liquid crystal systems have structures that are rarely perfect and that often contain defects [3]. Defects, which cause distortions in the director distribution, can be in the form of points (0D), lines (1D) or walls (2D) [1–3].

For example, nematic thin films may exhibit non-singular wall defects called inversion walls in which the directors rotate continuously by π radians or less over a small distance [4]. These inversion walls can cross the depth of the film and emerge on both bounding surfaces. The origin of inversion wall defects is usually a fast reorientation process [4]. Such phenomena can be induced by an external electric or magnetic field [2, 5] but also by a temperature-driven anchoring transition [6–9]. It is stressed that because line and wall defects appear respectively as points and lines in two-dimensional polarized light optical pictures, a confusion is often made in the literature [4, 7].

Most of the nematic liquid crystal applications are based on the fact that, the interfacial director orientation, which is called anchoring, can be controlled by physico-chemical treatments [10–14]. When interfacial torques are sufficiently strong, the director orientation at the bounding surfaces is fixed as function of temperature and is independent of the intrinsic bulk ordering effects. The surface director orientation corresponding to this strong anchoring state is known as easy axis [1, 2]. However, when interfacial torques are not strong enough to impose a well-defined orientation at the surfaces, that is the anchoring is weak, the surface director orientation deviates from the easy axis to allow the relaxation of bulk distortions and the lowering of the overall system free energy. The energy price paid by the system for this deviation

of the interface director orientation from the easy axis is called anchoring energy or anchoring strength and it is a function of temperature [14].

During a temperature-driven anchoring transition, the preferred director orientation at the surface is quickly modified; since the director is apolar, *i.e.* $\mathbf{n}$ is equivalent $-\mathbf{n}$, it has two opposite ways of rotating to orient parallel to the new easy axis and therefore an inversion wall defect can be trapped between two adjacent domains with opposite senses of rotation [6–9]. Because of their analogy with wall defects found in ferromagnetic materials, the inversion walls found in nematic liquid crystals are also called Bloch or Néel inversion wall defects depending on the type of elastic curvature involved [3].

Recently, the structure of Bloch inversion wall defects in nematic thin films has been studied using fluorescence confocal polarizing microscopy [15, 16]. This technique allow a true three-dimensional investigation of the director distribution unlike conventional polarizing microscopy [17]. The experimental results have revealed that in the regime where the extrapolation length b is smaller than the film thickness h, the wall tend to acquire a barrel-like structure. In this chapter, we verify, confirm and explain these experimental observations using simple modelling and simulations. Also, we derive an analytical expression characterizing the structure of the wall as function of the anchoring strength. This expression can be used in conjunction of experimental data to get a direct estimation of the anchoring energy.

The chapter is organized as follows: Section 3.3 presents the theoretical ingredients of the nematic liquid crystal model; Section 3.4 outlines the computational

modelling aspects; Section 3.5 reports the numerical results and analysis of the variational problem; finally Section 3.6 provides conclusions.

3.3 Governing nematostatics equations

In this section we present the necessary theoretical background to study the statics of a nematic liquid crystal thin film. Since the inversion wall defects of interest are non-singular, the director, *i.e.* vector, approach to the nemato-elasto-dynamics is used; we emphasize that for the objectives of this chapter, the scalar order parameter [1] that measures molecular alignment along the director plays no role. The total free energy F of such bounded system is the sum of bulk and surface terms:

$$F = \int_V f_b dV + \int_S f_s dS \tag{3.1}$$

According to Frank's formalism, the bulk elastic free energy density can be written, in the isotropic elasticity approximation as [12]:

$$f_b = \frac{K}{2} (\nabla \mathbf{n}) : (\nabla \mathbf{n})^T \tag{3.2}$$

where K is the Frank elastic constant [1]; the isotropic elasticity approximation assumes that the splay, twist, bend, and saddle-splay elastic constants are all equal; as shown below this approximation captures the main features of the experimental results; we emphasize that elastic anisotropy [1] is not the driving force of the phenomena we wish to model and only contribute to unimportnat small deviations. The

surface free energy density due to Rapini-Papoular [18] reads:

$$f_s = \frac{W(T)}{2}\left[1 - (\mathbf{n}\cdot\mathbf{e})^2\right] \tag{3.3}$$

where *W(T)* is the temperature-dependent surface anchoring strength and **e** is unit of vector representing the easy axis, *i.e.* the preferred orientation of the nematic director at the surface as it minimizes the free energy. More general expressions for f_s are found in the literature [1,2,14], but equation (3.3) is able to describe well the experimentally observed phenomena. As shown below, the minimum model given by equations (3.1) and (3.2) captures the main experimental features [15] and more detailed anisotropic or mesoscopic models are unnecessary.

Any deviation of the director **n** from the easy axis **e** leads to a free energy penalty proportional to the surface anchoring strength W. The ratio of bulk to surface energy densities defines an internal length scale known as the surface extrapolation length b:

$$b = \frac{K}{W} \tag{3.4}$$

In a sample of characteristic bulk size h it follows that when $h \gg b$, F_b is negligible when compared to F_s and the surface director is aligned along the easy axis ($\mathbf{n} = \mathbf{e}$). Otherwise the surface director is oriented along a direction that minimizes F; here F_b and F_s are the first and second integral in equation (3.1).

The equilibrium director field is the one that minimizes the total free energy [19]. The nematostatics governing equations are derived from a variation of the director

[20] and read:

$$\delta F = \int_V \left(\frac{\partial f_b}{\partial \mathbf{n}} - \nabla \cdot \frac{\partial f_b}{\partial \nabla \mathbf{n}} - \lambda_b \mathbf{n} \right) \delta \mathbf{n} dV + \int_S \left(\frac{\partial f_s}{\partial \mathbf{n}} + \mathbf{N} \cdot \frac{\partial f_b}{\partial \nabla \mathbf{n}} - \lambda_s \mathbf{n} \right) \delta \mathbf{n} dS \quad (3.5)$$

where $\mathbf{N}$ is a vector representing the unit normal to the surface; λ_b and λ_s are Lagrange multipliers introduced to fulfill the unit length constraint on the nematic director $\mathbf{n}$ in the bulk at the surface on the system respectively. Minimization of the variations leads to the condition $\delta F = 0$ and the corresponding Euler-Lagrange governing equations for the problem read [20]:

$$\frac{\partial f_b}{\partial \mathbf{n}} - \nabla \cdot \frac{\partial f_b}{\partial \nabla \mathbf{n}} = -K \nabla^2 \mathbf{n} = \lambda_b \mathbf{n} \quad (3.6)$$

$$\frac{\partial f_s}{\partial \mathbf{n}} + \mathbf{N} \cdot \frac{\partial f_b}{\partial \nabla \mathbf{n}} = -W (\mathbf{n} \cdot \mathbf{e}) \mathbf{e} + \mathbf{N} \cdot K \nabla \mathbf{n} = \lambda_s \mathbf{n} \quad (3.7)$$

Equations (3.6) and (3.7) are known as the bulk and surface torque balance equations, respectively [1].

3.4 Computational modeling

In order to study the effect of the temperature dependent surface anchoring strength W on the equilibrium structure of an inversion wall, we solve equations (3.6) and (3.7). The geometry considered for the study of this problem is a simple rectangular domain representing a slice of nematic material of thickness h confined between two parallel plates where nematic molecules are weakly anchored. The width of the computational domain is varied in function of the surface anchoring strength value (Top and bottom boundaries). Figure 3–1 defines the geometry and the coordinate system. In this figure, we have also represented the director field of a

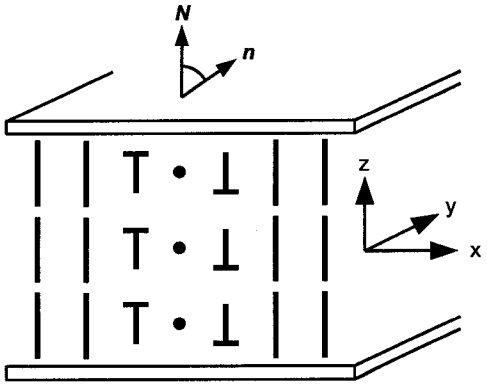

Figure 3–1: Schematic of the computational domain along with the dot-nail representation of the director field in a pure homogeneous Bloch wall. In this figure the segments and the dots indicate in-plane and out-of-plane directors respectively. The nails represent intermediate orientations.

pure twist Bloch wall using the dot-nail convention. Directors being normal to the figure plane are drawn as points, directors parallel to the plane are shown as segments of constant length and directors with intermediate orientations are represented as nails [3].

To adimensionalize the problem we scale distances with the gap thickness h and the computational domain is then a rectangle of unit height (in z-direction) and whose width (in x-direction) is chosen so as to eliminate lateral effects. The reduced position vector is hence:

$$\bar{r} = \frac{r}{h} \tag{3.8}$$

The key parameter in this problem is the dimensionless surface anchoring strength defined as:

$$p = \frac{h}{b} = \frac{hW}{K} \tag{3.9}$$

where b is the previously identified surface extrapolation length. The governing dimensionless equation is:

$$-\bar{\nabla}^2\mathbf{n} = \lambda_b\mathbf{n} \tag{3.10}$$

where the bar over the Nabla symbol indicates that the operator is dimensionless. The corresponding boundary condition at nematic thin film surfaces (upper and lower boundaries of the rectangular computational domain) is:

$$-p\,(\mathbf{n}\cdot\mathbf{e})\,\mathbf{e} + \mathbf{N}\cdot\bar{\nabla}\mathbf{n} = \lambda_s\mathbf{n} \tag{3.11}$$

On the sides of the computational domain we have employed Neumann boundaries so as to emulate an infinitely wide sample and get rid of any undesired lateral torques. This boundary condition reads:

$$\mathbf{N}\cdot\bar{\nabla}\mathbf{n} = \lambda_s\mathbf{n} \tag{3.12}$$

Also, for simplicity we shall consider π radians inversion walls and accordingly the easy director axis is chosen to be parallel to the unit normal of the film surface, *i.e.* $\mathbf{e} = \mathbf{N}$. We remind the reader that the total rotation of the director across an inversion wall can be however less than π radians [8].

3.5 Results and discussions

3.5.1 Anchoring strength-structure relationship in Bloch walls

Equations 3.10 and 3.11 were solved using the standard Galerkin finite element method. The solutions are classified into two asymptotic regimes:

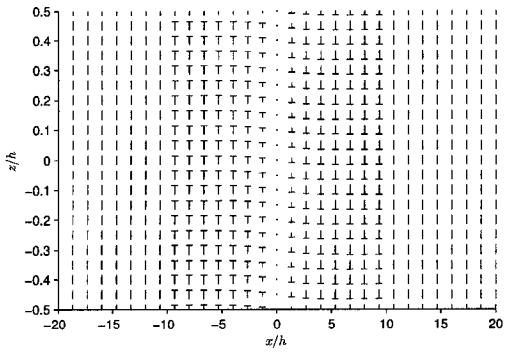

Figure 3–2: Director plot of a Bloch inversion wall for $p = 0.1$ using the dot-nail convention. The inversion wall is a homogeneous twist wall as the director orientation only varies along the wall width: $\mathbf{n} = \mathbf{n}(x)$.

1. Homogeneous wall regime ($p \leq 1$): here the bulk energy dominates and the director field is practically one dimensional: $\mathbf{n} = \mathbf{n}(x)$. The weak anchoring results in a surface director dictated mainly by bulk distortions.
2. Heterogeneous wall regime ($p > 1$): here the surface energy dominates and the director field is two dimensional: $\mathbf{n} = \mathbf{n}(x, z)$. The stronger anchoring results in a surface director dictated by a competition between surface and bulk torques.

Homogeneous wall regime ($p \leq 1$). We first report the computed structure of a Bloch wall defect in the homogeneous regime, *i.e.* the film thickness h is smaller or equal to the surface extrapolation length b. As observed experimentally [8, 15], in this regime, the structure of the inversion wall is uniform throughout the thickness of the film. The wall defect presents mainly twist deformation and we shall referred it to as pure twist wall. Figure 3–2 shows the structure of a pure twist wall obtained with a dimensionless anchoring strength $p = 0.1$. Figure 3–3 presents a contour plot of the out-of-plane component of the director field n_y. Parallel levels of gray scale

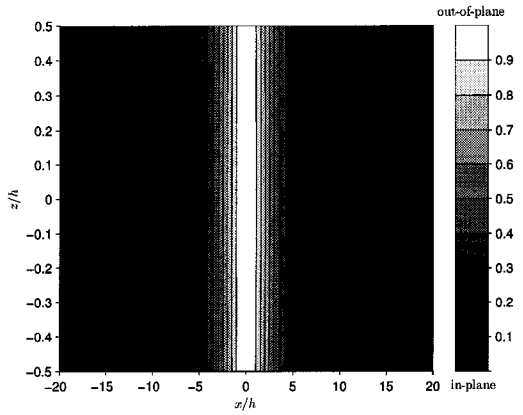

Figure 3–3: Contour plot of the out-of-plane component of the director n_y, when the dimensionless surface anchoring strength p is equal to 0.1. The director field is uniform through out the thickness of the film forming a pure homogeneous twist wall.

readily indicate that the director distribution is constant across the depth of the slab. Figure 3–4 shows the director's out-of-plane component n_y at the mid-plane ($z = 0$) and at the surface ($z = 1$) as a function of the dimensionless position x/h. The two profiles perfectly superimpose and are in accordance with fluorescence intensity signals recently obtained trough confocal polarizing microscopic observations [15].

Heterogeneous wall regime ($p > 1$). We now discuss the structure of the Bloch wall defect in the heterogeneous regime where the sample thickness h is greater than the surface extrapolation length b. Recent observations made with fluorescence confocal polarizing microscopy have shown that the wall defects tend to adopt a barrel-like structure in this regime [15]. Numerical solutions confirm that this type of solution can be in fact predicted with a simple nematic liquid crystal director

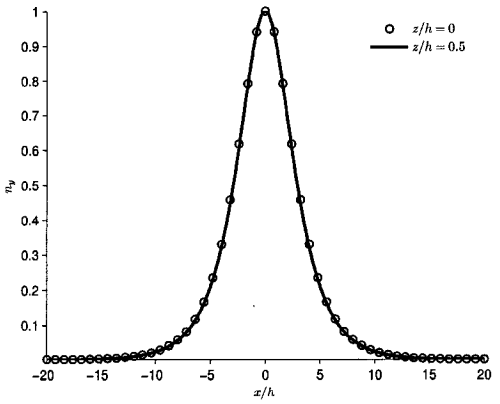

Figure 3–4: Profiles of the out-of-plane plane component of the director n_y at the surface ($z/h = 0.5$) and middle plane ($z/h = 0$), for $p = 0.1$. The result is representative of the homogeneous wall regime ($p \leq 1$). The profiles perfectly coincide as the director field is independent of the sample thickness.

model without the need of using tensor models or molecular order parameter models. Simulations show that as p becomes greater than 1, the pure twist homogeneous wall evolve into a diffuse heterogeneous wall. In contrast to the pure homogeneous twist wall, the diffuse heterogeneous wall does not have a constant structure across its thickness. The wall is thinner at the bounding surfaces than at middle depth. Figure 3–5 shows the computed structure of the Bloch wall when the dimensionless anchoring strength parameter $p = 10$. The figure clearly illustrates that the distance required by the director to rotate by π radians varies along the thickness of the film. This particular distribution of the director across the wall defect is responsible for the typical barreling pattern experimentally observed in microscopy images [15]. Figure 3–6 shows the barrel-like pattern of the diffuse heterogeneous wall though the contour plot of the out-of-plane component of the director field. The profiles of the

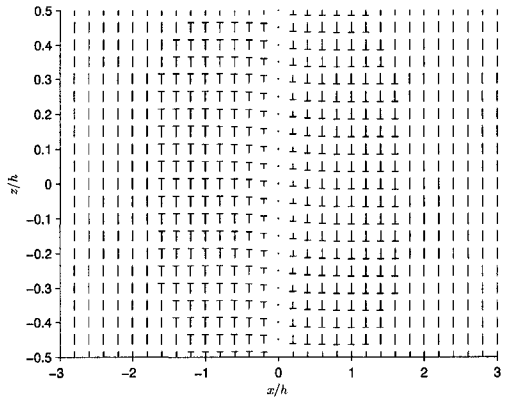

Figure 3–5: Director plot of a twist inversion wall for $p = 10$. The inversion wall is here a heterogeneous diffuse twist wall, and the director field is now two-dimensional: $\mathbf{n} = \mathbf{n}(x, z)$.

out-of-plane component across the wall at the middle depth and surface levels are shown in figure 3–7. It is seen from this figure that the inversion of the directors is not uniform throughout the thickness of the sample and that the rotation of the director are more localized at the surface than in the bulk. This can be understood by observing that the surface energy gets minimized as the wall width shrinks, while the bulk energy minimization requires the opposite; these competing orientational mechanism lead to this distorted twist wall structure.

3.5.2 Theoretical analysis of the homogeneous wall regime

The purpose of this section is to present a simple non-linear model that can be solved analytically and that captures the steady state director structure of the pure twist inversion wall shown in figure 3–1. The analytical model sheds light into the competing surface and bulk mechanisms and offer a direct view of the parametric

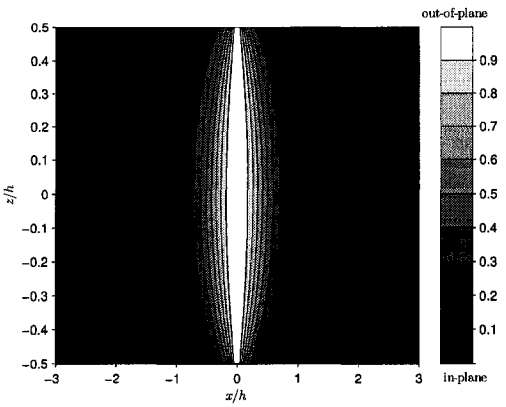

Figure 3–6: Contour plot of the out-of-plane component of the director n_y, when the dimensionless surface anchoring strength p is equal to 10. The director field is clearly varying along the thickness of the nematic film and displays the barrel-like pattern characteristic of heterogeneous twist inversion walls.

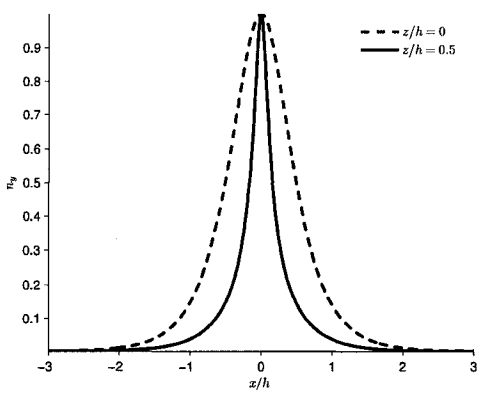

Figure 3–7: Profiles of the out-of-plane plane component of the director n_y at the surface ($z/h = 0.5$) and middle plane ($z/h = 0$) when $p = 10$. The barreling of the wall is clearly visible; the wall is larger at the middle plane than at the surface.

dependence. Numerical solutions of the variational problem (equations (3.10) and (3.11)) shows that, when the film thickness h is smaller or comparable to the surface extrapolation length b, it is reasonable to assume that the structure of the wall is homogeneous along the film thickness (the z-direction); in other words: $\mathbf{n} = \mathbf{n}(x)$. Under such assumption we can write the total free energy per unit length along the y-direction as:

$$F = \int_{-\infty}^{\infty} f dx = \int_{-\infty}^{\infty} (h f_b + 2 f_s)\, dx \tag{3.13}$$

Parameterizing the unit vector with the director angle θ:

$$\mathbf{n}(x) = \cos\theta(x)\, \delta_z + \sin\theta(x)\, \delta_y \tag{3.14}$$

the bulk energy density becomes:

$$f_b = \frac{K}{2}\left(\frac{d\theta}{dx}\right)^2 = \frac{K}{2}\theta'^2 \tag{3.15}$$

For a π radian inversion wall parallel to the $y-z$ plane with the easy axis along the z-direction ($\mathbf{e} = \delta_z$) the surface free energy density takes the following simple form:

$$f_s = \frac{W}{2}\sin^2\theta \tag{3.16}$$

Using the fact that the integrand f (defined in equation (3.13)) does not depend explicitly on x, a simple variational calculation leads to [19]:

$$c_1 = \theta'\frac{\partial f}{\partial \theta'} - f = \frac{Kh}{2}\theta'^2 - W\sin^2\theta = const \tag{3.17}$$

The constant c_1 can be determined from the boundary conditions; at $x = -\infty$, $\theta = 0$ and $\theta' = 0$ while at $x = \infty$, $\theta = \pi$ and $\theta' = 0$. These conditions equivalently lead to

$c_1 = 0$ and therefore the director angle obeys:

$$\theta'^2 = \frac{2W}{Kh}\sin^2\theta \tag{3.18}$$

Since θ', $sin\theta$ and the constants are all greater than zero in the interval of interest, it is possible to write the following ordinary differential equation:

$$\theta' = \sqrt{\frac{2W}{Kh}}\sin\theta \tag{3.19}$$

Integration of this differential equation gives:

$$\ln\tan\frac{\theta}{2} = \sqrt{\frac{2W}{Kh}}x + c_2 \tag{3.20}$$

Given that at $x = 0$, $\theta = \pi/2$, the constant of integration c_2 is also found to be zero. Therefore, the final solution for the profile of director angle in the π radians inversion wall reads:

$$\theta = 2\text{atan}\left[\exp\left(\sqrt{\frac{2W}{Kh}}x\right)\right] \tag{3.21}$$

In terms of our dimensionless anchoring strength p this expression reads:

$$\theta = 2\text{atan}\left[\exp\left(\sqrt{2p}\bar{x}\right)\right] \tag{3.22}$$

Figure 3–8 shows the profiles of the out-of-plane component of the director n_y corresponding to the numerical solution of equations (3.10) and (3.11) and to the analytical solution given through equation (3.22). It can be seen from this figure that the approximate analytical solution give a pretty accurate description of the wall structure in the homogeneous regime ($p < 1$). Consequently, if one has experimental data characterizing the structure of the wall obtained with the help of confocal

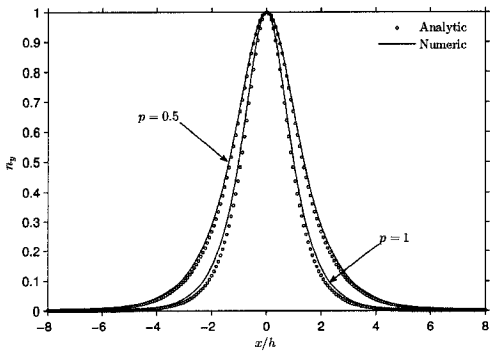

Figure 3–8: Profiles of the out-of-plane component of the director n_y obtained through the approximate analytical and exact numerical solutions for two values of the dimensionless anchoring strength in the regime $p \leq 1$.

polarizing microscopy, one can use equation (3.22) along with a standard non-linear least square fitting procedure and estimate the corresponding anchoring strength. Despite the development of new sophisticated methods [14], anchoring strength is still regularly estimated using inversion wall-based methods [21–23] and therefore the above describes method may found some practical applications.

3.6 Conclusions

We have investigated the influence of anchoring strength on the structure of a Bloch inversion wall using numerical simulations and simple variational analysis. It was shown that when $p \leq 1$, the width of the wall is uniform throughout the thickness of the film. As the dimensionless anchoring strength increases toward unity, the width of the wall globally decreases. In the regime where $p > 1$, the structure of the inversion wall becomes two-dimensional; the barreling of the wall, experimentally observed using fluorescence confocal polarizing microscopy [15] is confirmed by the

numerical simulations of a simple model. The barrel-like structure solution can be understood by noticing the antagonist director field minimizing the surface and bulk energies. The surface energy is minimized as the width of the wall becomes thinner while the bulk elastic energy reduces with gradients of the director orientations and therefore by expanding the width of the wall. In addition, we have shown that in the regime $p \leq 1$, a simple expression can be obtained to describe the structure of the inversion wall as a function of the anchoring strength. This equation can be, in turn, be used for a direct estimation of anchoring strength using a standard data fitting procedure given experimental data describing the structure of the wall.

REFERENCES

[1] P.G. de Gennes and J. Prost. *The Physics of Liquid Crystals.* Oxford University Press, New York, 1995.

[2] S. Chandrasekhar. *Liquid crystals.* Cambridge University Press, Cambridge, 1992.

[3] Y. Bouligand. *Physical properties of liquid crystals*, chapter Defects and textures, page 304. Whiley-VCH, Weinhem, 2003.

[4] D. Demus and L. Richter. *Textures of liquid crystals.* Verlag Chemie, New York, 1978.

[5] W. Helfrich. Alignment-inversion walls in nematic liquid crystals in presence of a magnetic field. *Phys. Rev. Lett.*, 21:1518, 1968.

[6] M. Kleman and C. Williams. Anchoring energies and nucleation of surface disclination lines in nematics. *Phil. Mag.*, 28:725–31, 1973.

[7] J. Nehring and A. Saupe. Schlieren texture in nematic and smectic liquid-crystals. *J. Chem. Soc. Faraday Trans. II*, 68(590):1, 1972.

[8] G. Ryschenkow and M. Kleman. Surface defects and structural transitions in very low anchoring energy nematic thin-films. *J. Chem. Phys.*, 64:404, 1976.

[9] V. Vitek and M. Kleman. Surface disclinations in nematic liquid-crystals. *J. Phys. Paris*, 36:59–67, 1975.

[10] J. Cognard. Alignment of nematic liquid crystals and their mixtures. *Mol. Cryst. Liq. Cryst. Suppl. Ser.*, 78:1, 1982.

[11] B. Jerome. Surface effects and anchoring in liquid-crystals. *Rep. Prog. Phys.*, 54:391, 1991.

[12] M. Kleman and O.D. Lavrentovich. *Soft matter physics: an introduction.* Springer, New York, 2002.

[13] A.A. Sonin. *The surface physics of liquid crystals.* Gordon and Breach, Amsterdam, 1995.

[14] H. Yokoyama. Surface anchoring of nematic liquid-crystals. *Mol. Cryst. Liq. Cryst.*, 165:265–316, 1988.

[15] J. Zhou. *Polymer dispersed liquid crystals and microscopy of liquid crystals.* PhD thesis, Georgia Institute of Technology, USA, 2004.

[16] J. Zhou, J.O. Park, G. De Luca, A.D. Rey, and M. Srinivasarao. Microscopic observations and simulations of blochwalls in nematic thin films. *Phys. Rev. Lett.*, 97:157801, 2006.

[17] I.I. Smalyukh, S.V. Shiyanovskii, and O.D. Lavrentovich. Three-dimensional imaging of orientational order by fluorescence confocal polarizing microscopy. *Chem. Phys. Lett.*, 336:88, 2001.

[18] A. Rapini and M. Papoular. Distorsion d'une lamelle nmatique sous champ magntique. conditions d'ancrage aux parois. *J. Phys. Coll.*, 30-C4:54, 1969.

[19] G. Barbero and L.R. Evangelista. *An elementary course on the continuum theory for nematic liquid crystals.* World Scientific Publishing, Singapore, 2000.

[20] A. Sugimura, K. Matsumoto, O.Y. Zhongcan, and M. Iwamoto. Anomalous anchoring effect of nanopolyimide langmuir-blodgett films in a twisted nematic liquid-crystal cell. *Phys. Rev. E*, 54:683, 1996.

[21] T. Akahane, H. Kaneko, and M. Kimura. Novel method of measuring surface torsional anchoring strength of nematic liquid crystals. *Japan. J. Appl. Phys.*, 35:4434, 1996.

[22] S. Oka, T. Mitsumoto, M. Kimura, and T. Akahane. Relationship between surface order and surface azimuthal anchoring strength of nematic liquid crystals. *Phys. Rev. E*, 69:061711, 2004.

[23] K. Okubo, M. Kimura, and T. Akahane. Measurement of genuine azimuthal anchoring energy, in consideration of liquid crystal molecular adsorption on alignment film. *Japan. J. Appl. Phys.*, 42:6428, 2003.

CHAPTER 4
Dynamic interactions between nematic point defects in the spinning extrusion duct of spiders

4.1 Summary

Spider silk fibers have remakable mechanical properties as a result of an ultra-optimized spinning process. Silk fibers are spun from a lyotropic nematic liquid crystalline anisotropic fluid phase which undergoes significant structural changes throughout the spinning pathway. In the silk extrusion duct, those structural changes are expected to be driven by elastic mediated interactions between point defects. In this work, the interaction between two point defects of opposite topological charges located on the axis of a cylindrical cavity is studied using a tensor order parameter formalism. Distinct regimes leading to defect annihilation and structural transitions are described in details. The driving force setting the defects in motion is also examined. The different results suggest that the tensorial approach is primordial in describing the complicated physics of the problem. The phenomenon described is important to the understanding of the process-induced structuring of silk fibers and to defect physics in a more general context.

4.2 Introduction

Spider silks enjoy mechanical properties that are comparable or even superior to the best man-made superfibers such as Kevlar or Twaron [1–3]. However, in contrast

to industrial high-performance fibers, silks are ecological: they are biodegradable while manufactured in an aqueous environment under benign processing conditions, including ambient temperature and pressure [4–6]. Accordingly, there is a considerable interest in understanding the design and processing details of silk-precursor materials. Doing so may eventually lead to the development of environmentally friendly processes for the fabrication of new high-performance fibers [7–11].

Spider silks, like the majority of high-performance industrial fibers, are spun from a lyotropic nematic liquid crystalline precursor [2, 7, 8, 12, 13]. The emergence of this mesophase (*i.e.*, intermediate phase) is due to the high concentration of rod-like molecules or aggregates in the watery dope solution. A nematic mesophase can flow as a liquid while possessing at the same time some degree of orientational order as a crystal [14, 15]. This orientational order is characterized by the tendency that have neighboring rod-like molecules to spontaneously orient their long axis approximately in parallel along a common direction. This preferred molecular orientation is usually local, varying from subregion to subregion in the medium due to elastic effects coupled with geometrical and interfacial constraints. Hence, the orientational order of nematic liquid crystals is often described in terms of a unit vector field $\mathbf{n}(\mathbf{r})$, called director field (where $\mathbf{r}$ is the position vector), giving the local average preferred orientation of the molecules [14, 15].

The orientational order of the liquid crystalline dope is known to significantly change along the silk spinning pathway and particularly in the tubular extrusion duct just before the draw down of the fiber [2, 16–19]. This evolution of orientational order is extremely important because it determines the micro-structural details of the

solidified silk fiber, and hence its remarkable mechanical properties. The structural changes are also important with respect to the processability of the material as they affect its viscosity [2, 12, 13, 16–19].

Observations made by polarized light microscopy in the spider tubular extrusion duct indicate the presence of a stable escaped radial structure with point defects (ERPD) [2, 16–20]. The ERPD configuration consist in an array of point defects of alternating type periodically distributed along the axis of the cylindrical cavity [21]. Nematic defects can generally be thought as singular regions where the director field $\mathbf{n}(\mathbf{r})$ cannot be uniquely defined and where ordering melts. The two type of point defects found in the ERPD texture are the radial and hyperbolic hedgehogs. These point defects bear topological charges of strength $+1$ and -1 respectively. The magnitude and sign of the topological charge indicates respectively the amount and sense of director rotation on encircling the defect. On approaching the very end of the spinning duct this ERPD structure is evolving into a defect-free predominantly axial structure corresponding, presumably, to an escaped radial (ER) structure [16]. This later configuration is retained in the solidified fiber [16]. Figure 4–1 shows the typical director fields corresponding to (a) the ERPD and (b) ER structures. Note that the pattern of the ERPD structure can be found periodically repeated in the extrusion duct.

The (meta)stability of the ERPD structure as well as its transition to the ER structure are governed by the interactions between the point defects. [14] These interactions, that are mediated by elastic deformations of the material and affected by geometry, anchoring orientation and strength, as well as external fields (in particular

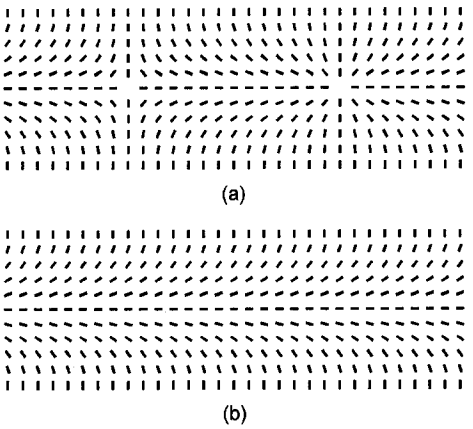

Figure 4–1: Schematic of the director fields $\mathbf{n}(\mathbf{r})$ corresponding to the ERPD (a) and ER (b) structures. In (a), the left and right point defects are respectively corresponding to the hyperbolic and radial hedgehogs. Note that the director is undefined in the core of each point defects.

flow field), can cause the point defects to move along the axis of the cavity. It is well known that when two defects of opposite topological charges are sufficiently close one another they usually attract until they coalesce and finally annihilate, leaving no trace of their previous existence. When, on the other hand, defects are well separated they usually do not feel any mutual attraction and stay immobile. It is therefore crucial to elucidate the properties of the elastic-distortion-mediated interactions between the point defects in order to better understand the process-induced structural transition occurring in the extrusion duct of spiders.

The problem of nematic point defect interactions in cylindrical capillaries has a long history [22–24]. Nematic hedgehogs and their corresponding ERPD configuration are regularly observed when nematic liquid crystals are confined in cylindrical tubes with lateral surfaces enforcing strong radial anchoring (*i.e.*, the molecules are

forced to orient radially at the surface). Generally theoretical and computational studies have considered a pair of oppositely charged point defects rather than a whole array. The annihilation of two nematic point defects of opposite charge consist of three distinct regimes: the pre-collision, the collision, and the post-collision stages. So far studies have been mostly focusing on the pre-collision regime where the defect are well separated [25]. It has been shown both, experimentally and theoretically, that the defects annihilate if their separation is approximately less than the diameter of the tube. The situation is however far less clear when the defects are separated by more than a diameter. Some experimental and theoretical works [26–29] seem to indicate that the defects tend to stay immobile at large separating distance (*i.e.*, the interaction force vanishes) while other studies rather support the defect repulsion hypothesis [30–32].

The collision and post-collision regimes and more generally the dynamics of point defects annihilation has been very little studied so far [25, 33]. Moreover, the analytical and numerical studies using the continuum theories have been generally using a vectorial description of the orientational order. As we will explained in more details in the next section this type of approach present significant drawbacks in the description of defect dynamics and defect-defect interactions. To overcome these limitations, we investigate the dynamic interaction/annihilation of two nematic point defects using a tensorial continuum approach.

This chapter is organized as follows. Section 4.3 gives the theoretical background necessary for modeling structural dynamics relevant to spider silk processing. Section 4.4 presents the numerical results. Finally, section 4.5 draws conclusions on the

work presented.

4.3 Modeling

4.3.1 Geometry

In order to study the problem of process-induced structuring and structure evolution in the extrusion spinning duct of spiders, the interaction between two nematic point defects of opposite topological charges confined in a cylindrical capillary is considered. The problem presents an obvious rotational symmetry around the axis of the cavity which allows to considerably reduce the computational space. The dynamic interaction between the point defect pair is therefore investigated in a simple two dimensional rectangular domain representing the upper half part of a longitudinal cross section through the tube and accordingly a cylindrical coordinate system (z, r) is considered. The width and height of the domain correspond respectively to the length Z and radius R of the cylindrical cavity.

4.3.2 Tensor order parameter Q_{ij}

The continuum nemato-dynamics equation describing the structure evolution of a nematic liquid crystal is typically derived from the minimization of a (visco)-elastic free energy equation. In the simplest continuum approach (Frank theory), the orientational order parameter appearing in the (elastic) free energy of the nematic liquid crystal phase is the unit vector field $\mathbf{n}(\mathbf{r})$. This director field gives an average preferred orientation of the rod-like molecules in each subregion of the nematic liquid crystal phase. This approach works generally well except close to defect cores where

the nematic ordering suffers important distortions and melts. Indeed, one important restriction of the vectorial description of the nematic ordering is that the director field is singular (not uniquely defined or undefined) or discontinuous in the core of defects. This generally causes the gradients of the director field and therefore the (elastic) free energy of the system to diverge and become infinite in those regions. Nevertheless, the structure evolution of nematic phases is customarily studied using this approach, and to bypass the above mentioned problem, small volumes of system including the singularities are usually excised and approximate energetic contributions for the core of defects are provided.

However a better way to treat this problem is to describe the nematic ordering in terms of a tensor field $\mathbf{Q}(\mathbf{r})$, called tensor order parameter field. With the use of this second order tensor, defects do not have to be treated as singularities and reliable estimate of the free energy can be obtained. Nevertheless this is at the cost of an increase complexity of the governing equations. The tensor order parameter is symmetric traceless (*i.e.*, $Q_{ij} = Q_{ji}$ and $Q_{ii} = 0$) and can be represented, in terms of its eigensystem. A spectral decomposition gives the following linear combination:

$$Q_{ij} = \mu_n n_i n_j + \mu_m m_i m_j + \mu_l l_i l_j \tag{4.1}$$

The unit eigenvectors $(\mathbf{n}, \mathbf{m}, \mathrm{l})$ form a local orthogonal triad characterizing the orientation of the phase while the corresponding eigenvalues (μ_n, μ_m, μ_l) gives the strength of alignment along those directions $(\mu_n + \mu_m + \mu_l = 0)$. The largest eigenvalue in magnitude or absolute value, μ_n, gives the strength of ordering along the uniaxial

director $\mathbf{n}$ previously defined. The second μ_m and third μ_l eigenvalues correspond respectively to the biaxial directors $\mathbf{m}$ and $\mathbf{l}$ ($\mathbf{l} = \mathbf{n} \times \mathbf{m}$).

It is also often useful to represent the tensor order parameter $\mathbf{Q}$ in the following alternative, but equivalent, format:

$$Q_{ij} = S(n_i n_j - \frac{\delta_{ij}}{3}) + \frac{P}{3}(m_i m_j - l_i l_j) \tag{4.2}$$

In this expression, S and P are referred as uniaxial and biaxial scalar order parameters. They describe the amount of order (or strength of alignment) around the uniaxial director $\mathbf{n}$ and biaxial director $\mathbf{m}$ and are given by $S = 3/2(n_i Q_{ij} n_j)$ and $P = 3/2(m_i Q_{ij} m_j - l_i Q_{ij} l n_j)$ respectively. The Kronecker $\boldsymbol{\delta}$ stands for the unit tensor. The correspondence between the scalar order parameters and the eigenvalues is as follow: $\mu_n = 2/3S$, $\mu_m = -1/3(S - P)$ and $\mu_m = -1/3(S + P)$.

According to these definitions, the ordering states described by the tensor order parameter are: isotropic ($\mu_n = \mu_m = \mu_l = 0$; $\mathbf{Q} = 0$), uniaxial ($\mu_n > \mu_m = \mu_l$; $S \neq 0$, $P = 0$) and biaxial ($\mu_n \neq \mu_m \neq \mu_l$; $S \neq 0$, $P \neq 0$). Biaxial ordering is likely to arise around defect cores where S and P generally exhibit sharp changes. Since the eigenvalues μ_i ($i = 1, 2, 3$) of the tensor order parameter are restricted by: $-1/3 \leq \mu_i \leq 2/3$, the uniaxial and biaxial scalar order parameters must obey the following limits: $-1/2 \leq S \leq 1$ and $-3/2 \leq P \leq 3/2$ respectively.

Finally it is stressed that the employment of the tensor order parameter $\mathbf{Q}$, with its quadrupolar symmetry, is consistent with head-tail invariance of the nematic director, that is: $\mathbf{n} = -\mathbf{n}$.

4.3.3 Landau-de Gennes free energy

The dimensionless total free energy of a nematic liquid crystal system can be generally written as the sum of bulk and surface terms:

$$\bar{F} = \int_V \bar{f}_b d\bar{r}^3 + \int_S \bar{f}_s d\bar{r}^2 \tag{4.3}$$

In this work, only strong/fixed anchoring conditions are considered and therefore the surface term does not need to be considered. The bulk free energy density term, when expressed in terms of the tensor order parameter $\mathbf{Q}$, consist of an homogeneous $\bar{f}_h$ and a gradient $\bar{f}_g$ contribution ($\bar{f}_b = \bar{f}_h + \bar{f}_g$). The homogeneous contribution describes the short-range ordering effects/interactions related to the amplitude of the scalar order parameters (more generally, the amplitude of $\mathbf{Q}$). This expression permits to describe the first order isotropic-nematic phase transition but also the variation of ordering in the vicinity of defects. This contribution is often referred as the Landau-de Gennes free energy; in this work, Doi's formalism [34] is employed and, in dimensionless form, the expansion reads:

$$\bar{f}_h = \frac{1}{2}(1 - \frac{U}{3})Q_{ij}Q_{ji} - \frac{U}{3}Q_{ij}Q_{jk}Q_{ki} + \frac{U}{4}(Q_{ij}Q_{ji})^2 \tag{4.4}$$

In this expression U is a dimensionless phenomenological parameter called nematic potential which controls the magnitude of the equilibrium tensor order parameter; in other words, the values of the scalar order parameters. In general the nematic potential U can be assigned a dependence on either temperature or concentration depending on the nature of the nematic liquid crystal (*i.e.*, thermotropic or lyotropic). In our study U is taken to be proportional to concentration and according to Doi's

theory, $U = 3C/C^*$ where C and C^* are the number and critical number density of rod-like molecules, respectively [34]. Within this format, the first order phase isotropic-nematic phase transition occurs at nematic potential $U_{IN} = 2.7$. Also, in this model, the system is isotropic for $U < U_{IN}$ and nematic for $U > U_{IN}$. The limit of metastability for the isotropic and nematic phase are $U^* = 3$ and $U^{**} = 8/3$, respectively [34].

At equilibrium and away from distorted regions, the tensor order parameter $\mathbf{Q}$ given by Eq. 4.4 is uniaxial. The value of the scalar order parameter is given by the relation:

$$S_e = \frac{1}{4} + \frac{3}{4}\sqrt{1 - \frac{8}{3U}} \tag{4.5}$$

The gradient $\bar{f}_g$ contribution, represents the energy density variation due to long-range ordering effects/interactions which corresponds to the energy penalty associated with the elastic distortions of the phase or tensor order parameter $\mathbf{Q}$. This term is an analogue to the Frank elastic free energy and can be expressed in dimensionless form as:

$$\bar{f}_g = \frac{\bar{\xi}^2}{2}\bar{\nabla}_k Q_{ij}\bar{\nabla}_k Q_{ij} \tag{4.6}$$

In this equation $\bar{\xi}$ represents the reduced nematic coherence length which gives a characteristic scale for the variation of the tensor amplitude/scalar order parameters and the size of defect core (or the thickness of the nematic-isotropic interface).

4.3.4 Governing nemato-dynamic equation

The dynamic equation describing the relaxation of the tensor order parameter $\mathbf{Q}(\mathbf{r},t)$ towards an equilibrium value that minimizes the total free energy follows from variational principles and is given in dimensionless format by:

$$\frac{\partial Q_{\alpha\beta}}{\partial \bar{t}} = -\frac{\delta \bar{F}}{\delta Q_{\alpha\beta}} \tag{4.7}$$

The right-hand side of this expression corresponds to the functional derivative of the total free energy. From variational calculus it can be shown that:

$$\frac{\delta \bar{F}}{\delta Q_{\alpha\beta}} = \frac{\partial \bar{f}_b}{\partial Q_{\alpha\beta}} - \bar{\nabla}_\gamma \frac{\partial \bar{f}_b}{\partial \bar{\nabla}_\gamma Q_{\alpha\beta}} \tag{4.8}$$

Only the symmetric traceless part of this expression is retained in order to satisfy the constraints of the tensor order parameter.

4.3.5 Dimensionless quantities

In this work, dimensionless equations are used to reduced the number of parameters and facilitates analysis as well as comparisons with other studies. The relation between dimensional and dimensionless quantities is as follows: $\bar{\mathbf{r}} = \mathbf{r}/R$; $\bar{\nabla} = R\nabla$; $\bar{\xi} = \xi/R$ with $\xi = \sqrt{L/A}$; $\bar{f}_b = f_b/A$; $\bar{F} = \frac{F}{AR^3}$; $\bar{t} = \frac{A}{\gamma}t$. In these expressions, A is an energy density scale ($A = C^*kT$, where k and T are the Boltzmann constant and the temperature respectively), L a material-specific elastic constant, R the radius of the cavity and γ a kinetic constant associated with rotational viscosity.

4.3.6 Auxiliary conditions

The boundary conditions are as follows: at the wall of the cylindrical cavity (upper part of the rectangular domain), the tensor order parameter is assumed to be uniaxial and to describe a rigid radial anchoring condition so that $Q_{ij}(r = R) = S_e(e_i^r e_j^r - \frac{\delta_{ij}}{3})$, where e^r is the unit vector along the radial direction. A rotational symmetry boundary condition is considered on the z-axis (lower part of the rectangular domain). Finally, on the sides of the domain, Neumann conditions are enforced so as to emulate an infinitely long cavity; this condition does not introduce any spurious effects as tested by using different computational grids.

Initially, the systems contains a hedgehog pair whose cores are separated by a distance $\bar{D} = D/R = 2.4$. The hyperbolic and radial hedgehog are respectively located at $\bar{z} = -1.2$ and $\bar{z} = 1.2$. The corresponding initial tensor field $\mathbf{Q}(\mathbf{r}, t = 0)$ is obtained by taking a few time steps starting from a trial configuration satisfying all the boundary conditions. Other initial defect configurations do not change the essential features of the results.

The model used in this work contains two parameters: the nematic potential U and the reduced nematic coherence length $\bar{\xi}$. For all the simulation results presented, the nematic potential is set to $U = 6$ which corresponds to a deep nematic phase with an equilibrium scalar order parameter of $S_e = 0.809$. Other values of U in the stable nematic range do not change the underlying process under study. The value of the reduced coherence is varied in order to analyze its effect on the defect interactions.

4.3.7 Numerical procedure

The governing dynamic equation for the tensor order parameter $\mathbf{Q}(\mathbf{r}, t)$ is solved using the standard numerical method of lines (under the constraints imposed by the boundary conditions). The space discretization is achieved using the finite element method. The time integration of the resulting differential equations is obtained using an adaptive stable implicit scheme. The density of element is higher in the region describing the trajectories of the defects along the z-axis. The independence of solutions on mesh density was verified using standard procedures. The size of the triangular elements is always smaller than the reduced coherence length $\bar{\xi}$ (smallest length in the problem) to accurately capture the amplitude variations of the tensor order parameter. The computational domain is a rectangle of reduced width $\bar{Z} = 6$ and reduced height $\bar{R} = 1$.

4.4 Results and discussions

This section presents representative results of the interaction dynamics between a pair of point defects located along the axis of a nematic cylindrical cavity such as found in the spinning extrusion duct of spiders.

Figure 4–2 shows a typical evolution for the director $\mathbf{n}$ and scalar order parameter S fields during the annihilation of two point defects of opposite charge for a reduced coherence length $\bar{\xi} = 1/30$ and nematic potential $U = 6$. The pre-collision [Fig. 4–2(a),(b)], collision [Fig. 4–2(c),(d)] and post-collision [Fig. 4–2(e),(f)] stages are shown. In this figure, white and black respectively indicate order and disorder while the segments represent the local directors. The initial distance separating the

hyperbolic (left) and radial (right) hedgehogs, $\bar{D}$, is 1.2 times the diameter of the capillary tube [Fig. 4–2(a)]. At dimensionless time $\bar{t} = 39750$ [Fig. 4–2(b)], the two point defects move closer and the distortions of director field between them increase. However this evolution of the director field does not affect significantly the variations of the uniaxial scalar order parameter in the vicinity of the defects. This confirms that in the pre-collision regime the structural changes are mainly governed by director field distortions [25]. At dimensionless time $\bar{t} = 40585$ [Fig. 4–2(c)], the system is in the collision stage. The two point defects are still distinct but their cores now touch each other and the director distortions are accompanied by variations of the scalar order parameter. The drop in the scalar order parameter occurs principally between the defects but also extends in the $\bar{r}$-direction in contrast to the previous steps. At dimensionless time $\bar{t} = 40599$ [Fig. 4–2(d)], the scalar order parameter field indicates that the cores of the two defects are indistinguishable. The collision of the defects result into the creation of a single defect. At dimensionless time $\bar{t} = 40613$ [Fig. 4–2(e)], the system is in the post-collision regime and tries to get rid of the defect. The scalar order parameter field reveals that the size of the defect diminished while the director map remain almost unchanged with respect to the previous time frame. This indicates that in this regime the structural changes are mainly governed by the variation of the scalar order parameter rather by the director distortions. This result is in agreement with a previous study that has used a Brownian molecular dynamics approach of a similar problem [25]. Finally, in the late stage of the post-collision regime, at dimensionless time $\bar{t} = 40914$ [Fig. 4–2(e)], the

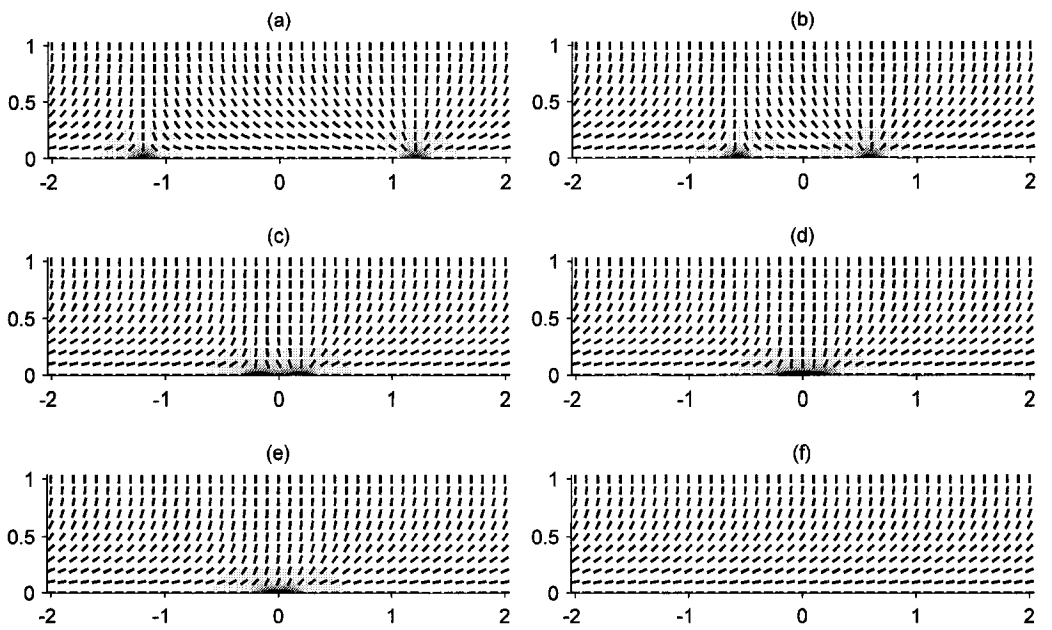

Figure 4–2: Evolution of the orientation (**n**)and alignment (S) fields during the pre-collision (a)-(b), collision (c)-(d) and post-collision (e)-(f) regimes of two nematic point defects along the axis of cylindrical capillary. The frame (a), (b), (c) and (d) correspond respectively to the dimensionless time $\bar{t} = 0, 39750, 40585, 40599, 40613, 40914$. The small segments represent the directors and thus the local preferred orientation of the rod-like molecules. The grayscale corresponds to S. The white regions are ordered while black ones, around defects, are disordered. $U = 6$, $\bar{\xi} = 1/30$.

system completes its relaxation and the defect disappear. The defect-free structure thus obtained corresponds to the classical escaped radial solution.

Figure 4–3 illustrates the evolution of the scalar order parameter S, along the $\bar{z}$-axis, during the annihilation of the two point defects for the same choice of parameters as Fig 4–2. Also, as in the Fig. 4–2, the pre-collision [Fig. 4–3(a and b)],

collision [Fig. 4–3(c and d)] and post-collision [Fig. 4–3(e and f)] stages are represented. In the pre-collision regime the two mutually approaching defects are single solitons. Clearly, in this stage, the two defects approach one another at the same speed [See also Fig. 4–4 and Fig. 4–5] without any amplitude changes in structure as indicated by the lateral translation of the single solitons. The scalar order parameter quickly reach an equilibrium value on each side of the two defects. In the collision stage, the two defects first collide (c), keeping their cores distinct, subsequently they strongly overlap (d) and become indistinguishable thus creating a single defect with an elongated core (In contrast to the circular nature of the individual defect cores). The profile of the scalar order parameter in the core of this resulting defect is flat (d). This is because the system lowers the ordering, in the inter-defect region, to the level of the surrounding defect cores. In the post-collision stage the profile of the scalar order parameter show an opposite behavior as the system relaxes (e) and the size of the defect gradually reduces before finally vanishing (f). During this step, ordering in the defect core progressively increases toward the equilibrium value of the bulk surroundings.

Figure 4–4 shows the displacement of the two point defects as a function of time during the annihilation process. Two cases are represented: (a) $U = 6$, $\bar{\xi} = 1/20$; (b) $U = 6$, $\bar{\xi} = 1/30$. The position of the point defects is determined by finding the minima of the corresponding uniaxial scalar order parameter profiles. The trajectories show that the displacement of the two defects are symmetric and that their speed increase dramatically on approaching each other. On comparing the two profiles one can easily concludes that the time required for the defects to

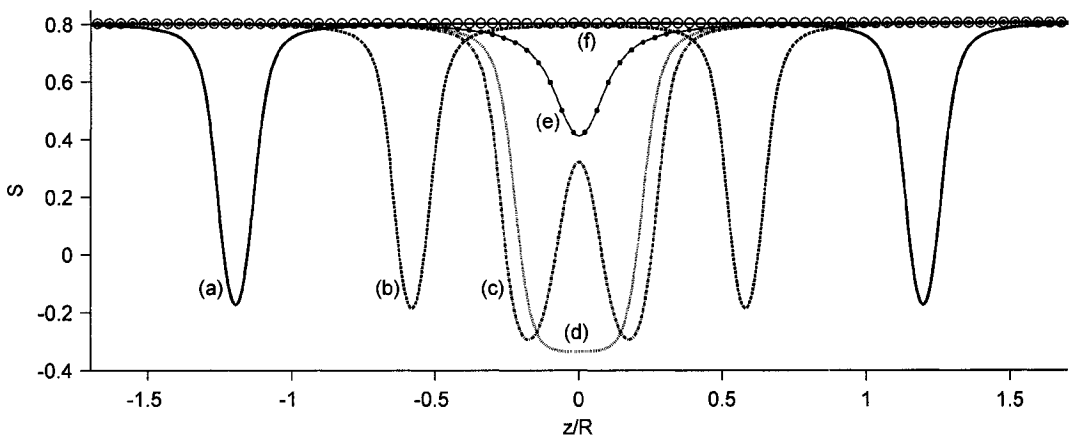

Figure 4–3: Evolution of the scalar order parameter S profile, along the $\bar{z}$-axis, during the pre-collision(a)-(b), collision (c)-(d) and post-collision (e)-(f) regimes. The dimensionless sampling times (a)-(f) are $\bar{t} = 0, 39750, 40585, 40599, 40620, 40920.U = 6$, $\bar{\xi} = 1/30$.

collide and annihilate reduces as $\bar{\xi}$ increases (*i.e.*, the diameter of the capillary tube decreases). To complement this result, Fig. 4–5 shows the reduced speed of the point defects as a function of the inter-defect distance $\bar{D}$ corresponding to Fig. 4–4. The trends show clearly that the speed of the point defects increases exponentially as the hedgehogs approach each other and collide to form a single defect. Also, in accordance to Fig. 4–4, the defects travel faster as the reduced coherence length $\bar{\xi}$ increases.

The force exerted on the nematic point defects and which set them into motion is usually called elastic because it is mediated by the surroundings director field distortions. One simple way of estimating this interaction force is by differentiating the bulk free energy corresponding to the minimized order parameter field with respect to the distance separating the two defects. In this work, the tensor order

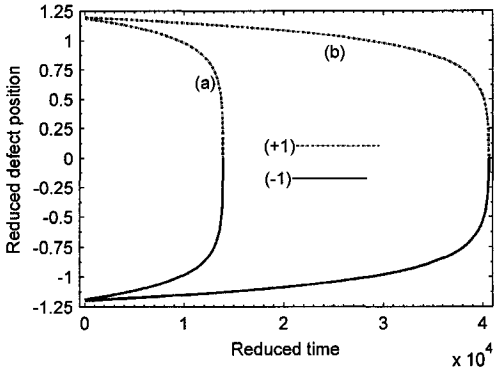

Figure 4–4: Reduced position of the point defects along the $\bar{z}$-axis as a function of the reduced time during the annihilation process. (a) $U = 6$, $\bar{\xi} = 1/20$; (b) $U = 6$, $\bar{\xi} = 1/30$.

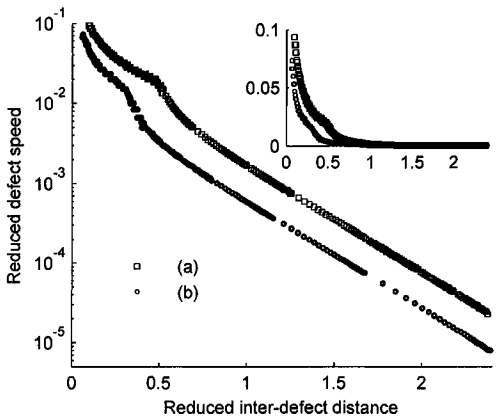

Figure 4–5: Reduced speed of the point defects as a function of their separating distance $\bar{D}$ during the annihilation process expressed in semi-log and linear scales. The speed of the point defects in the pre-collision and early collision regimes follows an exponential law. The trends for the (a) and (b) cases can be fitted with $0.03800\exp(-3.11\bar{D})$ and $0.01391\exp(-3.11\bar{D})$, respectively. (a) $U = 6$, $\bar{\xi} = 1/20$; (b) $U = 6$, $\bar{\xi} = 1/30$.

parameter formalism is employed and the reduced total bulk free energy can be evaluated by computing the following integral:

$$\bar{F} = 2\pi \int_{\bar{r}=0}^{\bar{r}=1} \int_{\bar{z}=-3}^{\bar{z}=3} \bar{f}_b \bar{r} d\bar{r} d\bar{z} \tag{4.9}$$

The corresponding reduced force of interaction between the point defect pair $\bar{f}_i$ is computed according to:

$$\bar{f}_i = -\frac{\partial \bar{F}}{\partial \bar{D}} \tag{4.10}$$

Figures 4–6 and 4–7 show the profiles of the reduced total free energy $\bar{F}$ and corresponding reduced interaction force $\bar{f}_i$ acting on the defects as a function of the reduced inter-defect distance for reduced coherence lengths $\bar{\xi}$ of 1/30 and 1/20 respectively. The profiles of the total reduced free energy and corresponding force of interaction exhibit very similar behaviors. The only noticeable difference between these profiles is the location of the inflexion points in the free energy curves. It is found that the abscissa of the inflection point increases with $\bar{\xi}$. This lateral shift in the inflexion point location is indeed related to the size of the defect cores which reduces with $\bar{\xi}$. Defects with smaller cores collide later in the annihilation process.

As discussed in Ref. [31,32], the profile of the interaction force between the point defects is still a matter of dispute. Different experimental and theoretical approaches have been taken to study the problem. Some studies [30–32] tend to indicate that the interaction force is attractive at short separating distance and repulsive at large separating distance while other works (including ours) favor the idea of a purely

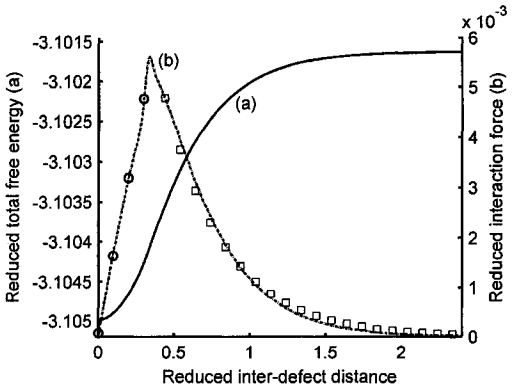

Figure 4–6: Evolution of reduced total free energy $\bar{F}$ (a) and corresponding reduced interaction force $\bar{f}_i$ (b) as a function of the reduced inter-defect distance for $U = 6$, $\bar{\xi} = 1/30$. The circles and squares denote respectively the linear $(0.01564\bar{D}+7.521e-5)$ and exponential $(0.01386\exp(-2.42\bar{D}))$ fits.

attractive force [26–29]. The discrepancies found in the theoretical works is believed to be due to boundary condition differences [32].

The difference between our computational approach and the previous ones is essentially the employment of a tensor order parameter which allows a continuous description of defect dynamics. This is particularly important in the collision stage governed by nematic ordering rather than director distortions as shown in Fig. 4–2 and Fig. 4–3. The force of interaction between the point defects is found to be strictly attractive. As previously demonstrated analytically in Ref. [26], the interaction force decay exponentially as the distance between the defect increases and becomes essentially negligible as defects separate by more than a diameter [28, 29]. However, in contrast to Refs [28, 29] the force is found to steeply reduce in a linear manner in the late stage of the collision rather than reaching a plateau. This behavior is attributed to the variation of the scalar order parameters. It is noticed, to the degree

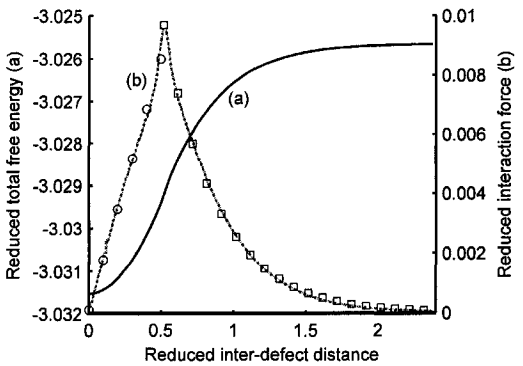

Figure 4–7: Evolution of reduced total free energy $\bar{F}$ (a) and corresponding reduced interaction force $\bar{f}_i$ (b) as a function of the reduced inter-defect distance for $U = 6$, $\bar{\xi} = 1/20$. The circles and squares denote respectively the linear $(0.01695\bar{D}+8.836e-5)$ and exponential $(0.03898\exp(-2.684\bar{D}))$ fits.

of resolution of the computational scheme and mesh density used in this work, that as the defect separating distance shrinks to zero the force remains finite although small. Figure 4–8 shows the time frame corresponding to the structural transition from the ERPD to the ER structures in the time evolution of the reduced total free energy for $U = 6$ and $\bar{\xi} = 30$. Three zones are identified: zone (a) corresponds to the pre-collision and collision stages previous identified in which to defect cores can be identified; zone (b) corresponds to the post-collision regime in which the system relaxes and defect gradually disappear; in zone (c) the system is the stable ER configuration and no trace of the ERPD structure can be found. It can be seen once again from this graph that the scalar order parameter relaxation plays a significant role in the defect pair annihilation and structural transition to the ER structure.

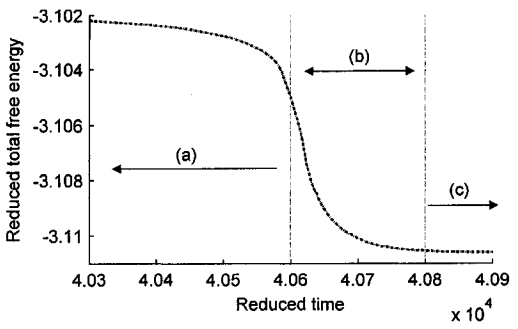

Figure 4–8: Time frame of the reduced total free energy during which the nematic system undergoes its structural transition from the ERPD to the ER configuration through the annihilation of two point defects of opposite topological charges. $U = 6$, $\bar{\xi} = 30$. In zone (a), the system presents two defects with distinct cores; in zone (b), the two defects have collapsed into a single defect which gradually disappear; in zone (c) the system is in defect-free ER configuration.

4.5 Conclusions

Motivated by the experimental observation of ERPD and ER structures in the extrusion duct of spiders spinning apparatus we have investigated numerically the dynamic interaction between two nematic point defects of opposite topological charge confined in cylindrical cavity. In contrast to previous analytical and numerical studies we employed the tensor order parameter formalism to describe the orientational order of the nematic phase, which allows for an unambiguous description of defects and reliable estimation of energies. Three distinct regimes leading to the annihilation of the antagonist point defect pair were described. The importance of the scalar order parameter S in the collision and post-collision regimes was demonstrated. Defect trajectories and corresponding speeds were reported for two different radius of the cylindrical cavity. It was found that the point defect travel faster in smaller cavities. The trends of defect trajectories agrees very well the one found in theoretical [26]

and experimental [27] studies. The absence of asymmetry in the defect trajectories as reported in Ref. [35] is attributed to the absence of backflow effects as well as by the isotropy of the elastic constant. Those effects will be investigated in future work and will be reported. The reasons of the point defect annihilation were also investigated. In particular, the dependence of the total free energy and corresponding interaction force on the inter-defect distance was analyzed for two different values of the cylindrical capillary radius. It was shown that the interaction force between the defect, which set them into motion, is decreasing exponentially at large defect separating distance. As predicted theoretically in Ref. [26] and shown experimentally if the point defects are separated by a distance greater than a diameter, the interaction force is shielded and the defects pinned. In contrast to previous studies having reported explicitly the force of interaction, we have found that at short separating distance, the interaction force was decreasing very steeply in a linear way. We show that this distinctive behavior is due to the significant variation of the scalar order parameter in the late stage of the collision regime. During the whole process the interaction force was found to be strictly attractive. Finally we would like to emphasize that despite that the context of our study is the biospinning process of spider silk, the obtained results should be useful to the field of defect physics.

REFERENCES

[1] J.M. Gosline, M.E. DeMont, and M.W. Denny. The structure and properties of spider silk. *Endeavour*, 10(1):37–43, 1986.

[2] F. Vollrath and D.P. Knight. Liquid crystalline spinning of spider silk. *Nature*, 410:541–548, 2001.

[3] F.K. Ko and J. Jovicic. Modeling of mechanical properties and structural design of spider web. *Biomacromolecules*, 5:780–785, 2004.

[4] S.A. Wainwright, W.D Biggs, J.D. Currey, and J.M. Gosline. *Mechanical Design in Organims.* Princeton University Press, Princeton, NJ, 1982.

[5] R.F. Foelix. *Biology of spiders.* Oxford University Press, New York, 1996.

[6] C.L. Craig. *Spiderwebs and silk.* Oxford University Press, New York, 2003.

[7] E. Atkins. Silk's secrets. *Nature*, 424:1010, 2003.

[8] H.-J. Jin and D.L. Kaplan. Mechanism of silk processing in insects and spiders. *Nature*, 424:1057–1061, 2003.

[9] J. Turner and C. Karatzas. *Natural fibers, plastics and composites*, chapter 1, Advanced spider silk fibers by biomimicry, pages 11–23. Kluwer Academic Publishers, Dordrecht, 2004.

[10] T. Scheibel. Spider silks: recombinant synthesis, assembly, spinning, and engineering of synthetic proteins. *Microb. Cell Fact.*, 3:14, 2004.

[11] T. Scheibel. Protein fibers as performance proteins: new technologies and applications. *Curr. Opin. Biotech.*, 16:427–433, 2005.

[12] K. Kerkam, C. Viney, D. Kaplan, and S. Lombardi. Liquid crystallinity of natural silk secretions. *Nature*, 349:596–598, 1991.

[13] C. Viney, A.E. Huber, D.L. Dunaway, K. Kerkam, and S.T. Case. *Silk polymers: materials science and biotechnology*, chapter 11, Optical characterization of silk

secretions and fibers, pages 120–136. American Chemical Society, Washington, DC, 1993.

[14] P.G. de Gennes and J. Prost. *The physics of liquid crystals.* Oxford University Press, New York, 1995.

[15] P.J. Collings. *Liquid crystals: nature's delicate phase of matter.* Princeton University Press, Princeton, NJ, 2001.

[16] D.P. Knight and F. Vollrath. Liquid crystals and flow elongation in a spider's silk production line. *Proc. R. Soc. Lond. B*, 266:519–523, 1999.

[17] F. Vollrath. Strength and structure of spiders silks. *Rev. Mol. Biotech.*, 74:67–83, 2000.

[18] D.P. Knight and F. Vollrath. Comparison of the spinning of selachian egg case ply sheets and orb web spider dragline filaments. *Biomacromolecules*, 2(2):323–334, 2001.

[19] D.P. Knight and F. Vollrath. Biological liquid crystal elastomers. *Proc. R. Soc. Lond. B*, 357:155–163, 2002.

[20] J.E. Lydon. Silk: the original liquid crystalline polymer. *Liq. Cryst. Today*, 13(3):1–13, 2004.

[21] P. Biscari, G.G. Peroli, and E.G. Virga. A statistical study for evolving arrays of nematic point defects. *Liq. Cryst.*, 26(12):1825–1832, 1999.

[22] C. Williams, .P Pieranski, and P. E. Cladis. Nonsingular s=+1 screw disclination lines in nematics. *Phys. Rev. Lett.*, 29(2):90, 1972.

[23] C.E. Williams, P.E. Cladis, and M. Kleman. Screw disclinations in nematic samples with cylindrical symmetry. *Mol. Cryst. Liq. Cryst.*, 21(3-4):355–373, 1973.

[24] D. Melzer and F.R.N. Nabarro. Cols and noeuds in a nematic liquid-crystal with a homeotropic cylindrical boundary. *Philos. Mag.*, 35(4):907–915, 1977.

[25] Z. Bradac, S. Kralj, M. Svetec, and S. Zumer. Annihilation of nematic point defects: Postcollision scenarios. *Phys. Rev. E*, 67(5):050702, 2003.

[26] G.G. Peroli and E.G. Virga. Annihilation of point defects in nematic liquid crystals. *Phys. Rev. E*, 54(5):5235–5241, 1996.

[27] G.G. Peroli, G. Hillig, A. Saupe, and E.G. Virga. Orientational capillary pressure on a nematic point defect. *Phys. Rev. E*, 58(3):3259–3263, 1998.

[28] A. N. Semenov. Interaction of point defects in a nematic liquid. *Europhys. Lett.*, 46(5):631–636, 1999.

[29] E.C. Gartland, A.M. Sonnet, and E.G. Virga. Elastic forces on nematic point defects. *Continuum Mech. Therm.*, 14(3):307–319, 2002.

[30] I. Vilfan, M. Vilfan, and S. Zumer. Defect structures of nematic liquid-crystals in cylindrical cavities. *Phys. Rev. A*, 43(12):6875–6880, 1991.

[31] J. Ignes-Mullol, J. Baudry, and P. Oswald. Formation and distribution of point defects on a disclination line near a free nematic interface. *Phys. Rev. E*, 63:031701, 2001.

[32] R. Holyst and P. Oswald. Annihilation of point defects on a line. *Phys. Rev. E*, 65:041711, 2002.

[33] Z. Bradac, S. Kralj, and S. Zumer. Molecular dynamics study of nematic structures confined to a cylindrical cavity. *Phys. Rev. E*, 58(6):7447–7454, 1998.

[34] M. Doi. *The Theory of Polymer Dynamics.* Oxford University Press, New York, 1998.

[35] P.E. Cladis and H.R. Brand. Hedgehog-antihedgehog pair annihilation to a static soliton. *Physica A*, 326(3-4):322–332, 2003.

CHAPTER 5
Structure evolution of spider silk liquid crystalline precursor material

5.1 Summary

Spiders produce silk fibers with remarkable mechanical properties using an ultra-optimized spinning process. The fluid precursor material used to draw the silk threads is a lyotropic nematic liquid crystal. The mechanical properties of the silk fibers as well as their processability are strongly affected by the complex structural transitions undergone by the nematic liquid crystal precursor along the spinning line. Our work focuses on the particular structure adopted by the nematic precursor in the extrusion duct of the spinning apparatus. This structure is characterized by a succession of well defined point defects located on the axis of the cavity and interacting on each other through elastic mediated forces. The phenomenon described is both important in understanding the process-induced structuring of spider silk fibers and to defect physics.

5.2 Introduction

Spiders' ultra-optimized and ecological spinning process produces a fiber with mechanical properties comparable or even superior to the best man-made super-fibers, which use corrosive solvents and cause significant environmental degradation [1, 2]. Hence, there is a great deal of interest in understanding the intricacy of their design and processing routes. Many environment friendly exciting applications are

envisaged upon the successful replication of spiders' fibers and complex spinning line [3–5].

Spider silk fibers are known to be spun from a lyotropic nematic liquid crystal emerging from a highly concentrated water-based solution of rod-like molecules or aggregates [6–8]. A quintessential property of this silk precursor is its capacity to maintain some degrees of orientational order while still flowing as a liquid. This orientational order is characterized by the tendency that have neighboring rod-like units to align their long axis in parallel along a common direction [9, 10]. This preferred molecular orientation usually varies from subregion to subregion in the mesophase (*i.e.*, intermediate phase) due to elastic effects coupled with geometrical and interfacial constraints [9]. The evolution of orientational order or molecular orientation along the spinning pathway is crucial as it affects the processability of the silk precursor mesophase and determines the microstructural details of the solidified fiber and therefore its remarkable physical properties [6–8].

Spiders' spinning line basically consist in a tail where the silk precursor material is synthesized, a central bag where it is stocked in a very concentrated solution, and an extrusion duct from which the silk fiber is drawn [8, 11]. Observations made by polarized light microscopy in the extrusion duct have revealed the presence of a complex orientation structure known as escaped radial with point defects (ERPD) [8, 12–14]. The point defects, referred as hedgehogs or monopole, are located where the direction of bending distortions changes. At those particular locations, orientational order *melts*. Two types of point defects are alternatively found in the cylindrical cavity of the extrusion duct: the radial and the hyperbolic hedgehogs. Figure 5–1

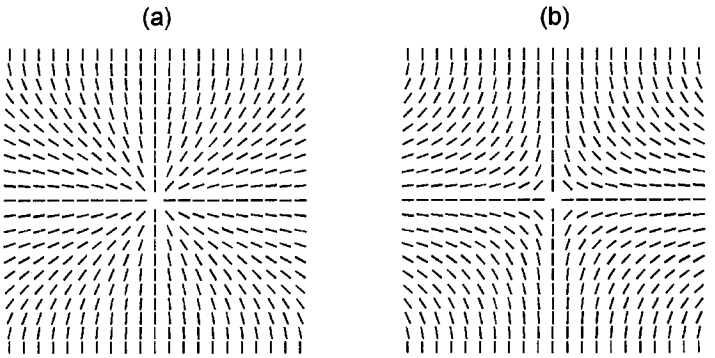

Figure 5–1: Structure of the radial (a) and hyperbolic (b) point defects found along the spinning duct of spiders in terms of the director field $\mathbf{n}(\mathbf{r})$.

shows the characteristic structures of the radial and hyperbolic hedgehogs in term of a director field $\mathbf{n}(\mathbf{r})$ giving the local average preferred orientation of the molecules. The unit directors are drawn arrowhead-free as there is no physical difference between the vector field $\mathbf{n}(\mathbf{r})$ and $-\mathbf{n}(\mathbf{r})$ [9, 10].

Whether this complex molecular structure is an accident of Nature or a necessary ingredient of the spider biospinning process is unknown at present. Nonetheless, one my hypothesized that this configuration with its orientational defects may play an important role in the control of material crystallization along with water pumping, ions exchanges and pH reduction phenomena [8]. Indeed, a premature crystallization of the silk may indeed cause the permanent blockage of the extrusion system and ultimately lead to the death of the animal [8, 15].

Nematic point defects confined in cylindrical geometries have been first experimentally observed and explained in the early seventies [16–19]. They are typically observed when a nematic mesophase is confined in cylindrical capillary with lateral

walls enforcing strong radial anchoring (*i.e.* molecules are forced to orient radially at the surface). Point defects with opposite topological charges are known to annihilate by pairs. This has been experimentally observed [16–21] and theoretically described [20, 22–26]. Results have shown that when two defects are separated by less than a tube diameter they usually attract until they eventually annihilate. As the two defects come closer their speed increases exponentially. At large separating distance the situation is far less clear as some studies support the hypothesis of a total screening of the attraction force [23–25] while others support a repulsion force [22, 27]. Recent experiments have also shown a possible speed anisotropy between the point defects [28] but the role played by elastic anisotropy and back-flow in this phenomenon has not been clearly established yet.

Obviously these phenomena become even further involving when considering not two point defects but rather a whole a array of them. Some studies have in fact *touched* this problem in a statistical manner but no experimental data have yet corroborated them [29]. During their evolution arrays often splits into sub-arrays of few interacting defects with alternating signs. This work aims at describing what can possibly happen inside those sub-arrays. These results should be useful in improving the understanding of arrays of nematic point defects and therefore of their behavior along the spinning duct of spiders, and hence contributing to the on-going efforts to develop systematic technology transfer from Nature to fiber engineering.

5.3 Modeling

In this section we briefly present the necessary theoretical background to study the dynamics of nematic point defects that is essential to silk bio-spinning.

The continuum dynamic equation describing the structure evolution of a nematic liquid crystal is typically derived from the minimization of a free energy functional depending on some orientational order parameter that characterizes molecular order and macroscopic texture [9]. In the simplest continuum approach, the orientational order of parameter is a unit vector $\mathbf{n}(\mathbf{r})$, called director, giving the average preferred orientation of the molecules at a point $\mathbf{r}$. The energy cost associated with the distortions of the director field is then given by the Frank distortion energy [9]:

$$f_b = \frac{K_1}{2}(\nabla \cdot \mathbf{n})^2 + \frac{K_2}{2}(\mathbf{n} \cdot \nabla \times \mathbf{n})^2 + \frac{K_3}{2}(\mathbf{n} \times \nabla \times \mathbf{n})^2, \tag{5.1}$$

where K_1, K_2, K_3 are elastic constants for the three modes of orientational distortions occurring in nematic: splay, twist and bend. It is useful and moreover appropriate to adopt the so-called one constant approximation: $K = K_1 = K_2 = K_3$. Within this approximation, no speed anisotropy can be attributed to elastic effects. The Frank free energy simplifies to:

$$f_b = \frac{K}{2}\nabla\mathbf{n} : (\nabla\mathbf{n})^T. \tag{5.2}$$

This vectorial approach is generally well suited to study small and continuous deformations of the nematic liquid crystal. However, this approach generally fails in the vicinity of defects where the director field may be discontinuous causing, in turn, the distortion free energy to become infinite. However, this problem can be overcome

in a rather straightforward manner by allowing the director to deviate from its unit length constraint and act as an additional order parameter measuring the degree of molecular alignment along itself. In this work we employed a regularized Frank elastic free energy of the form [30, 31]:

$$f_b = K\left[\frac{1}{2}\nabla\mathbf{n} : (\nabla\mathbf{n})^T + \frac{(|\mathbf{n}|^2-1)^2}{4\delta^2}\right], \tag{5.3}$$

where δ is a penalty parameter related to the size of the defect core. The second term on the right-hand side of Eq. 4.3 is the penalty function that allows the director to deviate from unity in orientational defects and the distortion energy to be bounded.

The time dependent equation for the rotation of the director is determined by the balance between a viscous and an elastic torque. The latter, which is usually refereed as molecular field, is given by the variational derivative of the Frank elastic free energy. The transient director equation is then:

$$\gamma\frac{\partial\mathbf{n}}{\partial t} = K\left[\nabla\cdot\nabla\mathbf{n} - \frac{(\mathbf{n}^2-1)\mathbf{n}}{\delta^2}\right], \tag{5.4}$$

where γ is a constant associated with the rotational viscosity of the director.

In order to reduce the number of parameters and facilitate the analysis of the results we non-dimensionalize the governing equation by introducing the characteristic time and length scales of the problem. Lengths are measure in terms of the capillary radius and therefore: $\bar{\mathbf{r}} = \mathbf{r}/R$. The time scale is determined by the typical relaxation time of the director field and is given by: $\bar{\mathbf{t}} = \mathbf{t}/\tau$ with $\tau = \frac{\gamma R^2}{K}$.

Given that the solutions to our problem have an obvious rotational symmetry around the axis of the cylindrical cavity we consider a two dimensional computational space representing half of a longitudinal cross section and we accordingly employ cylindrical coordinates (r, z). The width L and height R of the computational domain are set to 5 and 1, respectively. Finally, the boundary conditions on the outer wall and end caps are respectively strong radial anchoring and no flux.

5.4 Results

This section gives some representative results on the collective behavior of subarrays of nematic point defects lying on the axis of a cylindrical capillary and interacting between each other. We consider scenarios involving three and then four nematic point defects.

5.4.1 Interactions between three point defects

In this case we examine the influence of a point defect on the interaction between a neighboring pair. Note that the global charge of the system does not alter the results presented. As we mentioned earlier, when two defects of opposite charges are sufficiently close one another (*i.e.*, when their separating distance is smaller or equal to the tube diameter) they usually attract and finally annihilate living no trace of their previous existence. Furthermore when no back-flow or anisotropic elastic effects are considered, the two defects travel at the same speed and therefore meet at the midpoint between their initial positions. This behavior can be however significantly affected by the presence of an additional defect interacting with the pair.

Figure 5–2 shows the trajectories of three nematic point defects as a function of time for three different scenarios. In all three cases, two defects, forming a pair, were initially held at the same separating distance $d_i = 0.95$ while a third *perturbing* defect was placed at different distances $d_p = 1.05, 1.55, 2.05$ away from that pair. It can be seen from fig. 5–2 that as d_p increases, the effect of the *perturbing* defect becomes weaker. For the case $d_p = 2.05$ (the separation tends to the screening length), the pair is annihilating practically at midpoint and roughly unaware of its presence. The reverse is also obviously true for the *perturbing* defect which is just weakly initially attracted by the pair. When $d_p = 1.05$ (the distances between the three defects are comparable), the trajectories become distorted as the system tries to globally reduce the distance separating the defects, including d_p. One can see that the pair does not annihilate at midpoint anymore indicating speed anisotropy between the two defects. Furthermore, the time required for the pair annihilation is found to increase as d_p decreases. Figure 5–3 illustrates the dynamic structural changes occurring in the case $d_p = 1.05$. In this figure, the small segments give the director field while the gray scale provides and indication of its length thereby providing an alignment scalar order parameter.

5.4.2 Interactions between four point defects

We now turn to cases where all defects can potentially annihilate by pair and disappear from the system. The system has now two pairs and therefore an additional important length to take into account. We denote by d_j this distance separating the second pair of defects. As for the previous cases of three defects, one pair is held at

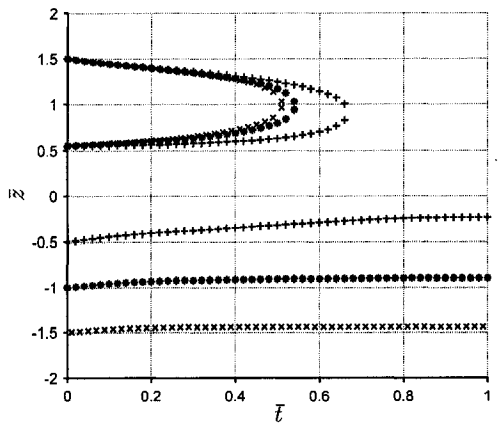

Figure 5–2: Position of the point defects along the cavity axis as a function of time for three different cases ($d_p = 1.05, 1.55, 2.05$)

constant initial separation. One of the defects of the second pair (the exterior one) is also held at the same initial position while the remaining defect (inner one) is moved at different initial positions thus varying the lengths d_j and d_p at the same time.

Figure 5–4 shows the trajectories of the four defects as a function of time for different initial positions of one defect. It can be seen that when d_p is large and approaching the screening distance, the two pairs annihilate unaware of each other. The pair whose initial interdefect separating distance is the smallest annihilates the fastest. In the second case $d_i \approx d_j \approx d_p$ and the two pairs annihilate in the same time frame. The trajectories of the defects in each pair are asymmetric as the two exterior defects are traveling faster than their inner counterpart. It is also important to note that the two inner defects do not collapse together despite being separated by the same distance with respect to the exterior defects. This provides evidence that each defect is affected by all the remaining ones and the attraction felt is proportional to

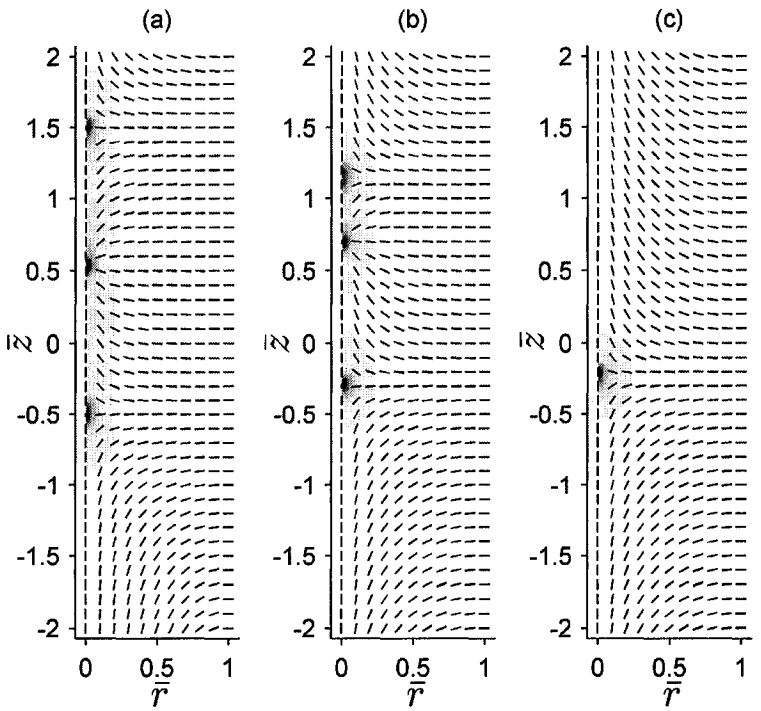

Figure 5–3: Evolution of structure in the cylindrical capillary as the point defects move along the axis. Segments indicate the orientation of directors while the gray scalar gives the degree of alignment along the directors. Black=no alignment=defect core, white=alignment. $\bar{t} = 0.01(a), 0.6(b)$ and $1(c)$.

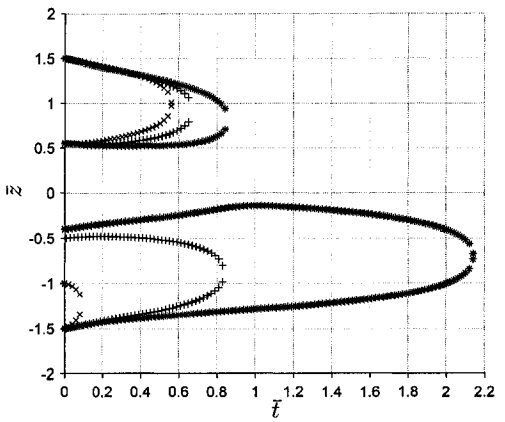

Figure 5–4: Position of the point defects along the cavity axis as a function of time for three different cases.

the separating distances. In the third and last case, $d_p < d_j$ and the inner defect is more attracted by the other inner defect rather by the closet exterior defect so that three defects tend to go in the same direction. Unfortunately for the *rebelling* defect, it is still slowed down enough by the attraction of the closet exterior defect so that it cannot reach the other pair on time and it is forced to change direction once the first pair has collapsed. This change of direction considerably lengthens the annihilation process of the second pair. As observed from the case of three defects the annihilation time scale increases as d_p decreases. Figure 5–5 illustrates the dynamic structural changes occurring in the case $d_i \approx d_j \approx d_p$.

5.5 Conclusions

We have presented a simple model to study the interactions between nematic point defects lying on the axis of a cylindrical capillary. This work was motivated

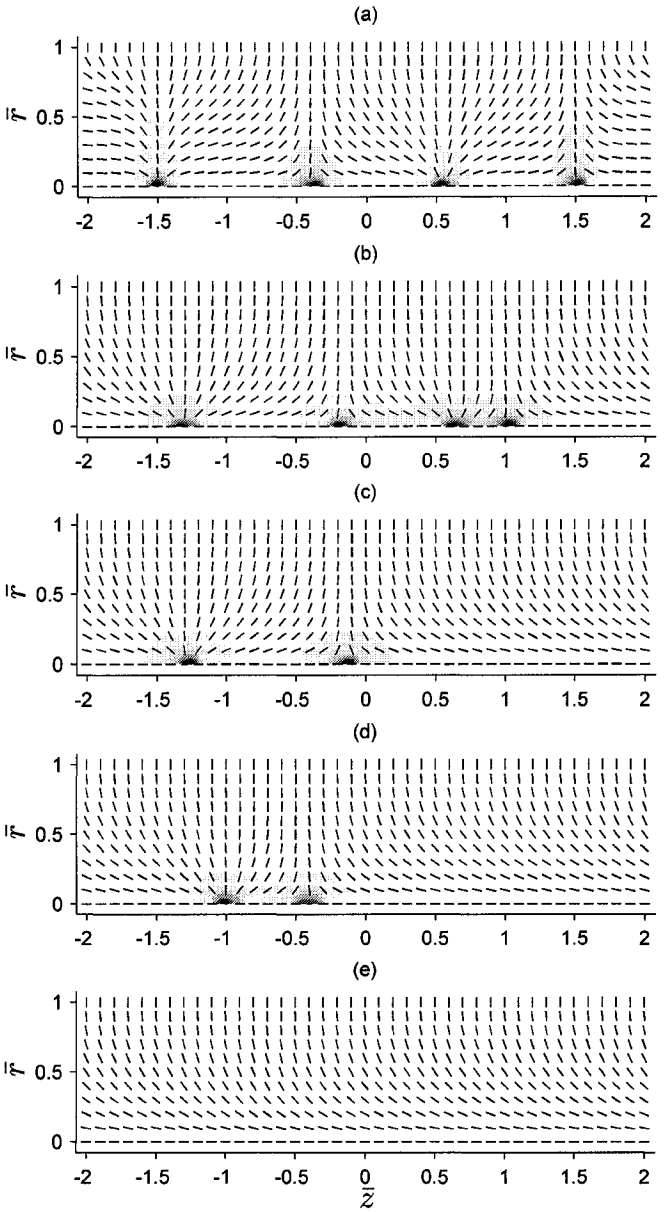

Figure 5–5: Evolution of structure in the cylindrical capillary as the point defects move along the axis. Black=no alignment=defect core, white=alignment. $\bar{t} = 0.01(a), 0.81(b), 0.99(c), 2(d)$ and $2.2(e)$.

by the reported experimental observation of those types of liquid crystal defects and related structures along the spinning extrusion duct of spiders. The cases of sub-arrays of three and four mutually interacting defects were presented. Despite the absence of back-flow and elastic anisotropy effects, strong anisotropy were put in evidence due to the sole effect of collective interactions. As for the much studied case of two interacting point defects, the screening distance after which the defects were unaware of each other and pinned was found to be around one diameter. A phenomenon of direction change that cannot be observed when considering only two defects was also featured. The different simulations have shown that defects are always attracted by their closet complementary neighbor but still affected by all the other defects below the screening distance. The results presented here should be useful in both improving the understanding of point defects in the context of the process-induced structuring of spider silk and to the more universal physics of defects.

REFERENCES

[1] J.M. Gosline, M.E. DeMont, and M.W. Denny. The structure and properties of spider silk. *Endeavour*, 10(1):37–43, 1986.

[2] F.K. Ko and J. Jovicic. Modeling of mechanical properties and structural design of spider web. *Biomacromolecules*, 5:780–785, 2004.

[3] E. Atkins. Silk's secrets. *Nature*, 424:1010, 2003.

[4] H.-J. Jin and D.L. Kaplan. Mechanism of silk processing in insects and spiders. *Nature*, 424:1057–1061, 2003.

[5] J. Turner and C. Karatzas. *Natural fibers, plastics and composites*, chapter 1, Advanced spider silk fibers by biomimicry, pages 11–23. Kluwer Academic Publishers, Dordrecht, 2004.

[6] K. Kerkam, C. Viney, D. Kaplan, and S. Lombardi. Liquid crystallinity of natural silk secretions. *Nature*, 349:596–598, 1991.

[7] C. Viney, A.E. Huber, D.L. Dunaway, K. Kerkam, and S.T. Case. *Silk polymers: materials science and biotechnology*, chapter 11, Optical characterization of silk secretions and fibers, pages 120–136. American Chemical Society, Washington, DC, 1993.

[8] F. Vollrath and D.P. Knight. Liquid crystalline spinning of spider silk. *Nature*, 410:541–548, 2001.

[9] P.G. de Gennes and J. Prost. *The physics of liquid crystals.* Oxford University Press, New York, 1995.

[10] P.J. Collings. *Liquid crystals: nature's delicate phase of matter.* Princeton University Press, Princeton, NJ, 2001.

[11] R.F. Foelix. *Biology of spiders.* Oxford University Press, New York, 1996.

[12] D.P. Knight and F. Vollrath. Liquid crystals and flow elongation in a spider's silk production line. *Proc. R. Soc. Lond. B*, 266:519–523, 1999.

[13] F. Vollrath. Strength and structure of spiders silks. *Rev. Mol. Biotech.*, 74:67–83, 2000.

[14] J.E. Lydon. Silk: the original liquid crystalline polymer. *Liq. Cryst. Today*, 13(3):1–13, 2004.

[15] S.A. Wainwright, W.D Biggs, J.D. Currey, and J.M. Gosline. *Mechanical Design in Organims.* Princeton University Press, Princeton, NJ, 1982.

[16] C. Williams, .P Pieranski, and P. E. Cladis. Nonsingular s=+1 screw disclination lines in nematics. *Phys. Rev. Lett.*, 29(2):90, 1972.

[17] P.E. Cladis and M. Kleman. Non-singular disclinations of strength s=+1 in nematics. *J. Phys.*, 33(5-6):591, 1972.

[18] C.E. Williams, P.E. Cladis, and M. Kleman. Screw disclinations in nematic samples with cylindrical symmetry. *Mol. Cryst. Liq. Cryst.*, 21(3-4):355–373, 1973.

[19] D. Melzer and F.R.N. Nabarro. Cols and noeuds in a nematic liquid-crystal with a homeotropic cylindrical boundary. *Philos. Mag.*, 35(4):907–915, 1977.

[20] A. Pargellis, N. Turok, and B. Yurke. Monopole-antimonopole annihilation in a nematic liquid crystal. *Phys. Rev. Lett.*, 67(12):1570–1573, 1991.

[21] G.G. Peroli, G. Hillig, A. Saupe, and E.G. Virga. Orientational capillary pressure on a nematic point defect. *Phys. Rev. E*, 58(3):3259–3263, 1998.

[22] I. Vilfan, M. Vilfan, and S. Zumer. Defect structures of nematic liquid-crystals in cylindrical cavities. *Phys. Rev. A*, 43(12):6875–6880, 1991.

[23] G.G. Peroli and E.G. Virga. Annihilation of point defects in nematic liquid crystals. *Phys. Rev. E*, 54(5):5235–5241, 1996.

[24] A. N. Semenov. Interaction of point defects in a nematic liquid. *Europhys. Lett.*, 46(5):631–636, 1999.

[25] E.C. Gartland, A.M. Sonnet, and E.G. Virga. Elastic forces on nematic point defects. *Continuum Mech. Therm.*, 14(3):307–319, 2002.

[26] J. Bajc, G.G. Peroli, E.G. Virga, and S. Zumer. Dynamics of nematic point defects in a capillary with tilted boundary conditions. *Liq. Cryst.*, 29(2):213–219, 2002.

[27] R. Holyst and P. Oswald. Annihilation of point defects on a line. *Phys. Rev. E*, 65:041711, 2002.

[28] P.E. Cladis and H.R. Brand. Hedgehog-antihedgehog pair annihilation to a static soliton. *Physica A*, 326(3-4):322–332, 2003.

[29] P. Biscari, G.G. Peroli, and E.G. Virga. A statistical study for evolving arrays of nematic point defects. *Liq. Cryst.*, 26(12):1825–1832, 1999.

[30] C. Liu and N.J. Walkington. Approxiamtion of liquid crystal flows. *SIAM J. Numer. Anal.*, 37:725–741, 2000.

[31] P. Yue, J.J. Feng, C. Liu, and Shen J. A diffuse-interface method for simulating two-phase flows of complex fluids. *J. Fluid Mech.*, 515:293–317, 2004.

CHAPTER 6
Ring-like cores of cylindrically confined nematic point defects

6.1 Summary

Nematic liquid crystals confined in a cylindrical capillary and subjected to strong homeotropic anchoring conditions is a long-studied fundamental problem that uniquely incorporates nonlinearity, topological stability, defects and texture physics. Observed and predicted textures that continue to be investigated include escape radial, radial with a line defect, planar polar with two line defects, and periodic array of point defects. This paper presents theory and multiscale simulations of global and fine scale textures of nematic point defects, based on the Landau-de Gennes tensor order parameter equations. The aim of this paper is to further investigate the ring-like nature of point defect cores and its importance on texture transformation mechanisms and stability. The paper shows that the ring-like cores can be oriented either along the cylinder axis or along the radial direction. Axial rings can partially expand but are constrained by the capillary sidewalls. Radial rings can deform into elliptical structures whose major axis is along the capillary axis. The transformation between several families of textures under capillary confinement as well as their stability is discussed in terms of defect ring distortions. A unified view of nematic textures found in the cylindrical cavities is provided.

6.2 Introduction

Nematic liquid crystals are intermediate phases found in materials composed of rigid and highly anisotropic molecules, favoring parallel packing either through excluded volume effects and/or molecular forces. [1,2] These mesophases share some common properties with isotropic liquids and fully ordered crystalline solids and combine fluidity and order. Because of this unique combination, nematic liquid crystal mesophases are often referred as ordered or anisotropic fluids. Order in nematic liquid crystals is orientational. Due to this order, nematic fluids display material properties such as permittivity, refractive index, elasticity and viscosity that are anisotropic (i.e. their magnitude differs from one direction to another). [1, 2] In absence of any constraints, orientational order in a nematic liquid crystal is homogeneous to minimize bulk elastic energy and therefore neighboring rod-like molecules tend to spontaneously orient their long axis approximately parallel along a common preferred direction. However, geometry (shape and size of the container), surface anchoring (molecular orientation imposed by the surface of the container) and possibly external fields (electric, magnetic, flow) results in heterogeneous orientational order. [2, 3] Technological applications of nematic liquid crystals (e.g. displays, sensors, high-performance fibers) are invariably based on the fact that the structure and therefore the systems physical properties (e.g. optical, mechanical and rheological) can be tuned by external fields and geometric constraints.

As any other ordered materials, nematic liquid crystals may contain defects. [1,3] The presence of these defects can be detected either directly by means of optical methods or indirectly through the variations of physical properties of the system. [1,3]

From the strict topological point of view, defects in an ordered media are configurations in which some *order parameter* cannot be transformed continuously. In nematic mesophases, the order parameter is typically a unit vector field $\mathbf{n}(\mathbf{r})$ (where $\mathbf{r}$ is the position vector), called director field, giving the local average preferred orientation of the molecules; $\mathbf{n}$ is a headless vector since the states $\mathbf{n}$ and $-\mathbf{n}$ are physically indistinguishable. [1, 3] Within this framework, a defect generally corresponds to a *region* in the form of a point (0D) or a line (1D) in which the local director field exhibit a discontinuous change in orientation. In such a singular region, the director $\mathbf{n}(\mathbf{r})$ cannot be uniquely defined. Therefore, within the director description, a singular region is considered to be isotropic while a non-singular region is uniaxial nematic. Nematic defects are conventionally characterized by a strength (M) whose magnitude (usually 1/2 or 1) and sign ($\pm$) denote respectively the amount and the sense of director rotation when encircling the defect. [1, 3] [Note that some director field configurations, despite presenting no singularity, are still considered as *defects* (e.g. walls (2D) or escaped line (1D)), since they still involve large/sharp deformations.] To appropriately describe a defect one needs to employ a tensorial order parameter field rather than a vectorial one. This tensorial order parameter conventionally denoted by $\mathbf{Q}(\mathbf{r})$ is, unlike $\mathbf{n}(\mathbf{r})$, everywhere continuous including in the core of defect. $\mathbf{Q}$ can describe smooth changes between the isotropic, uniaxial and biaxial nematic states (in contrast to $\mathbf{n}(\mathbf{r})$ which can only describe the uniaxial nematic state). [1, 3–6] Properties of nematic-based systems are strongly affected by defects and their associated textures. In some cases defects are highly undesirable while in others they are essential. [2] In order to eventually reduce, remove or more

generally control them and hence optimize the performances of the nematic liquid crystal-based system one invariably needs to understand static and dynamic defect properties. [2]

The most widely found geometries for nematic-based systems are: planar (film, i.e. a mesophase sandwiched between to two parallel plates), cylindrical (ordered fluid filling a tube) and spherical (droplet). Among those systems, nematics in cylindrical capillaries exhibit a rich diversity of structures. The possible (equilibrium) configurations of a nematic fluid in a cylindrical capillary depend primarily on the molecular orientation (i.e. anchoring) imposed by the sidewalls of the cavity. The imposed orientation at the surface can be anywhere from parallel to perpendicular to the surface unit normal. Cylindrical cavities with sidewalls imposing a homeotropic anchoring (molecules forced to align their long axis parallel to the surface unit normal) have attracted the most experimental and theoretical interest to date, in part because this configuration possesses various orientational textures which are common in fiber manufacturing and in-situ composites. [7–13] There are basically four different types of nematic structures found in a cylindrically cavity with homeotropic anchoring, known as: (1) planar radial with line defect (PRLD), (2) planar polar with two line defects (PPLD), (3) escape radial (ER) and (4) escape radial with point defects (ERPD), shown in figure 6–1. While the first three configurations are two-dimensional (the system is homogenous in the third direction, collinear with the capillary axis), the fourth is completely three-dimensional. The stability of these structures depends on: (i) the size of the capillary, (ii) the nematic potential which is temperature for thermotropic nematic liquid crystals (TNLCs) and concentration for lyotropic nematic

liquid crystals (LNLCs), (iii) the elastic properties of the particular nematic liquid crystal considered. The variations of elastic properties from one nematic material to another essentially modify the (meta)stability limits/envelopes of the phase diagram. [14–16] Therefore, far from phase transitions that introduce pre-transitional elastic constant divergences, such as nematic-smectic A [1], the qualitative features of the configurations can be appropriately studied within the approximation of elastic isotropy. [17] In addition, when the nematic potential is high enough and that the material is far from the isotropic-nematic phase transition, the (meta)stability of the different configurations is only dictated by the size of the capillary.

In the PRLD configuration, which arises in small capillaries or very close to the isotropic-nematic phase transition, the molecular orientation is everywhere radial and a line defect of strength $M = +1$ runs along the capillary axis. [10–12] In larger capillaries or at higher nematic potential, the PRLD becomes unstable with respect to the PPLD structure. The PPLD structure exhibits a broken rotational symmetry and is characterized by two line defects of strength $M = +1/2$. Due to the combination of their mutual repulsion and a repulsion from the bounding curve surface, the two defect lines stabilize at a finite distance. The equilibrium defect-defect separation distance has been shown to be $\approx 0.66D$, where D is the capillary diameter. [15, 16] In large capillaries, theoretical studies predict that the energetically favorable configuration is the continuous ER. [7–9] The three-dimensional ER deformation can be seen as a PRLD configuration which has avoided the central line defect by uniformly *escaping* in the third dimension. This is explained by the topological instability of integer line defects, which is based on the notion that on the unit

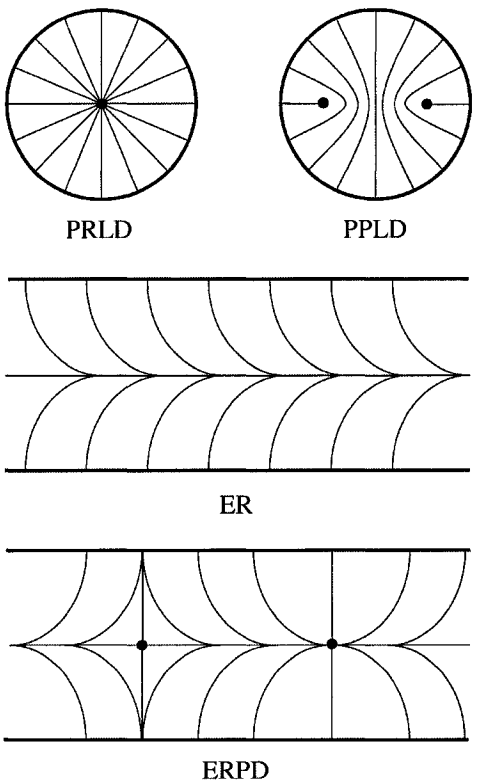

Figure 6–1: The four typical textures found in nematic capillaries subjected to homeotropic anchoring: PRLD, PPLD, ER and ERPD. Lines are everywhere tangent to the director field. Singular regions are indicated by black dots

orientation sphere, a $M = +1$ integral defect is an equatorial loop that can be smoothly and continuously eliminated by translating the loop towards one of the equators. [1,3] In practice, the ER configuration is seldom observed, as nematic-filled cylindrical capillaries usually exhibit instead the more complicated three-dimensional ERPD configuration. [7–12] The ERPD consists of partially escaped domains with a distribution of alternating radial and hyperbolic point defects along the capillary axis. Point defects are often referred as hedgehogs. The emergence of these point defects is not well understood. Generally the hypothesis is that since *escape* directions along the tube axis are energetically equivalent, they spontaneously form due to intrinsic fluctuations near the isotropic-to-nematic phase transition or due to surface irregularities. [10,12,18] It has been also suggested that they result from the presence of impurities in the cavity. [19]

Nematic liquid crystals in circular capillaries subjected to strong anchoring are model systems for non-linearity and multi-scales in soft material science. The non-linearities are expressed by the multiple solutions that include the above-mentioned different types of textures: PRLD with a single $M = +1$ line defect, PPLD with two $M = +1/2$ line defects, ER with no defects, and ERPD with alternating $M = \pm 1$ defects. The multi-scale nature of the problem arises from the disparity between the size of the capillary (micrometer scale) and the defect cores (nanometer scale). A complete static description of nematic filled cylindrical cavities subjected to homeotropic conditions involves the texture phase diagram as a function of the material elastic properties, nematic potential, and capillary radius, where the (meta)stability ranges are defined, as well as the nano-scale ordering and geometry of the defects.

Although the topic of nematic defects and textures in cylindrical capillaries has been the subject of many experimental [7–9, 12, 20, 21] and theoretical [10, 11, 15–18, 22–24] works over the last thirty years, a complete detailed picture is still lacking. As a contribution to the on-going characterization of the multi-scale ordering and non-linearity (multi-stability) in nematic-filled cylindrical cavities, this chapter focus on the exact nature of the point defects found in the ERPD texture and examines possible transformation paths to the PPLD configuration. In contrast with the basic director field description [9, 18, 20], the core of cylindrically confined point defects are not necessarily *points* in the isotropic state. [25] Indeed, orientational order in the core of hedgehogs has been shown, both experimentally [26, 27] and theoretically [28–32], to adopt a more complex but yet topologically equivalent ring-like configuration due to a core splitting mechanism. A unique contribution of this chapter is to establish the role of the ring geometry on textural transformations and texture stability, thus showing that point defects lack the dimensionality to explain textural changes.

A detailed description of orientational order in the core of cylindrically-confined nematic point defects has been given in recent theoretical studies. [33–35] According to these works, the core of a point defect splits into a uniaxial ring disclination whose axis is aligned along the axis of the cylindrical capillary. The uniaxial ring is in turn surrounded by a biaxial torus in which the degree of biaxiality attains its maximum. However, recent molecular dynamic computational studies dealing with the annihilation of nematic point defects in cylindrical capillaries have suggested that the orientation of the ring disclinations in the core of the point defects could be along

the radial direction rather than along the axial one. [36–38] No precise description of this alternate ring-like configuration is available yet to the best of our knowledge.

To eventually fully understand and characterize the ERPD texture and its connections to the other textures found in nematic cylindrical cavities, particularly the PPLD configuration, a better understanding of point defect cores is required. The first objective of this chapter is to investigate the possible ring configurations in the cores of nematic point defects confined into a cylindrical cavity. In contrast with previous studies [33–35], we use three-dimensional simulations and therefore do not assume a cylindrical symmetry of the defect structure. In addition, we consider the original Landau-de Gennes expansion and do not constrain the tensor order parameter $\mathbf{Q}$ to avoid isotropic states by using the Lyuksyutov constraint as in previous studies. [33–35] The configurations obtained are therefore entirely self-selected. The second objective of this chapter is to investigate the effect of the confinement on the geometry of the ring-like structure of the point defect core. This is done by simulating a spherically confined point defect and compared with the results obtained in the capillary. The third and last objective is to investigate the structural relationships/transitions between the *point* defects and the PPLD structure. Texture transformations from, say, PRLD to PPLD have been described using defect splitting of a $M = +1$ line defect into two $M = +1/2$ line defects, driven by changes in the capillary radius. [39] Similarly, one would expect that certain (i.e. properly oriented within the capillary) ring defects may expand and coalesce with each other and give rise to the texture transformation between ERPD and PPLD. The chapter is organized as follows: in section 6.3 we introduce the mathematical model employed,

in section 6.4 we present our computational results and in finally in section 6.5 we present our conclusions.

6.3 Modelling

6.3.1 Tensor order parameter Q_{ij}

As we mentioned earlier, defect cores in nematic liquid crystals cannot be described by a director field because of their discontinuous nature, their inherent biaxiality and steep order parameter changes. [17] An appropriate description of orientational ordering in the presence of defects therefore requires a tensor order parameter field $\mathbf{Q}(\mathbf{r})$. This tensor is symmetric traceless (*i.e.*, $Q_{ij} = Q_{ji}$ and $Q_{ii} = 0$) and therefore possesses five degrees of freedom. It can be represented, in terms of its eigensystem as follows: [35]

$$Q_{ij} = \mu_n n_i n_j + \mu_m m_i m_j + \mu_l l_i l_j \tag{6.1}$$

In this expression, $\mathbf{n}$, $\mathbf{m}$ and $\mathbf{l}$ are unit eigenvectors forming an orthogonal triad and μ_n, μ_m and μ_l are their corresponding eigenvalues. The eigenvalues μ_i $(i = 1, 2, 3)$ of the tensor order parameter are restricted by: $-1/3 \leq \mu_i \leq 2/3$ and $\mu_n + \mu_m + \mu_l = 0$. The director triad and the eigenvalues are characterizing the orientation and the strength of alignment of the phase respectively. The largest eigenvalue in magnitude or absolute value, μ_n, gives the strength of ordering along the uniaxial director $\mathbf{n}$ previously defined. The second μ_m and third μ_l eigenvalues correspond respectively to the biaxial directors $\mathbf{m}$ and $\mathbf{l}$ ($\mathbf{l} = \mathbf{n} \times \mathbf{m}$). At equilibrium, an undistorted nematic phase is uniaxial; however, in distorted regions like defect cores the phase

is likely to exhibit biaxiality. The possible ordering states that can describe the tensor order parameter are: isotropic ($\mu_1 = \mu_2 = \mu_3 = 0$; $\mathbf{Q} = 0$), positive uniaxial ($\mu_1 > \mu_2 = \mu_3$), negative uniaxial ($\mu_1 = \mu_2 > \mu_3$) and biaxial ($\mu_n \neq \mu_m \neq \mu_l$). In the negative uniaxial phase, the molecules spread orthogonally to the director. [35]

When the tensor order parameter $\mathbf{Q}$ is uniaxial, it is often useful to represent it in the following format:

$$Q_{ij} = S(n_i n_j - \frac{\delta_{ij}}{3}) \tag{6.2}$$

In this expression, S is referred as the uniaxial scalar order parameter. It describes the *amount* of order (or strength of alignment) around the uniaxial director $\mathbf{n}$ and is given by $S = 3/2(n_i Q_{ij} n_j) = 3/2\mu_n$. The Kronecker δ stands for the unit tensor. The uniaxial scalar order parameter is in the range: $-1/2 \leq S \leq 1$.

Biaxiality plays an important role in the type of solutions computed. A convenient parameter to represent it is the degree of biaxiality defined as: [35]

$$\beta^2 = 1 - 6\frac{(\mathrm{tr}\mathbf{Q}^3)^2}{(\mathrm{tr}\mathbf{Q}^2)^3} \tag{6.3}$$

which is found in the interval $[0, 1]$. In positive and negative uniaxial states $\beta^2 = 0$, while a state of maximum biaxiality corresponds to $\beta^2 = 1$.

6.3.2 Governing equation

The total free energy of a nematic liquid crystal system under strong anchoring conditions (*i.e.*, when the molecular ordering at the boundary is fixed) is written

as: [1]

$$F = \int_V f_b dr^3 = \int_V (f_h + f_g) dr^3 \tag{6.4}$$

In this expression, f_b, f_h and f_g represent the total bulk, homogeneous bulk and gradient bulk free energy densities, respectively. The homogeneous free energy describes the short-range ordering effects related to the amplitude of the tensor order parameter. This expression can describe the first order isotropic-nematic phase transition but also, and more importantly in our work, the variations of the nematic ordering in the vicinity of defects. This contribution is often referred as the Landau-de Gennes free energy. According to Doi's formalism [4, 5], this expansion of the order parameter may be written as:

$$f_h = \frac{A}{2}(1 - \frac{U}{3})Q_{ij}Q_{ji} - \frac{AU}{3}Q_{ij}Q_{jk}Q_{ki} + \frac{AU}{4}(Q_{ij}Q_{ji})^2 \tag{6.5}$$

In this expression A is an energy density scale (unit of energy per cubic meter), U is a dimensionless phenomenological parameter called nematic potential which controls the magnitude of the equilibrium tensor order parameter. In general the nematic potential U can be assigned a dependence on either temperature or concentration depending on the nature of the nematic liquid crystal considered (*i.e.*, thermotropic or lyotropic). In our study U is taken to be proportional to concentration and according to Doi's theory, $U = 3C/C^*$ where C and C^* are the number and critical number density of rod-like molecules, respectively. [4,5] Accordingly, the energy density scale $A = C^*kT$ where k and T are the Boltzmann constant and the temperature of the system, respectively.

At equilibrium and away from distorted regions, the tensor order parameter **Q** given by Eq. 6.5 is uniaxial. Under these conditions, the value of the scalar order parameter is given by the relation:

$$S_e = \frac{1}{4} + \frac{3}{4}\sqrt{1 - \frac{8}{3U}} \tag{6.6}$$

Within this framework, the first order phase isotropic-nematic phase transition occurs at nematic potential $U_{IN} = 2.7$. Also, in this model, the system is isotropic for $U < U_{IN}$ and nematic for $U > U_{IN}$. The limit of metastability for the isotropic and nematic phase are $U^* = 3$ and $U^{**} = 8/3$, respectively. [4, 5]

The gradient f_g contribution in Eq.(6.4), represents the energy density penalty associated with the long-range variations of the tensor order parameter **Q** in the nematic phase. As mentioned in the introduction, the elastic anisotropy of nematic essentially modifies the limits/envelopes defining the domain of (meta)stability of the different defect configurations but not their qualitative features. Since exploring the entire parametric space is beyond the scope of this chapter we therefore consider the case of elastic isotropy. In the one constant approximation, the gradient energy expressed in terms of **Q** reads: [4, 40]

$$f_g = \frac{L}{2}\nabla_k Q_{ij} \nabla_k Q_{ij} \tag{6.7}$$

In this equation, L is a material-dependent elastic constant (unit of energy per unit length).

The equilibrium tensor order parameter field is the one that minimizes the total free energy under the different constraints (shape and size of the container, anchoring

at its surface, etc...) and is obtained from variational calculus principles. Under strong anchoring conditions, the Euler-Lagrange equation associated with the free energy of the nematic liquid crystal reads:

$$\frac{\delta F}{\delta Q_{\alpha\beta}} = \frac{\partial f_b}{\partial Q_{\alpha\beta}} - \nabla_\gamma \frac{\partial f_b}{\partial \nabla_\gamma Q_{\alpha\beta}} = 0 \tag{6.8}$$

Solving directly the non-linear steady state equation (6.8) iteratively is difficult given that the problem present multiple solutions which all depend on the initial guess. In addition, convergence to one of the many stable solutions is only insured if the initial guess is close enough to a basin of attraction. To palliate this problem it is customary to introduce a fictitious time dependency to the problem and therefore obtain a physical evolution of the solution. The pseudo-transient or false-transient problem we solve in order to obtained the different solution families follow from variational principles and reads: [4, 13, 40–42]

$$\gamma \frac{\partial Q_{\alpha\beta}}{\partial t} = -\frac{\delta F}{\delta Q_{\alpha\beta}} \tag{6.9}$$

In this equation γ is a kinematic constant known as rotational viscosity. [4, 40]

6.3.3 Geometries and auxiliary conditions

In contrast to previous studies [33–35] on the ring-like core of point defects, we use three-dimensional simulations which allow the emergence of additional possible ring-like core configurations. In order to assess our objectives we used cylindrical and spherical computational volumes. Nevertheless, in order to reduce the high

computational cost of the simulations we have considered 1/8 of the computational volumes using the (mirror) symmetry properties of the expected solutions.

Furthermore, we use non-dimensionalization in order to reduce the number of parameters and facilitate the analysis of the results. Using the energy scale A, we define the dimensionless bulk free energy density $\bar{f}_b = f_b/A$ where the overbar indicates the dimensionless quantity. The dimensionless position vector is defined as $\bar{\mathbf{r}} = \mathbf{r}/R$ where R stands for the radius of the cylindrical or spherical cavity. Accordingly, we define the dimensionless nabla operator $\bar{\nabla} = R\nabla$ and dimensionless total energy $\bar{F} = \frac{F}{AR^3}$. The fixed, reference length scale in the problem is the nematic coherence length defined as $\xi = \sqrt{L/A}$. This length gives a characteristic scale for the amplitude variations of the tensor order parameter and the size of defect cores. The ratio R/ξ, corresponding to the dimensionless nematic coherence length reciprocal, therefore represents the relative size of the cavity.

The boundary conditions are as follows: at the wall of the cavity, the tensor order parameter is assumed to be uniaxial and to describe a rigid radial anchoring condition so that $Q_{ij}(r = R) = S_e(e_i^r e_j^r - \frac{\delta_{ij}}{3})$, where $\mathbf{e^r}$ is the unit vector along the radial direction. The interior boundary conditions insure the mirror symmetries. In the case of the cylindrical cavity, a *no flux* condition is used on the exterior face so as to emulate an infinitely long cavity; this condition does not introduce any spurious effects as tested by using different computational grids.

The model used in this work contains two parameters: the nematic potential U and the reduced cavity size R/ξ. Exploring the entire parametric space is beyond the scope of this chapter and is left for future work. For all the simulation results

presented, the nematic potential is set to $U = 6$ which corresponds to a deep nematic phase with an equilibrium scalar order parameter of $S_e = 0.809$. Note that other values of U in the stable nematic range do not change the structures under study. This chapter finds and analyzes solutions for different cavity sizes R/ξ in the range $[17.5, 30]$. This choice is motivated by the fact that the point defects are only stable in large cavities; the upper bound is dictated by our memory limitation while the lower bound corresponds to the limit of stability of the point defect. A previous two dimensional computational study has used a similar range of cavity radii for the exploration of spherically confined point defects. [14]

6.3.4 Computational procedure and post-processing tools

The governing partial differential equation for the tensor order parameter $\mathbf{Q}(\mathbf{r})$, Eq. (6.9) is solved using a standard iterative method. The space discretization is achieved using the Galerkin finite element method. A pseudo-transient continuation method was used to explore the parametric range. The density of element is higher in the regions describing steep changes in the tensor order parameter amplitude. In those delicate regions, the size of the triangular elements is always smaller than the ratio ξ/R.

The order parameter fields $\mathbf{Q}(\mathbf{r})$ corresponding to each computed solutions are visualized by means of cuboids built from the eigensystem of the tensor. [17] The axes of the cuboids are aligned with the eigenvectors while the size of each side is proportional to the eigenvalues. Given that the eigenvalues of $\mathbf{Q}(\mathbf{r})$ can be negative,

we use instead the shifted tensor $\mathbf{M} = \mathbf{Q} + \delta/3s$. [33] Using this technique, it is possible to distinguish between isotropic (all edges of the cuboid are equal), uniaxial (two edges are equal) and biaxial (all three edges are different) states.

6.4 Results and discussions

6.4.1 Ring-like disclination cores of nematic point defects

This subsection present actual numerical results obtained by solving Eq.(6.9). Within our 3D computational space, two different types of ring-like core structures are found for the cylindrically-confined point defects depending on the type of initial configuration considered. Dependence to initial configuration is the hallmark of non-linearity, [43] which is here introduce by the homogenous part of the free energy density. In the first type of configuration, the ring axis is aligned along the axis of the cylindrical cavity whereas in the second type of configuration, the ring axis is aligned along the normal of the capillary surface, that is, along the radial coordinate. We denote the former and latter configurations as the z-ring and r-ring core solutions, respectively. Schematics of the two ring-like core configurations in the case of radial and hyperbolic point defects are shown in figure 6–2.

Z-ring core. We first examine the computed z-ring core configuration which is obtained using an approximate z-ring like initial guess. The family of solutions of this configuration has only one member. Within the z-ring arrangement, the cylindrical symmetry of the far director field is transferred to the inner-core structure of the point defect. The z-ring core solution is found for both the radial and hyperbolic point defects. Figure 6–3 shows the two computed configurations in terms of a

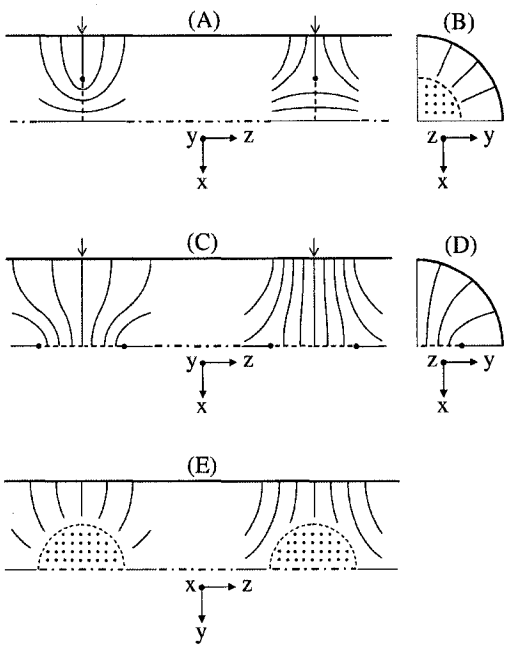

Figure 6–2: Ring-like cores of radial and hyperbolic nematic point defects embedded in a cylindrical cavity. Lines are tangent everywhere to the director field. (A) represents a longitudinal cross-section through the radial and hyperbolic z-rings. (B) corresponds to the transversal cross-section through the center of each defect as denoted by the arrows. (C) and (E) are mutually orthogonal longitudinal cross-sections through the radial and hyperbolic r-rings. (D) shows the transversal cross-section through the center of each defect as indicated by the arrows.

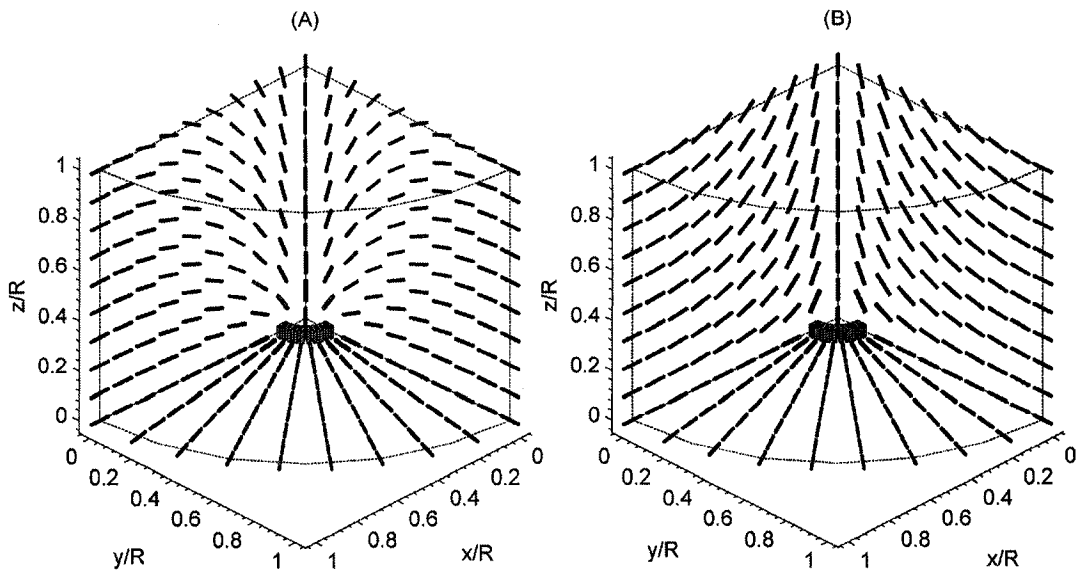

Figure 6–3: Z-ring cores of the cylindrically confined radial and hyperbolic point defects. The cuboid fields are represented on three faces of the computational volume for the ease of visualization.

cuboid field for the reduced cavity radius $R/\xi = 25$. The left (A) and right (B) plots correspond to the radial and hyperbolic form of the point defect, respectively.

The figure shows that the structures are, in both cases, entirely cylindrically symmetric and that the order is essentially uniaxial except in a narrow circular region close to the z-axis of the cavity where it becomes biaxial. Along the cross section defined by the plane $z = 0$, the smooth shape evolution of the cuboids shows that the preferred molecular orientation goes from radial, at the wall, to tangential, in the biaxial ring, to axial, along the cavity axis.

Complementarily, figure 6–4 gives the variations of tensor order parameter eigenvalues along the radial direction at $z = 0$ in the case of the radial configuration for

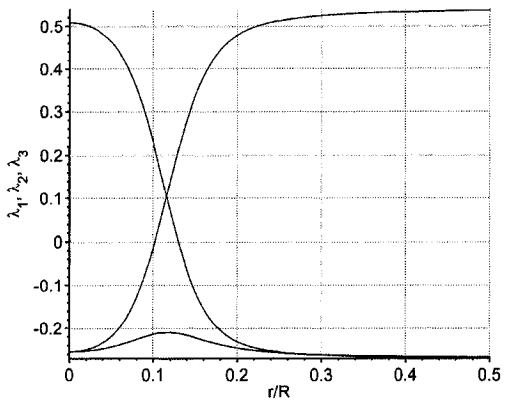

Figure 6–4: Eigenvalues of the **Q** tensor along the radial direction at $z = 0$.

$R/\xi = 25$. Note that given the elastic isotropy considered, the profiles are identical in the radial and hyperbolic forms of the point defects.

The eigenvalue profiles shown in this figure are qualitatively analogous to the ones found in the cases of ring disclination-like core occurring in spherically confined nematic subjected to homeotropic anchoring. [14] They attest that the z-ring solution is effectively uniaxial away from the eigenvalue exchange region corresponding to the ring disclination and in which order is biaxial with a negative scalar order parameter. Biaxiality is clearly a distinctive feature in the ring-like core of the point defect since no isotropic state is ever found. Another representation of the biaxiality variation in the defect core is given in figure 6–5 which is an iso-surface plot of the biaxial parameter β^2 as a function of the (x, y, z) coordinates; in this graph, which clearly shows the toroidal variations of biaxiality, the iso-level is $\beta^2 = 0.5$. In this figure, the β^2 envelopes describe a torus. The evolution of biaxiality in the z-ring defect is in qualitative agreement with the theoretical predictions obtained in previous

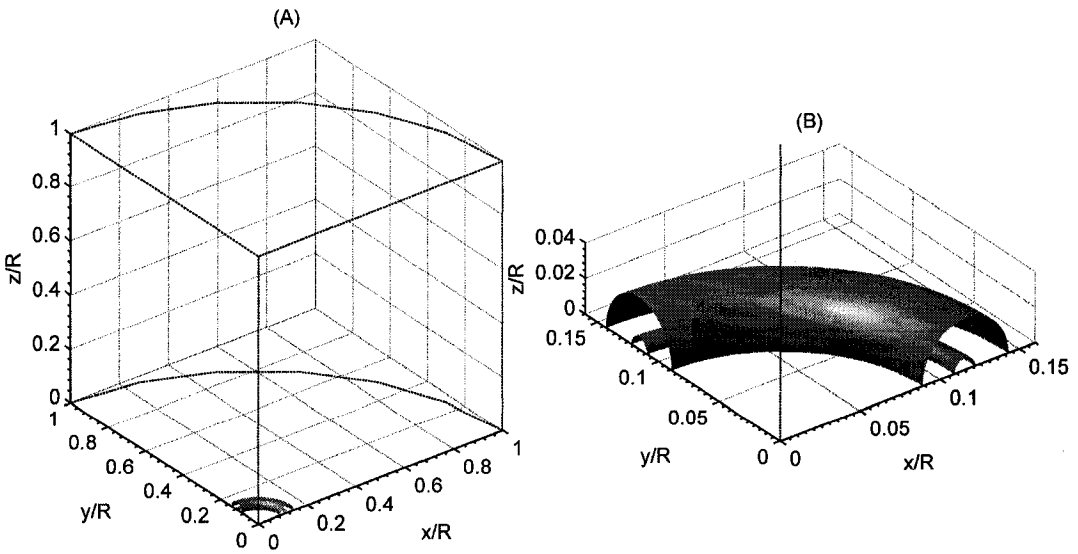

Figure 6–5: Toroidal variations of biaxiality within the z-ring like core disclination. The iso-level is $\beta^2 = 0.5$ while the (A) and (B) plots correspond to the original and enlarged view of the torus, respectively.

works. [33–35] However, in contrast to these studies, no (Lyuksyutov) constraint is applied to the degree of biaxiality of the tensor order parameter $\mathbf{Q}$, and the evolution of biaxiality inside the ring disclination is completely self-selected. This suggests that it is not necessary to apply such constraint in our work.

In our simulations we find that the cross section of the biaxial torus (distance separating the peaks of maximum biaxiality) is always perfectly circular. As in previous studies, [33–35] we note that there is a uniaxial *line* embedded in the center of a biaxial torus. Along this uniaxial sheath the scalar order parameter S is negative as indicated by figure 6–4, meaning that the nematic molecules tend to spread perpendicularly to a director field everywhere tangent to the ring.

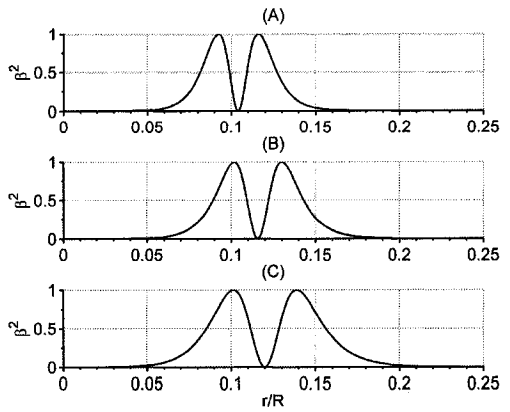

Figure 6–6: Profiles of biaxiality of z-ring like core disclination along the radial direction. Cases (A), (B) and (C) corresponds respectively to the capillary sizes $R/\xi = 30, 25, 20$, respectively.

Given its cylindrical symmetry and circular nature, the biaxial structure of the z-ring defect core can be characterized by plotting the variation of the degree of biaxiality β^2 along the radial direction on the $z = 0$ plane. Figure 6–6 illustrates the variations for the capillary sizes $R/\xi = 30, 25, 20$. It appears from figure 6–6 that the cross section of the torus increases with a decreasing capillary radius. Additionally, the radius of torus (distance from the origin of the coordinate system to the uniaxial sheath) follows the same trend. The growth of the z-ring is restricted by sidewall forces so that the maximum radius of the z-ring is found to be around $r_c \sim 0.12$ for $R/\xi \sim 18$.

R-ring core. The other core configuration obtained for cylindrically confined point defects is the r-ring disclination which is obtained using an approximate point defect structure with an isotropic core (see fig. 6–2). In contrast to the z-ring configuration previously described the r-ring solution does not possess cylindrical

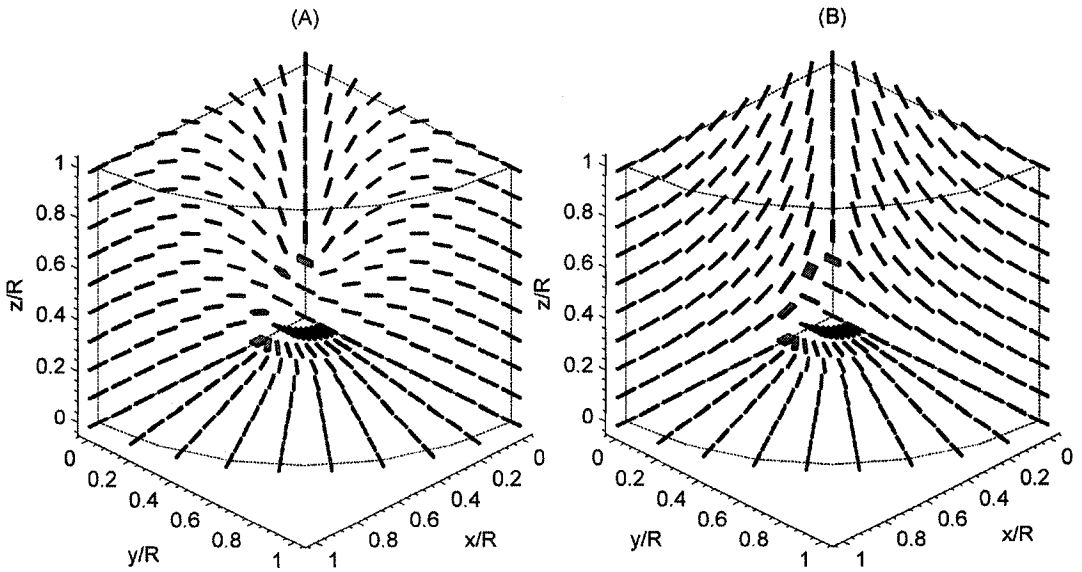

Figure 6–7: R-ring cores of the cylindrically confined radial and hyperbolic point defects. The cuboid fields are represented on three faces of the computational volume for the ease of visualization.

symmetry as the ring axis is now positioned parallel to the radial direction of the cavity. To date, studies [33–35] have assumed that the ring axis was aligned with the cavity and that the configuration was consequently cylindrically symmetric. However, recent molecular dynamic simulations [36–38] suggest that the ring could be instead oriented along the radial direction and therefore break the symmetry. No description of the r-ring solution has been however proposed. As for the z-ring, the r-ring solution can be equivalently found for the radial and hyperbolic point defects. Figure 6–7 shows the tensor field corresponding to radial and hyperbolic solutions for the reduced cavity radius $R/\xi = 25$. The left (A) and right (B) plots correspond to the radial and hyperbolic form of the point defect, respectively.

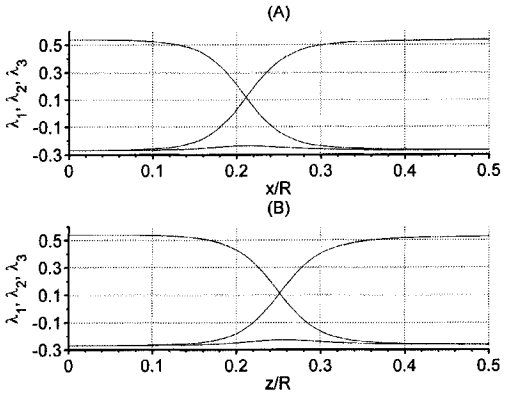

Figure 6–8: Eigenvalues of the **Q** tensor along the x and z-directions at $y = 0$.

In these plots, the biaxial r-ring lies on $y = 0$ plane and is parallel to the y-axis. At this point one can note that in contrast to the z-ring configuration which possesses a single ring axis (i.e. the z-axis), the r-ring configuration may take any orientation along the radial direction and therefore possess an infinity of possible equivalent orientations. In our simulations, the orientation of the ring is self-selected along the y-axis but it could be also equivalently oriented along the x-axis. As for the z-ring, in figure 6–7, smooth orientation transitions occur from the periphery to the core of the point defect through biaxial states. Despite their difference of orientations, the z- and r-ring configurations display similar characteristics. Figure 6–8 provides the tensor order parameter eigenvalue variations along the x and z-directions for the same parameter used in figure 6–7.

The profiles vary in a manner similar to that of the z-ring core (See fig. 6–4). There are, however, two essential differences: (1) the radius of the biaxial torus is

significantly larger than that found in the case of the z-ring core for equivalent parametric conditions, and (2) the torus is not circular (at least for this set of parametric values, as further discussed below) but rather elliptical with the major axis along the axial z-direction and the minor axis along the radial r-direction.

To get a better visual representation of the r-ring core, figure 6–9 provides an iso-surface plot of the degree of biaxiality β^2 for the iso-level 0.5 in the parametric conditions of fig. 6–7. Figure 6–9 attests that the distribution of the biaxial envelopes in the z-ring and r-ring cores is qualitatively similar with the difference however that r-ring configuration breaks the cylindrical symmetry. Given this lack of symmetry, two axes belonging to the $r = 0$ plane must be taken to describe the r-ring core configuration.

Figure 6–10 illustrates the evolution of the degree of biaxiality β^2 along the radial and axial direction for the relative capillary sizes $R/\xi = 30, 25, 22.5$. As noticed in the case of the z-ring core, the torus of the r-ring cores are essentially circular. One can see that for equivalent parametric and geometric conditions, the radii of the ring-disclinations are substantially larger in the r-ring configurations than in the z-ring ones. More importantly, our simulations tend to indicate that in large cavities (i.e. for $R/\xi \gg 30$), the biaxial torus is essentially circular (like the z-ring core) but that in small cavities, it is elliptical with major axis along the cavity axis. Moreover, as the cavity diameter decreases, the torus tends to deform faster in the axial than in the radial direction. The sensitivity of the torus geometry on the cavity radius is noticeably more significant in the r-ring core than in the z-ring core.

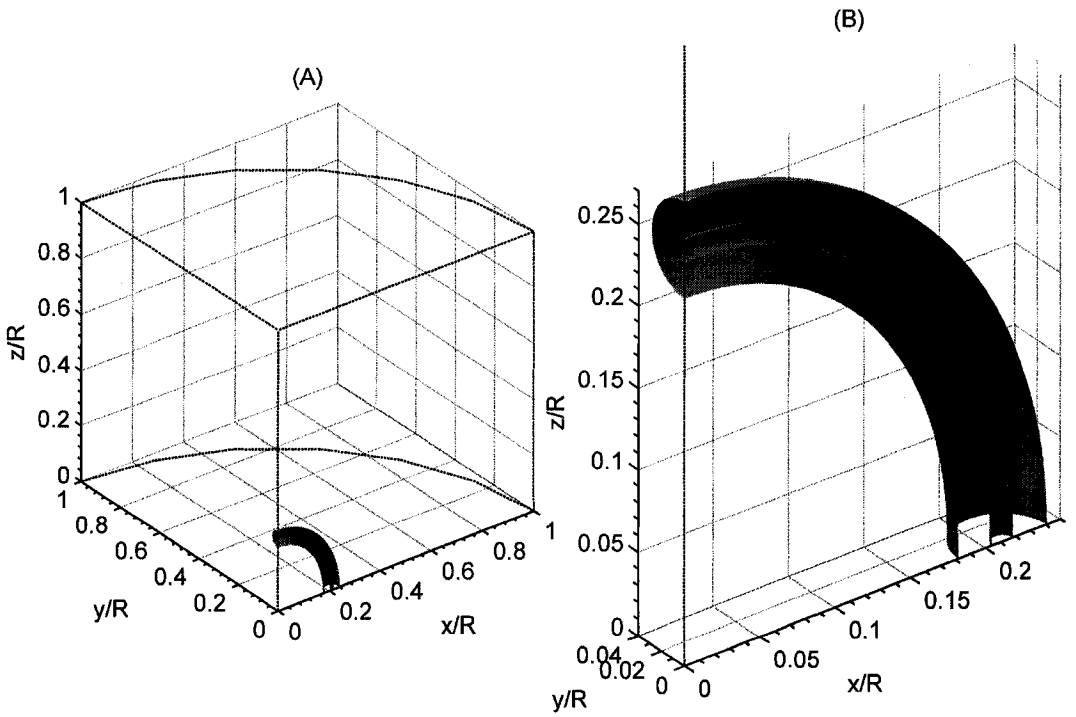

Figure 6–9: Toroidal variations of biaxiality within the r-ring like core disclination. The iso-level is $\beta^2 = 0.5$ while the (A) and (B) plots correspond to the original and enlarged view of the torus, respectively.

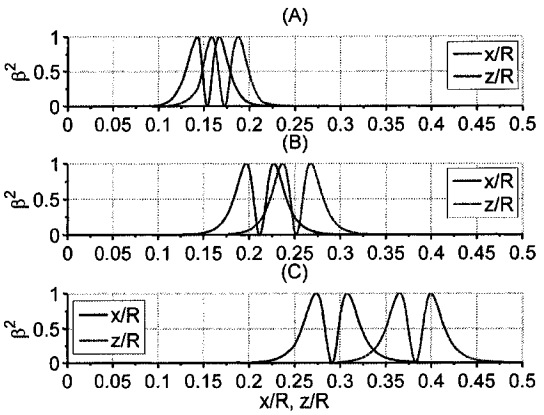

Figure 6–10: Profiles of biaxiality of r-ring core disclination along the radial and axial directions. Cases (A), (B) and (C) corresponds respectively to the capillary sizes $R/\xi = 30, 25, 22.5$, respectively.

6.4.2 Confinement effects

In order to assess the role of confinement on the structure of the ring-core disclinations, we have additionally computed the fine structure of a point defect in a spherical droplet. Figure 6–11 illustrates the biaxial ring-like configuration adopted by the core of a radial hedgehog for $U = 6$ and $R/\xi = 25$. This result is in qualitative agreement with the results obtained in previous two-dimensional simulations. [14] There is an infinite possibility of ring orientation in the sphere. While the far-director field exhibits the spherical symmetry of the confinement, the ring-like core displays a cylindrical symmetry. As for the z-ring structure found in the core of a cylindrically confined point defect, both characteristic cross section of the torus are circular.

To see the effects of parametric conditions on the geometry evolution of the ring disclination core figure 6–12 illustrates the variations of the degree of biaxiality β^2 along the spherical radius ρ at the nematic potential $U = 6$ for three different cavity

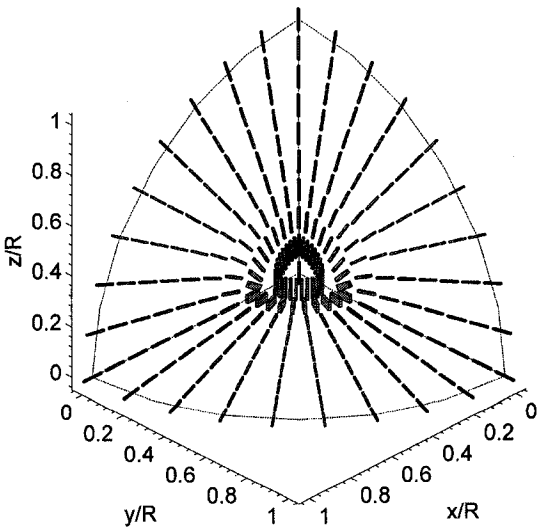

Figure 6–11: Ring-like disclination core of a spherically confined radial point defect. The cuboid fields are represented on three faces of the computational volume for the ease of visualization.

size $R/\xi = 30, 25, 20$. Comparison between these profiles and the profiles obtained for the z-ring core (in the cylindrical confinement) shows that the characteristic radii of the torus are significantly larger in the spherical confinement.

6.4.3 Hedgehog-to-planar polar structural transition

In this section we report the structural transitions we have observed between the point defects with ring-like cores and the planar polar texture. In our simulations, this transition is trigger by a decrease of the cavity's relative size. Indeed, below a certain cavity size, the stable equilibrium configuration is the PPLD structure. The threshold cavity radius is not the same when the point defect displays the r-ring vs. z-ring core. In the case of the r-ring core the critical radius at which the structural

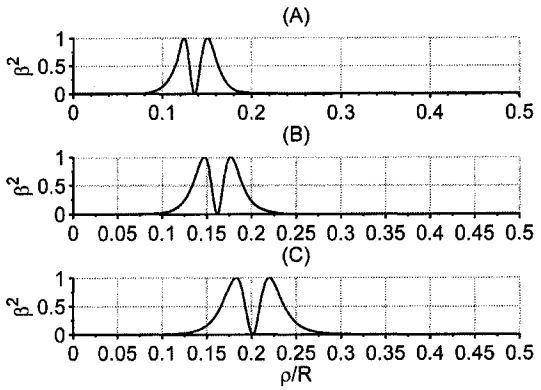

Figure 6–12: Eigenvalues of the $\mathbf{Q}$ tensor along the radial direction ρ.

transition occurs is $R/\xi \sim 21$. We first examine the transformation from the r-ring core hedgehog to the PPLD. In order to see the transformation from the two structures we solve the false-transient problem given by Eq. (6.9). Figure 6–13 gives the time evolution of the biaxial torus during the transition from the point defect with r-ring core to the planar polar texture with two line defects. In this figure each *branch* corresponds to the iso-value 0.5 of the biaxial parameter β^2. The critical radius of instability for the r-ring core is $R/\xi \sim 21$.

As one can see from figure 6–13, the transformation causes the radius of the torus to increase progressively in both the radial and axial directions. The extension of the torus in the axial direction does not present any restriction and is therefore faster than in the radial direction. We hypothesize that the r-ring would expand toward the end-caps of the cylindrical cavity no matter what its size. In contrast, the extension of the torus in the radial direction is restricted by the capillary sidewall and associated force balance. As mentioned earlier, the equilibrium distance between the two lines' defects within the planar polar texture is dictated by the force balance between the

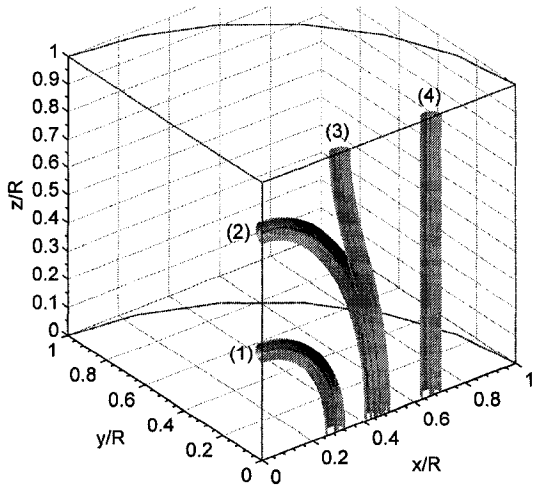

Figure 6–13: Time evolution of the biaxial torus during the *opening* of the r-ring core. The labels (1)-(4) give the order of the sequence.

mutual repulsion of the two line defects and the repulsion from the surface. [15,16] In fact, within the case of isotropic elasticity, the equilibrium defect-defect separation distance has been shown to be $\approx 0.66D$. [15,16] Hence the maximum extension of the torus along the radial direction is $\approx 0.66R$. This critical separation between the line defects is observed in our simulations (See figure 6–13). Due to our limited computer memory we have not been able to consider a long cylindrical cavity, we therefore observe an *early* the breakage of the loop which leads to the PPLD configuration. Despite this limitation, the simulation provides useful insights on the structural transformation phenomenon. Within a longer capillary, one can easily imagine that the ring would first reach its maximal radial extension then continue to grow in the axial direction until meeting the lateral limits of the cavity or meet another ring. Indeed experiments tend to show that point defects are usually found in series leading to the ERPD texture rather than isolated. Figure 6–14 give schematics

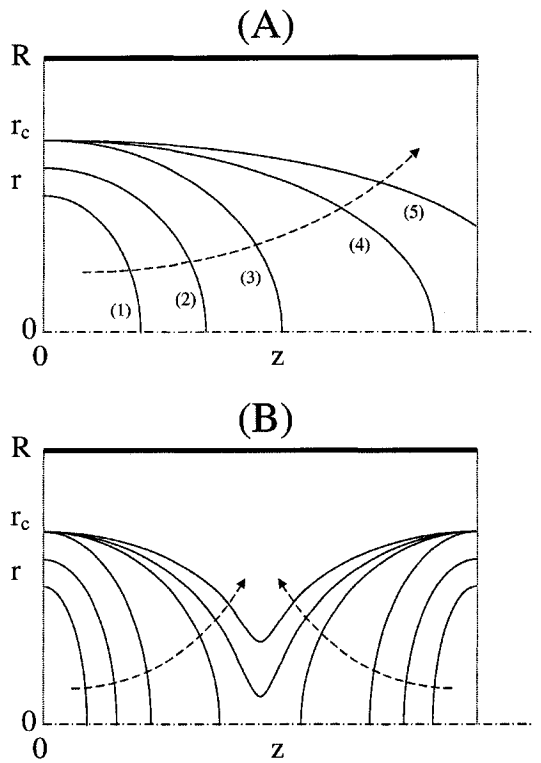

Figure 6–14: Evolution of the ring core of a point defect in an unbounded cylindrical cavity (A) and in the presence of neighboring point defect with similar r-ring core (B). The critical radial extension of the ring is given by $r_c \approx 0.66$. Arrows and numbers indicate the structure progression with time

of the ring growing process and the potential transformation into the planar polar texture with line defects in an unbounded cylindrical capillary (A) and in the presence of a neighboring point defect with an r-ring core (B). These results and scenarios are in agreement with the observations made in molecular dynamics studies on the annihilation of point defects within a cylindrical capillary and the possible ERPD to PPLD transition. [38]

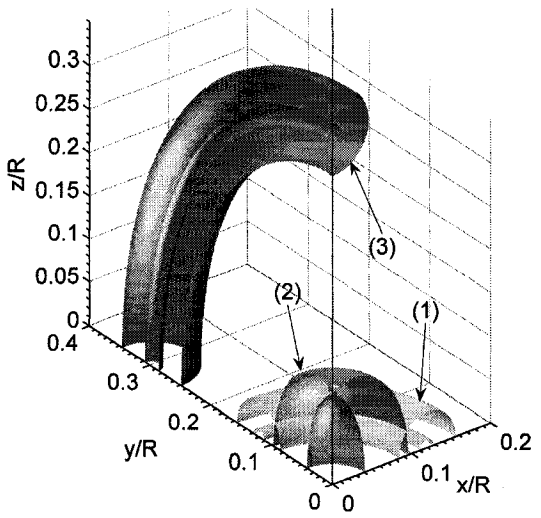

Figure 6–15: Time evolution of the biaxial torus during the transformation from the z-ring to r-ring core. The labels (1)-(3) give the order of the sequence.

In the case of the point defect with a z-ring core the transformation is found to occur at lower critical cavity radius $R/\xi \sim 17.5$. The transformation process is also found to be significantly more involving than in the case of the r-ring core as the z-ring does not permit a direct transition to the PPLD texture. Indeed, the biaxial torus of the z-ring core is found to first shrink into a spherical envelope, before subsequently changing into an r-ring core. This r-ring torus then eventually opens as previously described. Figure 6–15 illustrates the mutation of the torus of the z-ring core into an r-ring core as time evolves.

6.5 Summary and conclusions

In this chapter we have investigated the fine ring-like structure of point defect cores occurring in cylindrical capillaries. Two types of core configurations are found

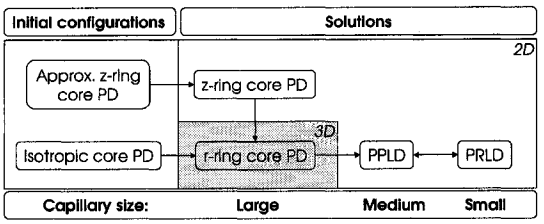

Figure 6–16: Summary of the texture connections investigated in this work. PD, PPLD and PRLD stand for point defect, planar polar with line defects and planar radial with line defect, respectively.

and described: the z-ring core whose ring-axis is along the capillary axis and the r-ring core whose axis is aligned along the radial direction. In contrast to previous studies, [33–35] the z-ring core was obtained in a self-selected fashion, without forcing the tensor order parameter $\mathbf{Q}$ to be biaxial and no cylindrical symmetry was assumed as the simulations were three-dimensional. Despite some previous indications of its existence, [36–38] the r-ring core configuration has never been described before. In contrast to its axial counterpart, the r-ring core structure does not retain the cylindrical symmetry of the far-field director field. Despite displaying qualitative similarities, the two ring structures still present some distinctive features that are intimately connected to the nature of their confinement. The r-ring core possesses a higher probability of occurrence since the ring has an infinite possibility of axis orientations along the radial direction. In contrast, the equilibrium of the z-ring ring core is rather fragile as it possesses a single possible axis orientation, along the cavity axis. The cross section of the biaxial torus characterizing the ring-like core structure is found to always be circular. Given that it is restrained by the cavity sidewalls, the biaxial torus characterizing the z-ring core solution is always perfectly

circular. The radial extension of the z-ring core is restricted by the sidewall forces so that the maximum radius reached by the ring is $r_c \sim 0.12$. The situation is however different in the case of the r-ring core, since in that case the ring can freely expand along the axial direction. What we observed is that in the limit of large cavity radii, the torus tends to be circular. In smaller cavities however, one observes the expansion of the ring along the axial direction. When the radius becomes too small to insure the stability of the point defect, a transition towards the planar polar configuration is initiated. In the case that the point defect displays the r-ring core structure, the transformation consists in the expansion of the ring towards the end-caps of the capillary or towards another point defect with an r-ring structure in the ERPD texture (This last scenario was not numerically explored in this chapter but should be reported in the next future). The transition from the ERPD to the PPLD by extension of the r-ring structure, predicted in previous work [38], has been described. When the z-ring core is involved, the transformation consists in a prior shrinkage of the ring into a spherical pellet followed by the subsequent creation of an r-ring core which finally enlarge along the axial direction. The r-ring core forming the point defect is therefore pivotal. Figure 6–16 is summarizing the texture multiplicity found in nematic-filled cylindrical cavities subjected to strong homeotropic anchoring we have studied in this work. We have additionally inspected the effect of confinement on the ring-like core of the point defect. In contrast to cylindrically confined point defects, spherically confined hedgehogs have only one ring-like core structure but have the possibility of a uniaxial isotropic core solution. The ring axis can be along any radial direction in the sphere with equivalent probability. Given

its symmetry features, the ring-like core in the sphere compares well with the z-ring core in cylindrical confinement. For an equivalent cavity radius, the biaxial torus in the droplet is nevertheless found to be significantly larger than in the cylindrical capillary. The computational results provide new and significant insights on nematic liquid crystal defect physics, textures, and topological transformation under cylindrical and spherical confinement.

REFERENCES

[1] P.G. de Gennes and J. Prost. *The physics of liquid crystals.* Oxford University Press, New York, 1995.

[2] P.J. Collings. *Liquid crystals: nature's delicate phase of matter.* Princeton University Press, Princeton, NJ, 2001.

[3] M. Kleman and O.D. Lavrentovich. *Soft Matter Physics: An Introduction.* Springer, New York, 2002.

[4] A.N. Beris and B.J. Edwards. *Thermodynamics of Flowing Systems.* Oxford University Press, New York, 1994.

[5] M. Doi. *The Theory of Polymer Dynamics.* Oxford University Press, New York, 1998.

[6] R.G. Larson. *The structure and rheology of complex fluids.* Oxford University Press, New York, 1999.

[7] C. Williams, .P Pieranski, and P. E. Cladis. Nonsingular s=+1 screw disclination lines in nematics. *Phys. Rev. Lett.*, 29(2):90, 1972.

[8] C.E. Williams, P.E. Cladis, and M. Kleman. Screw disclinations in nematic samples with cylindrical symmetry. *Mol. Cryst. Liq. Cryst.*, 21(3-4):355–373, 1973.

[9] R.B. Meyer. Existence of even indexed disclinations in nematic liquid-crystals. *Philos. Mag.*, 27(2):405–424, 1973.

[10] S. Kralj and S. Zumer. Saddle-splay elasticity of nematic structures confined to a cylindrical capillary. *Phys. Rev. E*, 51(1):366–379, 1995.

[11] S.V. Burylov. Equilibrium configuration of a nematic liquid crystal confined to a cylindrical cavity. *J. Exp. Theor. Phys.*, 85(5):873–886, 1997.

[12] G.P. Crawford, D.W. Allender, and J.W. Doane. Surface elastic and molecular-anchoring properties of nematic liquid-crystals confined to cylindrical cavities. *Phys. Rev. A*, 45(12):8693–8708, 1992.

[13] A.G. Cheong and A.D. Rey. Texture dependence of capillary instabilities in nematic liquid crystalline fibres. *Liq. Cryst.*, 31(9):1271–1284, 2004.

[14] S. Mkaddem and E.C. Gartland. Fine structure of defects in radial nematic droplets. *Phys. Rev. E*, 62(5):6694–6705, 2000.

[15] J. Yan and A.D. Rey. Texture formation in carbonaceous mesophase fibers. *Phys. Rev. E*, 65:031713–1–14, 2002.

[16] J. Yan and A.D. Rey. Theory and simulation of texture formation in mesophase carbon fibers. *Carbon*, 40:2647–2660, 2002.

[17] A. Sonnet, A. Kilian, and S. Hess. Alignment tensor versus director - description of defects in nematic liquid-crystals. *Phys. Rev. E*, 52(1):718–722, 1995.

[18] I. Vilfan, M. Vilfan, and S. Zumer. Defect structures of nematic liquid-crystals in cylindrical cavities. *Phys. Rev. A*, 43(12):6875–6880, 1991.

[19] A.M. Donald and A.H. Windle. *Liquid crystalline polymers.* Cambridge University Press, Cambridge, 1992.

[20] P.E. Cladis and M. Kleman. Non-singular disclinations of strength s=+1 in nematics. *J. Phys. (France)*, 33(5-6):591, 1972.

[21] P.E. Cladis and H.R. Brand. Hedgehog-antihedgehog pair annihilation to a static soliton. *Physica A*, 326(3-4):322–332, 2003.

[22] E.C. Gartland, P. Palffy-Muhoray, and R.S. Varga. Numerical minimization of the landau-de-gennes free-energy - defects in cylindrical capillaries. *Mol. Cryst. Liq. Cryst.*, 199:429–452, 1991.

[23] Z. Bradac, S. Kralj, and S. Zumer. Molecular dynamics study of nematic structures confined to a cylindrical cavity. *Phys. Rev. E*, 58(6):7447–7454, 1998.

[24] A.M. Smondyrev and R.A. Pelcovits. Nematic structures in cylindrical cavities. *Liq. Cryst.*, 26(2):235–240, 1999.

[25] M. Kleman and O.D. Lavrentovich. Topological point defects in nematic liquid crystals. *Philos. Mag.*, 86(25-26):4117–4137, 2006.

[26] D. Melzer and F.R.N. Nabarro. Cols and noeuds in a nematic liquid-crystal with a homeotropic cylindrical boundary. *Philos. Mag.*, 35(4):907–915, 1977.

[27] O.D. Lavrentovich and E.M. Terentiev. Phase-transition with the change of symmetry of topological point-defects (hedgehogs) in a nematic liquid-crystal. *Zh. Eksp. Teor. Fiz.*, 91:2084–2096, 1986.

[28] H. Mori and H. Nakanishi. On the stability of topologically non-trivial point-defects. *J. Phys. Soc. Japan*, 57:1281–1286, 1988.

[29] E.M. Terentjev. Disclination loops, standing alone and around solid particles, in nematic liquid-crystals. *Phys. Rev. E*, 51(2):1330–1337, 1995.

[30] O.D. Lavrentovich, T. Ishikawa, and E.M. Terentjev. Disclination loop in mori-nakanishi ansatz: Role of the divergence elasticity. *Mol. Cryst. Liq. Cryst.*, 299:301–306, 1997.

[31] T.C. Lubensky, D. Pettey, N. Currier, and H. Stark. Topological defects and interactions in nematic emulsions. *Phys. Rev. E*, 57(1):610–625, 1998.

[32] J.-I. Fukuda and H. Yokoyama. Stability of a hyperbolic disclination ring in a nematic liquid crystal. *Phys. Rev. E*, 66:012703–4, 2002.

[33] S. Kralj and E.G. Virga. Universal fine structure of nematic hedgehogs. *J. Phys. A*, 34:829–838, 2001.

[34] S. Kralj and E.G. Virga. Core hysteresis in nematic defects. *Phys. Rev. E*, 66:021703, 2002.

[35] S. Kralj, E.G. Virga, and S. Zumer. Biaxial torus around nematic point defects. *Phys. Rev. E*, 60(2):1858–1866, 1999.

[36] Z. Bradac, S. Kralj, M. Svetec, and S. Zumer. Annihilation of nematic point defects: Postcollision scenarios. *Phys. Rev. E*, 67(5):050702, 2003.

[37] M. Svetec, Z. Bradac, S. Kralj, and S. Zumer. Hedgehog annihilation in a confined nematic liquid crystal. *Mol. Cryst. Liq. Cryst.*, 413:2179–2187, 2004.

[38] M. Svetec, S. Kralj, Z. Bradac, and S. Zumer. Annihilation of nematic point defects: Pre-collision and post-collision evolution. *Eur. Phys. J. E*, 20:71–79, 2006.

[39] D. Sharma and A.D. Rey. Simulation of texture formation processes in carbonaceous mesophase fibres. *Liq. Cryst.*, 30(3):377–389, 2003.

[40] B.J. Edwards and A.N. Beris. Order parameter representation of spatial inhomogeneities in polymeric liquid-crystals. *J. Rheo.*, 33:1189–1193, 1989.

[41] L.M. Pismen and B.Y. Rubinstein. Motion of interacting point-defects in nematics. *Phys. Rev. Lett.*, 69(1):96–99, 1992.

[42] L. M. Pismen. *Vortices in Nonlinear Fields From Liquid Crystals to Superfluids, from Non-equilibrium Patterns to Cosmic Strings.* Clarendon Press, 1999.

[43] D. Walgraef. *Spatio-Temporal Pattern Formation.* Spinger-Verlag, 1997.

CHAPTER 7
Point and ring defects in nematics under capillary confinement

7.1 Summary

The textures exhibited by nematic liquid crystals confined to cylindrical capillaries under homeotropic anchoring have been studied for nearly thirty years. One of the reasons behind this maintained interest is that the processing of many high-performance fibers including carbon fibers and spider silks involve these textures. Three of these textures, the planar radial with line defect (PRLD), the planar polar with two line defects (PPLD) and the escape radial (ER) are relatively well understood. A third one, the escape radial with point defects (ERPD) presents however some unresolved issues and recent studies have questioned the real nature and dimensionality of the defects involved in this texture. It seems that the defects are not in the form of points but rather in the form of closed lines or rings. This paper presents a detailed study on the connection between point and ring defects in a cylindrical cavity using three-dimensional simulations based on the continuum Landau-de Gennes theory. The results show that *true* point defects cannot exist in cylindrical cavities and that the merging of two ring-like defects may lead to two qualitatively different stable textures; namely the ER and PPLD textures. The various results are in qualitative agreement with recent molecular dynamic studies and with theoretical predictions based on experimental observations. The predictions provide new

insights on the structural connections between synthetic and biological super-fibers.

7.2 Introduction

Nematic liquid crystals are intermediate phases combining liquid-like fluidity with solid-like orientational order forming in a wide variety of materials often comprised of rigid rod-like molecules. [1–3] The orientational order of these anisotropic fluids results from the spontaneous alignment of their constituent molecules along a common preferred direction called the *director* and described by a unit vector $\mathbf{n}$. As mesogenic molecules are generally apolar, the states $\mathbf{n}$ and $-\mathbf{n}$ are equivalent and therefore $\mathbf{n}$ should be thought of as a headless vector. The usefulness of nematic liquid crystals arises from the fact that their various physical properties (e.g. optical, rheological, mechanical) can be in principle tailored by adjusting their geometric, interfacial and external constraints (i.e. shape of the nematic container, molecular orientation imposed by its surface and possibly electric, magnetic or flow fields). The average preferred molecular orientation in these materials is therefore usually only local and varying from subregion to subregion forming orientational textures. [1–3] An important feature of orientational textures is that they often contain defects. Nematic defects usually corresponds to *regions* in the form of points (zero-dimensional) or lines (one-dimensional) where a director field $\mathbf{n}(\mathbf{r})$ cannot be uniquely defined. [3, 4] In addition to their dimensionality (point or line), nematic defects are also conventionally given a strength (M) whose magnitude (usually 1/2 or 1) and sign ($\pm$) denote respectively the amount and the sense of director rotation when encircling the defect. [3, 4] In this work we focus on the various textures and

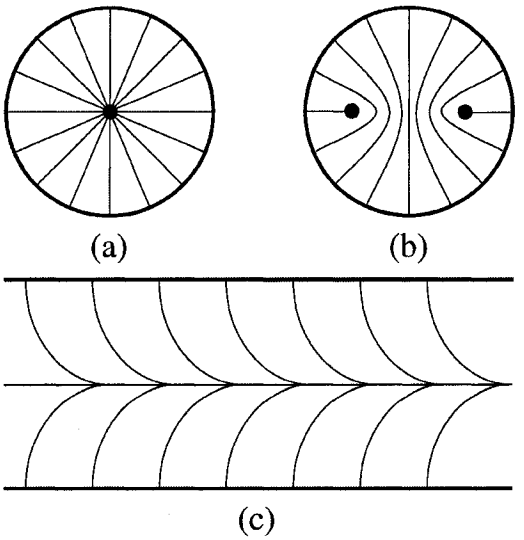

Figure 7–1: Typical textures found in nematic-filled cylindrical capillaries with sidewalls imposing a homeotropic anchoring. (a) Transversal view of the planar radial with a line defect texture (PRLD); (b) Transversal view of the planar polar with two line defects texture (PPLD); (c) Longitudinal view of the escape radial texture (ER). The (flux) lines are everywhere tangent to the director field $\mathbf{n}(\mathbf{r})$ while the black dots indicate the presence of line singularities perpendicular to the page.

defects exhibited by nematic mesophases confined in cylindrical cavities with sidewalls imposing a radial molecular orientation. The motivation behind the study of these textures and defects is their occurrence and importance in the manufacturing of many high-performance fibers (e.g. carbon fibers, nematic-filled carbon nanotubes and spider's silks) formed from nematic precursors. [5–14]

Nematic mesophases confined in cylindrical capillaries whose walls impose homeotropic anchoring basically display three different types of stable texture known as: (i) planar radial with line defect (PRLD), (ii) planar polar with line defects (PPLD) and (iii) escape radial (ER). [15–17] These three textures, which are pictured in figure 7–1,

are homogeneous along the cavity axis and therefore purely two-dimensional. Their stability depends on: (a) the radius of the capillary, (b) the nematic potential (A function of temperature for thermotropic nematic liquid crystals or concentration for lyotropic liquid crystals), and (c) the elastic properties of the particular nematic fluid considered. [18] The variations of elastic properties from one nematic mesophase to another essentially modify the (meta)stability limits/envelopes of the texture phase diagram. [19] Therefore, far from phase transitions that introduce pre-transitional elastic constant divergences, such as nematic-smectic A, [1] the essential qualitative features of the textures can be appropriately studied within the approximation of elastic isotropy. In addition, when the nematic potential is high enough and the material is far from the isotropic-nematic phase transition, the (meta)stability of the different textures is only dictated by the radius of the capillary.

In the PRLD texture (Fig. 7–1(a)), which arises in small capillaries or very close to the isotropic-nematic phase transition, the molecular orientation is everywhere radial and a line defect of strength $M = +1$ runs along the capillary axis. In larger capillaries or at higher nematic potential, the PRLD becomes unstable with respect to the PPLD texture. The PPLD texture (Fig. 7–1(b)) exhibits a broken rotational symmetry and is characterized by two line defects of strength $M = +1/2$ parallel to the cavity axis. In large capillaries, theoretical studies predict that the energetically favorable texture is the ER (Fig. 7–1(c)). Unlike the PRLD and PPLD, the ER is continuous and does not present any line singularity. The ER texture is similar to a PRLD texture, but which has avoided the central line defect by uniformly *escaping* in the third dimension. [20–22]

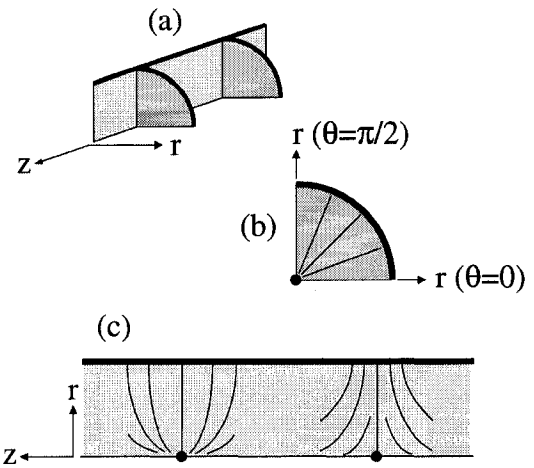

Figure 7–2: Schematic of the escape radial with point defects texture (ERPD). The flux lines are everywhere tangent to the director field $\mathbf{n}(\mathbf{r})$ while the black dots indicate the presence of point singularities on the axis of the cavity. (a) The different elementary cross sections given through the ERPD texture; (b) transversal cross section (identical for the radial and hyperbolic point defects); (c) longitudinal cross section. The point defect on the left is said to be radial while bearing the topological charge $M = +1$ and the one on the right is hyperbolic and has the charge $M = -1$.

Despite the fact that the stable texture in large nematic capillaries is theoretically the ER texture, in practice it is seldom observed. [17, 21–25] What is instead commonly detected is a three-dimensional texture consisting of a periodic distribution of point defects of alternating topological charge (i.e. $M = \pm 1$) known as escape radial with point defects (ERPD) (See Fig. (7–2)). [17, 21–25] The ERPD texture can be seen as a bidirectional ER texture consisting of partially escaped domains leading to the distribution of alternating radial ($M = +1$) and hyperbolic ($M = -1$) point defects. A noteworthy occurrence of the ERPD texture is found in the nematic dope flowing along the spinning apparatus of spiders. [8, 9] Although the role of this texture is unclear, it is believed to play an essential function in the extrusion process, possibly delaying crystallization of the nematic silk precursor in the spinning duct, but also optimizing its rheology (back-flow phenomenon [26]) and pre-aligning the molecules.

Although the ERPD texture (Fig. 7–2) has been known for about thirty years, [21,22,25] it is not yet completely understood. Its emergence is believed to be due to surface irregularity effects, fluctuations near the isotropic-to-nematic phase transition and possibly to impurities in the cavity. [15–17, 27] Experimental and theoretical works have shown that the ERPD texture is metastable because oppositely charged point defects may attract and annihilate each other leading to the more energetically favorable ER texture (cf. Fig. 7–1(c)). [15–17, 21, 22, 25, 27]

On the other hand, recent three-dimensional Brownian molecular dynamic studies on the ERPD texture have suggested that the defects found along the axis of cylindrical cavities may not be, in reality, in the form of points but rather in the

form of closed-lines or rings. [28–30] The splitting of point defects into ring defects in cylindrical cavities subjected to homeotropic anchoring has been verified in our previous contribution using three-dimensional Landau-de Gennes continuum simulations. [31] To avoid any confusions on the dimensionality of the singularity we therefore introduce the name escape radial with ring defects (ERRD) to designate the texture consisting of ring defects instead of point defects. The most probable orientation for ring singularities in cylindrical tubes is with their axis perpendicular to the cavity axis therefore breaking the cylindrical symmetry of the entire associated texture. A schematic of the described ERRD texture is given in Fig. (7–3).

This paper is a contribution to the on-going effort to understand nematic texture transformations in fiber-like geometries and in particular transformations between point, ring and line defects and their associated textures. In this work we first question the existence and the stability of isolated point defects confined to cylindrical capillaries and consequently of the ERPD texture. We then study the (meta)stability of ERRD texture and show the representative annihilation of two ring defects leading, in a continuous manner, to the well known ER and PPLD textures, depending on the radius of the capillaries. The paper is organized as follows: in section 7.3 we introduce the mathematical model employed, in section 7.4 we present the computational results and finally in section 7.5 we present conclusions.

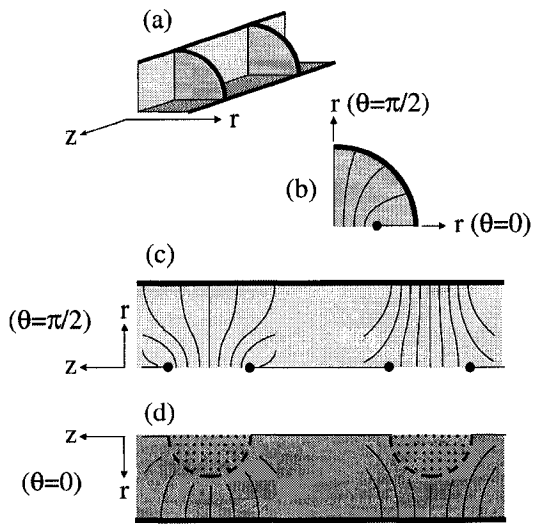

Figure 7–3: Schematic of the escape radial with ring defects texture (ERRD). The flux lines are everywhere tangent to the director field $\mathbf{n}(\mathbf{r})$. (a) The different cross sections taken through the ERRD texture; (b) the transversal cross section (identical for the radial and hyperbolic ring defects); (c) first longitudinal cross section (in (b) and (c) views, the big black dots indicate the passage of the ring singularity); (d) second longitudinal cross section (normal to the plane given in (c)) in which the dash lines correspond to the ring singularity. In (c) and (d), the defect on the left is the radial ring ($M = 1/2$) while the one on the right is the hyperbolic ring ($M = -1/2$).

7.3 Modeling

7.3.1 Computational domain

In order to study the ERRD texture and associated radial and hyperbolic ring defects we consider a three-dimensional cylindrical cavity of radius R and a total length up to $H = 8R$. In order to reduce the high cost of the three-dimensional calculations we do not consider the entire volume but rather a fourth of it and use the mirror symmetry properties of the envisioned solutions (cf. Fig. (7–3)).

7.3.2 Tensor order parameter Q_{ij}

The tensor order parameter $\mathbf{Q}$ is, unlike the director $\mathbf{n}$, everywhere continuous including in the core of defects. [32] It is symmetric traceless (*i.e.*, $Q_{ij} = Q_{ji}$ and $Q_{ii} = 0$) and therefore possesses five degrees of freedom. In terms of its eigensystem, it is represented as follows: [33]

$$Q_{ij} = \mu_n n_i n_j + \mu_m m_i m_j + \mu_l l_i l_j \tag{7.1}$$

$\mathbf{n}$, $\mathbf{m}$ and $\mathbf{l}$ are unit eigenvectors forming an orthogonal triad and μ_n, μ_m and μ_l are their corresponding eigenvalues. The eigenvalues μ_i $(i = 1, 2, 3)$ of the tensor order parameter are restricted by: $-1/3 \leq \mu_i \leq 2/3$ and $\mu_n + \mu_m + \mu_l = 0$. The director triad and the eigenvalues characterize the orientation and the strength of alignment of the phase respectively. The largest eigenvalue in magnitude, μ_n, gives the strength of ordering along the uniaxial director $\mathbf{n}$. [34, 35] μ_m and μ_l eigenvalues correspond to the biaxial directors $\mathbf{m}$ and $\mathbf{l}$ $(\mathbf{l} = \mathbf{n} \times \mathbf{m})$. At equilibrium, an undistorted nematic phase is uniaxial; however, at defect cores the phase is likely to exhibit biaxiality.

The ordering states that can describe $\mathbf{Q}$ are: isotropic ($\mu_1 = \mu_2 = \mu_3 = 0$; $\mathbf{Q} = 0$), positive uniaxial ($\mu_1 > \mu_2 = \mu_3$), negative uniaxial ($\mu_1 = \mu_2 > \mu_3$) and biaxial ($\mu_n \neq \mu_m \neq \mu_l$). [33, 36]

When the tensor order parameter $\mathbf{Q}$ is uniaxial, it is useful to represent it as:

$$Q_{ij} = S(n_i n_j - \frac{I_{ij}}{3}) \tag{7.2}$$

S ($-1/2 \leq S \leq 1$) is referred to as the uniaxial scalar order parameter and characterizes the degree of alignment around the $\mathbf{n}$. $\mathbf{I}$ stands for the standard unit tensor.

Biaxiality plays an important role in the type of solutions we compute in this work and a convenient parameter to represent it is the degree of biaxiality defined as: [33]

$$\beta^2 = 1 - 6\frac{(\mathrm{tr}\mathbf{Q}^3)^2}{(\mathrm{tr}\mathbf{Q}^2)^3} \tag{7.3}$$

which takes values in the interval $[0, 1]$. In positive and negative uniaxial states $\beta^2 = 0$, while maximum biaxiality states correspond to $\beta^2 = 1$.

7.3.3 Landau de-Gennes free energy

The total free energy of a nematic liquid crystal system under strong anchoring conditions (*i.e.*, when the molecular order at the boundary is fixed) is written as: [1]

$$F = \int_V f_b dr^3 = \int_V (f_h + f_g) dr^3 \tag{7.4}$$

In this expression, f_b, f_h and f_g represent the total bulk, homogeneous bulk and gradient bulk free energy densities, respectively. The homogeneous free energy describes

the short-range ordering effects related to the amplitude of the tensor order parameter. This expression can describe the first order isotropic-nematic phase transition but also, and more importantly in our work, the variations of the nematic ordering in the vicinity of defects. This contribution is often referred as the Landau-de Gennes free energy. According to Doi's formalism [18, 37, 38], this expansion of the order parameter may be written as:

$$f_h = \frac{A}{2}(1 - \frac{U}{3})Q_{ij}Q_{ji} - \frac{AU}{3}Q_{ij}Q_{jk}Q_{ki} + \frac{AU}{4}(Q_{ij}Q_{ji})^2 \tag{7.5}$$

In this expression A is an energy density scale (unit of energy per cubic meter), U is a dimensionless phenomenological parameter called nematic potential which controls the magnitude of the equilibrium tensor order parameter. In general the nematic potential U can be assigned a dependence on either temperature or concentration depending on the nature of the nematic liquid crystal considered (*i.e.*, thermotropic or lyotropic). In our study U is taken to be proportional to concentration and according to Doi's theory, $U = 3C/C^*$ where C and C^* are the number and critical number density of rod-like molecules, respectively. [18, 37] Accordingly, the energy density scale $A = C^*kT$ where k and T are the Boltzmann constant and the temperature of the system, respectively.

At equilibrium and away from distorted regions, the tensor order parameter $\mathbf{Q}$ given by Eq. (7.5) is uniaxial. Under these conditions, the value of the scalar order parameter is given by the relation:

$$S_e = \frac{1}{4} + \frac{3}{4}\sqrt{1 - \frac{8}{3U}} \tag{7.6}$$

Within this framework, the first order phase isotropic-nematic phase transition occurs at nematic potential $U_{IN} = 2.7$. Also, in this model, the system is isotropic for $U < U_{IN}$ and nematic for $U > U_{IN}$. The limit of metastability for the isotropic and nematic phase are $U^* = 3$ and $U^{**} = 8/3$, respectively. [18,37]

The gradient f_g contribution in Eq. (7.4), represents the energy density penalty associated with the long-range variations of the tensor order parameter $\mathbf{Q}$ in the nematic phase. As mentioned in the introduction, the elastic anisotropy of nematic essentially modifies the limits/envelopes defining the domain of (meta)stability of the different defect configurations but not their qualitative features. Since exploring the entire parametric space is beyond the scope of this paper we therefore consider the case of elastic isotropy. In the one constant approximation, the gradient energy expressed in terms of $\mathbf{Q}$ reads: [37,39]

$$f_g = \frac{L}{2}\nabla_k Q_{ij}\nabla_k Q_{ij} \tag{7.7}$$

In this expression, L is a material-dependent elastic constant (unit of energy per unit length).

7.3.4 Governing nemato-dynamic equation

The dynamic equation describing the relaxation of the tensor order parameter $\mathbf{Q}(\mathbf{r}, t)$ toward an equilibrium value that minimizes the total free energy under the different constraints (shape and size of the container, anchoring at its surface, etc.)

follows from variational principles and is given by: [37, 39–42]

$$\gamma \frac{\partial Q_{\alpha\beta}}{\partial t} = -\frac{\delta F}{\delta Q_{\alpha\beta}} \tag{7.8}$$

In this equation γ is a constant kinematic coefficient related to rotational viscosity. [37, 39] The right-hand side of Eq. (7.8) corresponds to the functional derivative of the total free energy. From variational calculus it can be shown that:

$$\frac{\delta F}{\delta Q_{\alpha\beta}} = \frac{\partial f_b}{\partial Q_{\alpha\beta}} - \nabla_\sigma \frac{\partial f_b}{\partial \nabla_\sigma Q_{\alpha\beta}} \tag{7.9}$$

Only the symmetric traceless part of this expression is retained in the calculations in order to satisfy the constraints of the tensor order parameter.

7.3.5 Dimensionless quantities and auxiliary conditions

In order to reduce the number of parameters, facilitate the analysis, and to compare with other studies, all the calculations reported here are presented in dimensionless format. Using the energy scale A, we define the dimensionless bulk free energy density $\bar{f}_b = f_b/A$ where the over-bar indicates the dimensionless quantity. The dimensionless position vector is defined as $\bar{\mathbf{r}} = \mathbf{r}/R$ where R stands for the radius of the cylindrical cavity. Accordingly, we define the dimensionless *nabla* operator $\bar{\nabla} = R\nabla$ and dimensionless total energy $\bar{F} = \frac{F}{AR^3}$. The fixed, reference length scale in the problem is the nematic coherence length defined as $\xi = \sqrt{L/A}$. This length gives a characteristic scale for the amplitude variations of the tensor order

parameter and the size of defect cores. The ratio R/ξ, corresponding to the dimensionless nematic coherence length reciprocal, therefore represents the relative size of the cavity.

The boundary conditions are as follows: at the curved surface representing the wall of the cavity, the tensor order parameter is assumed to be uniaxial and to describe a rigid radial anchoring condition so that $Q_{ij}(r = R) = S_e(e_i^r e_j^r - \frac{\delta_{ij}}{3})$, where $\mathbf{e^r}$ is the unit vector along the radial direction. On the two mutually perpendicular interior surfaces, boundary conditions ensure mirror symmetries. Finally at both ends of the tube a *no flux* condition ($e_\gamma^z \frac{\partial f_b}{\partial \nabla_\gamma Q_{\alpha\beta}} = 0$, where e_γ^z is the unit normal to the cavity caps) is used to emulate an infinitely long cavity.

In dimensionless format, the model contains two parameters: the nematic potential U and the reduced cavity size R/ξ. Exploring the entire parametric space is beyond the scope of this paper and is left for future work. For all the simulation results presented in the next section, the nematic potential is set to $U = 6$ which corresponds to a deep nematic phase with an equilibrium scalar order parameter of $S_e = 0.809$. In this contribution we analyze solutions for different cavity sizes R/ξ.

7.3.6 Computational procedure and post-processing tools

The governing partial differential equation for the tensor order parameter $\mathbf{Q}(\mathbf{r})$, Eq. (7.8) is solved using a standard time integration scheme. The space discretization is achieved using the Galerkin finite element method. The density of triangular element is higher in the regions describing steep changes in the tensor order parameter

amplitude. In those delicate regions, the size of the triangular elements is always smaller than the ratio ξ/R which corresponds to the smallest length of the problem.

The order parameter fields $\mathbf{Q}(\mathbf{r})$ are visualized by means of cuboids built from the eigensystem of the tensor. [32] The axes of the cuboids are aligned with the eigenvectors while the size of each side is proportional to the eigenvalues. Given that the eigenvalues of $\mathbf{Q}(\mathbf{r})$ can be negative, we use the shifted tensor $\mathbf{M} = \mathbf{Q} + \mathbf{I}/3$ for the purpose of cuboid visualization. [36] Using this technique, it is possible to distinguish between isotropic (all edges of the cuboid equal), uniaxial (two edges equal) and biaxial (all three edges different) states.

7.4 Results and discussions

7.4.1 Stability and existence of ring defects versus point defects in cylindrical cavities

In order to develop a better understanding of the ERRD texture (cf. Fig. (7–3)) and its connections with other fiber textures (cf. Fig. (7–1)), this section provides a study on the fine structure of isolated ring defects confined in cylindrical cavities, their stability and existence.

Ring defects that have broadened out of cylindrically-confined point defects are most probably oriented with their axis perpendicular to the cavity axis. [28–31] Despite that this orientation of the ring defects might appear to be counter-intuitive since this breaks the overall cylindrical symmetry of the orientational order, it is most likely because it provides to the defect an infinite possiblility of orientations along the radial direction.

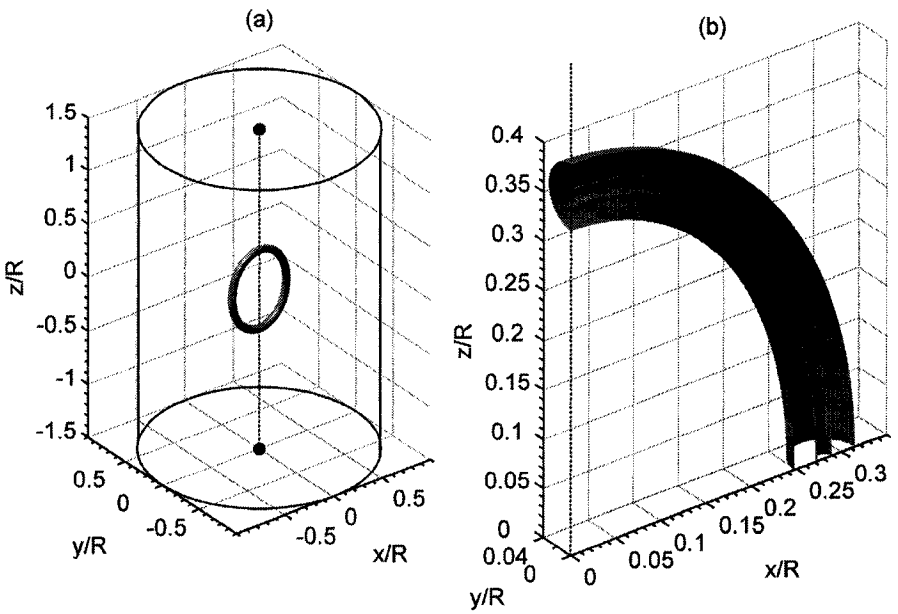

Figure 7–4: (a) Equilibrium R-ring defect in a cylindrical capillary subjected to homeotropic anchoring for the parameters $U = 6$ and $R/\xi = 22$. (b) Enlarged view of the elementary cross-section cut through the defect. The surfaces in (a) and (b) correspond to the iso-level 0.5 of the biaxial parameter β^2.

Given their inherent biaxial structure, line defects and consequently ring defects are conveniently visualized in terms of the biaxial parameter β^2 defined in Eq. (7.3). Figure (7–4) shows an iso-surface plot of a typical ring defect oriented with its axis perpendicular to the cavity axis which has spontaneously emerged out of an initially enforced point defect with an isotropic core using the iso-level $\beta^2 = 0.5$. When considering a nematic material with elastic isotropy, as we do in this work, the geometry as well as the variations of ordering (i.e. the eigenvalues of the **Q**-tensor) are identical in the hyperbolic and radial ring defects; the only difference is in the director fields ($\mathbf{n}(\mathbf{r})$). [31]

Figure (7–5) provides the variations of the **Q**-tensor order parameter eigenvalues. One can see that a ring defect is characterized by a negative uniaxial ring surrounded by a biaxial torus with maximum biaxiality. Away from the torus, the ordering is positive uniaxial as prescribed by the boundary conditions. This result is in qualitative agreement with those obtain in previous two-dimensional analytical studies considering ring defects co-linearly orientated with the cylindrical cavity axis. [33,36,43] Careful examination of the β^2 profiles and in particular the separating distance between the peaks along the x and z directions reveals that the cross-section of the torus is perfectly circular; we identified in our previous work that the radius of the cross-section is however decreasing as the size of the capillary increases. [31] It is also interesting to note that, for the size of capillary considered, the ring defect is not circular but, in fact, wider in the z-direction.

In order to assess the stability of the ring defect we look at the variation of its geometry as a function of the confinement. To do so, we define the ring radii δ_z and

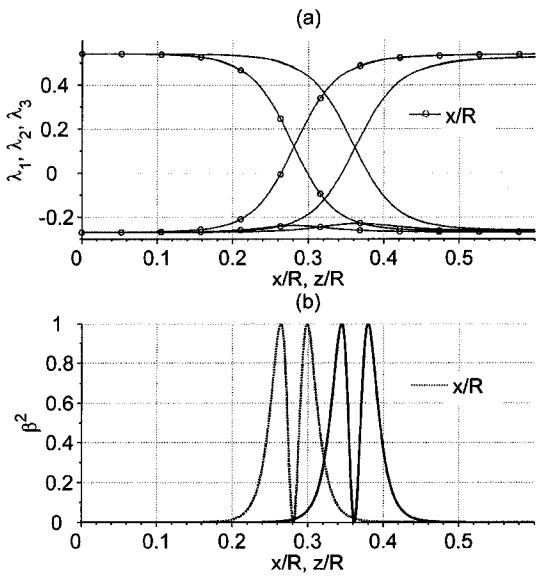

Figure 7–5: (a) Eigenvalues of the tensor order parameter $\mathbf{Q}$ along the x and z-directions for the same parametric conditions as in Fig. (7–4). (b) Corresponding variations of the biaxial parameter β^2.

δ_r corresponding to the distance from the center of the biaxial torus to the negative uniaxial ring along the axial and radial direction, respectively. Figure (7–6) shows the evolution of the ring radii as a function of the cavity radius (the coherence length ξ is a fixed length). What can be seen first is that for large cavities (small ξ/R), the ring defect is essentially circular ($\delta_z = \delta_r = \delta$). One can also observe that the evolution of this (unique) ring radius δ follows the linear relation $\delta/R \approx 4.083\ \xi/R$. This results suggest that *point* defects, corresponding to $\delta = 0$ can only be obtained in the case of infinite cavity radius (i.e. in absence of confinement). Figure (7–6) also shows that as the radius of the cavity shrinks (as ξ/R increases), the ring defect widens more in the axial direction than in the radial direction. This is understandable since whereas in the radial direction the ring is restricted by the cavity walls, it is not restricted by anything in the axial direction. Finally, we found that as the cavity radius continues to diminish, the radii of the ring defect diverge. The critical cavity radius at which the ring defect becomes unstable against transformation into the PPLD texture was evaluated to $R_c/\xi \approx 21.5$. On the other hand the smallest ring was computed for a cavity radius $R/\xi = 500$. In each simulation, adaptive mesh refinement was set so as to smoothly capture the gradients of the tensor order parameter. In the core of the defect, the size of the triangular elements is always smaller than the dimensionless coherence length ξ/R. In addition, each simulation started with an isotropic point defect.

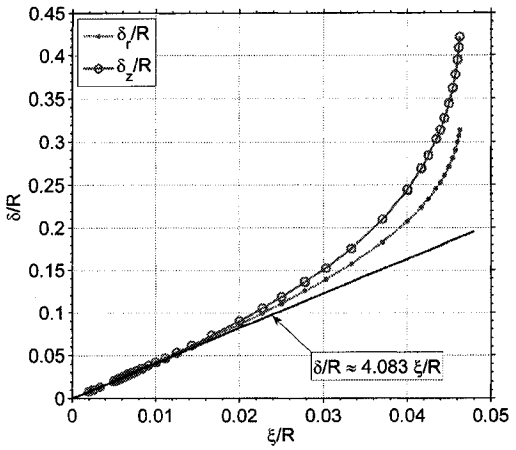

Figure 7–6: Evolution of the radii of an isolated ring defect confined into a cylindrical capillary with homeotropic anchoring as a function of the cavity radius.

7.4.2 Annihilation of a pair of ring defects in a cylindrical cavity

We now consider the interaction between two ring defects of opposite types (i.e. radial and hyperbolic) and examine, in detail, the topological transformations occurring in the course of the annihilation process. Three different stages can be identified during the annihilation process of two antagonist defects: (i) the pre-collision, (ii) the collision and (iii) the post-collision. [31] Two qualitatively different post-collision scenarios are found in the simulations: in the first one the annihilation of the two ring defects leads to the ER texture while in the second one it leads to the PPLD texture. The ERRD to ER transformation is illustrated for a cavity of radius $R/\xi = 25$ while the ERRD to PPLD is shown for the case $R/\xi = 22.5$. In both situations, the computational procedure employed is as follows: first we enforced two point defects with isotropic cores separated by a distance $d > 2R$ so that the system is in the early pre-collision regime. Then we take a couple of time steps until the points

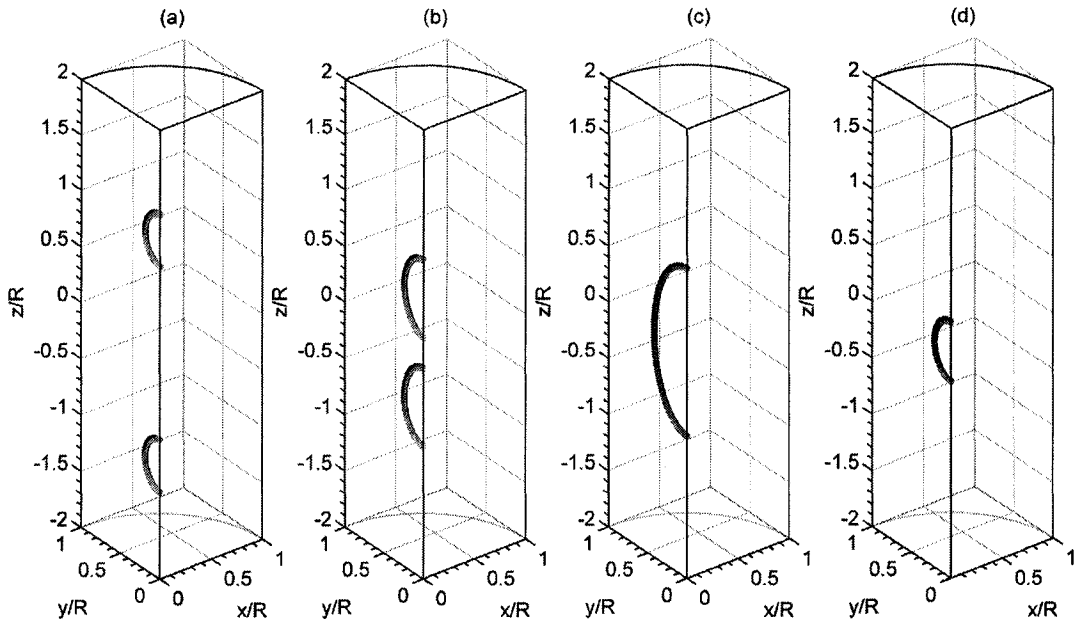

Figure 7–7: Topological transformations between two interacting ring defects confined into a cylindrical capillary of radius $R/\xi = 25$ leading to the ER texture. (a)-(b) (late) pre-collision regime; (c) end of collision regime and (d) post-collision regime. Surfaces are given by the iso-levels $\beta^2 = 0.5$. Frames (a), (b), (c) and (d) correspond respectively to dimensionless time 0, 5500, 5700 and 6350, respectively.

broaden into rings with quasi-stable radii (i.e. *quasi-stable* because despite that the rings' mutual interaction is fairly weak in the early pre-collision regime, it still exists and ring radii are therefore affected, even if infinitesimally). We consider time *zero* to be the instant when the two ring defects that have spontaneously emerged out of the isotropic point defects are separated by a distance $d_0 = 2R$ (i.e. the late pre-collision regime). The separating distance between the ring d is measured from the center/axis of each ring defect.

ERRD to ER transformation. Figure (7–7) illustrates the annihilation process between two ring defects in a cavity of size $R/\xi = 25$ leading to the ER texture. In this figure the ring defects are represented by means of the biaxial parameter β^2 for an iso-level of 0.5. Figure 7–7(a) shows the ring defects at time zero when they are separated by a distance $d_0 = 2R$ and are therefore entering the late pre-collision regime. In Fig. 7–7(b), which corresponds to dimensionless time 5500, the two ring defects are in the late pre-collision regime; due to their mutual interactions, they have enlarged in both the axial and radial directions. Figure 7–7(c) corresponds to time 5700 and the end of the collision regime when the two rings have collided and merged so as to form a new single defect. This new defect is a *chargeless* ring defect whose longitudinal radius corresponds to the sum of the individual ring defects' axial radii. The collision regime occurs over a very short period of time as compared as to the pre-collision stage. Finally Fig. 7–7(d) illustrates the post-collision regime with the configuration of the chargeless ring defect at dimensionless time 6350. At that stage, the chargeless ring has considerably shrunk and is on the verge of disappearing to leave behind a strictly uniaxial ER texture.

In order to get a better sense of the overall ordering in the cavity and in particular of the average molecular orientation, figure 7–8 provides three different cross sections (as given in Fig. 7–3) through the tensor order parameter field $\mathbf{Q}(\mathbf{r})$ at time zero and corresponding to the frame given in Fig. 7–7(a). The two types of ring defects: radial and hyperbolic can be clearly identified at positions $z/R = 1$ and $z/R = -1$, respectively. Biaxial ordering in the vicinity of the ring defects is detected by the distinctive shape of the cuboids (cf. Fig. 7–8(a)). Note the continuous variations of

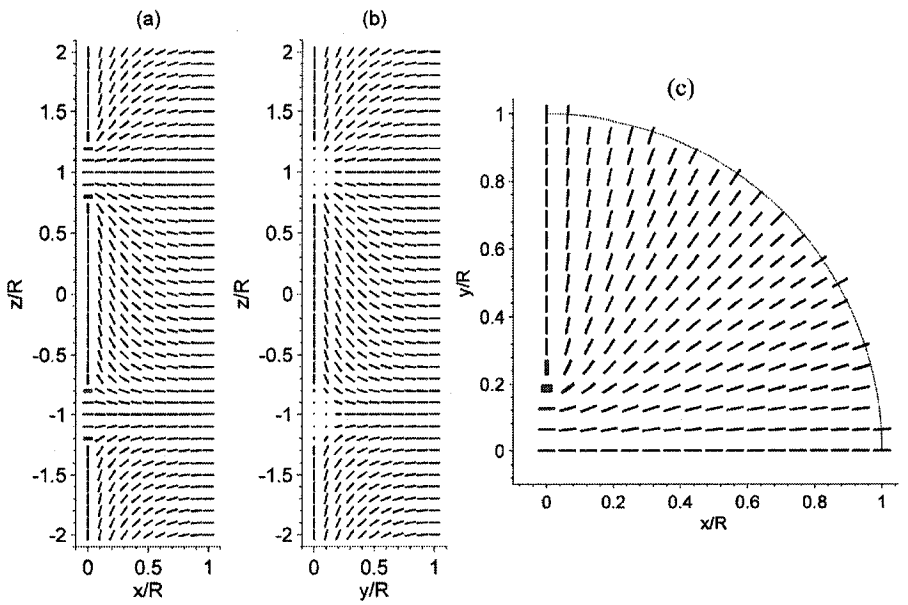

Figure 7–8: Different cross sections through the tensor order parameter field $\mathbf{Q}(\mathbf{r})$ corresponding to the frame shown in Fig. 7–7(a). The radial and hyperbolic ring defects are located at $z/R = 1$ and $z/R = -1$, respectively. Frames (a) and (b) correspond to the planes parallel and normal to the axis of the ring defects. Frame (c) corresponds to the transversal cross-section through the ring defect at $z/R = \pm 1$.

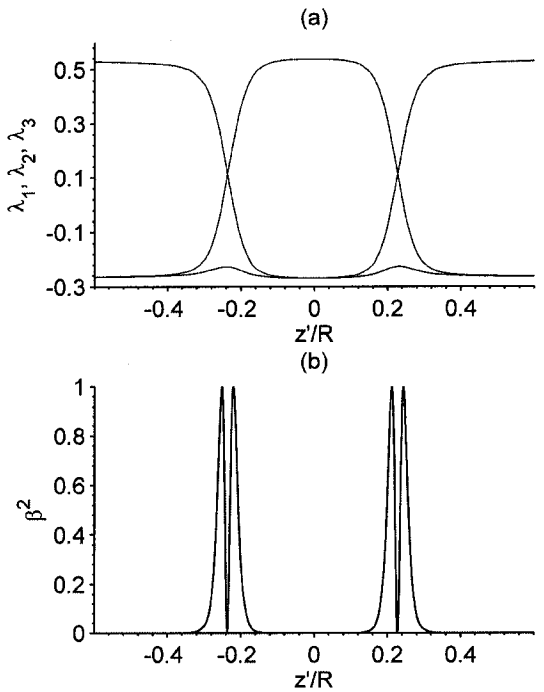

Figure 7–9: Variations of the tensor order parameter eigenvalues (a) and corresponding biaxial parameter β^2 (b) along the axial direction at time zero. The shifted coordinate z'/R is centered on the ring defect at $z/R = \pm 1$.

the tensor order parameter $\mathbf{Q}(\mathbf{r})$ throughout the defects. To complete this picture of ordering in the nematic cavity, Fig. 7–8(c) presents the transversal cross sectional view that is observed at $z/R = \pm 1$. The ordering in this cross-section is similar to the one found in the PPLD texture (cf. Fig. 7–1(b)); however the orientation transition along the y-direction at $x = 0$, which corresponds to the passage of the ring, does not occur at distance $0.666R$ as in the case of the PPLD texture but closer to the origin. [44, 45]

To complement the representation of ordering through cuboids, figure 7–9 gives the evolution of ordering along the axis of the cavity at time zero. Figures 7–9(a)

and 7–9(b) respectively provide the variations of the order parameter **Q** eigenvalues and biaxial parameter β^2 as a function of the shifted coordinate z'/R centered on the ring defects. The profiles are in agreement with the one given in Fig. 7–5 for an isolated ring defect in a nematic-filled cylindrical cavity. One can verify that the radius of the ring defects along the axial direction is $\delta_z/R \approx 0.24$. This shows that for separation distances d equal to or greater than a capillary diameter, the loop defects are essentially unaffected by each other.

Figure 7–10 shows the chargeless ring ordering in the late post-collision regime after it has significantly shrank. The molecular orientation away from the ring resembles that of the ER texture with the cuboids escaping toward a single direction. The orientation transition leading to the localized biaxiality of the defect is identified by the characteristic shape of the cuboids along the cavity axis. Figures 7–10(a) and 7–10(b) provide two mutually orthogonal cross-sections through the tensor order parameter field. Figure 7–10(c) corresponds to the complementary transversal cross-section in the plane perpendicular to the cavity axis at $z/R = 0$. This transversal cross-section resembles the PPLD texture given in Figs. 7–1(b) as well as the cross section of the individual $M = \pm 1$ ring defects (cf. Fig. 7–8(c)). The essential difference however is that in the case of the chargeless ring defect given in Fig. 7–10(c), the director is flipping out of the plane.

Figure 7–11 illustrates the variations of the **Q**-tensor eigenvalues and biaxial parameter β^2 in the chargeless ring defect along the cavity axis (The profiles correspond to dimensionless time 6350). The eigenvalues are, as in the case of the *charged* ring defects, exhibiting the typical eigenvalue exchange seen in line defects. As previously

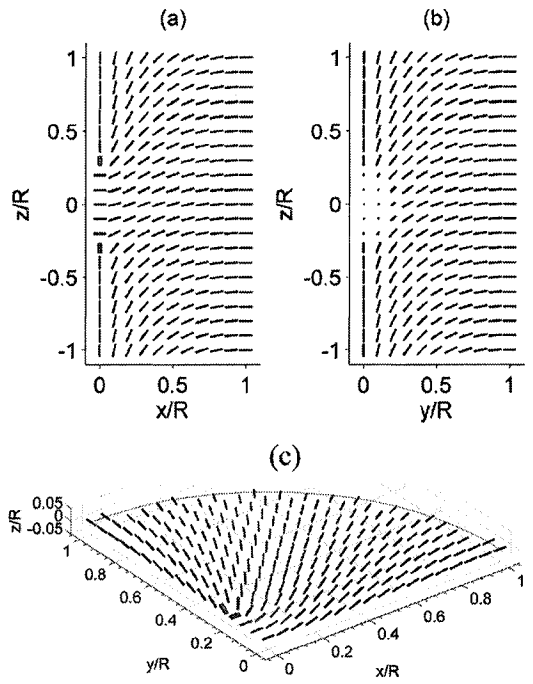

Figure 7–10: Cross section through the tensor order parameter field $\mathbf{Q}$ at dimensionless time 6350 (cf. Fig. 7–7(d)) showing the ordering in the *chargeless* ring formed after the collision and merging of two oppositely charged ring defects. (a) and (b) correspond to two mutually orthogonal longitudinal cross-sections through the defect while (c) gives the transversal cut at $z/R = 0$. The field of cuboids show the mixed escape-planar polar-like nature of the chargeless ring formed at the end of the collision regime.

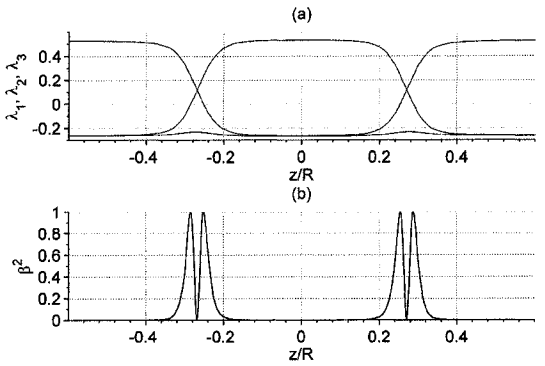

Figure 7–11: Variations of the tensor order parameter eigenvalues (a) and corresponding biaxial parameter β^2 (b) along the axial direction in the chargeless ring during the post-collision regime.

mentioned this exchange corresponds to a change of average preferred molecular orientation within the defect. The chargeless ring also consists of a negative uniaxial loop enclosed in a biaxial torus.

Finally Fig. 7–12 is a longitudinal cross section through the tensor order parameter field showing the computed defect-free ER texture (cf. Fig. 7–1(c)) that remains once the chargeless ring defect has shrank and disappeared. The ER texture, which characterizes the end of the post-collision regime in this first scenario, is cylindrically symmetric and strictly uniaxial.

ERRD to PPLD transformation. Figure (7–13) illustrates the process of annihilation of two ring defects in a cylindrical cavity of size $R/\xi = 22.5$ leading to the PPLD texture in the late post-collision regime. As in previous cases, the ring defects are represented by iso-surfaces of the biaxial parameter β^2 for an iso-value of 0.5. Figure 7–13(a) shows the ring defects at time zero when they are separated by a distance $d_0 = 2R$ and are hence in the late pre-collision regime. At this time,

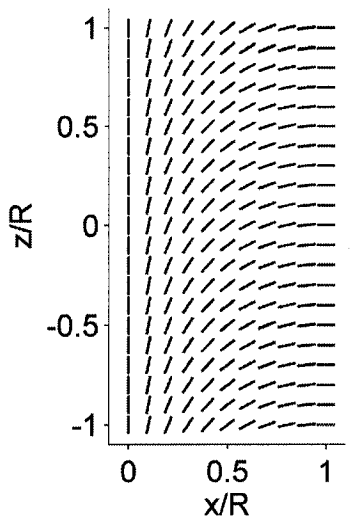

Figure 7–12: Longitudinal cross section through the tensor order parameter field represented in terms of cuboids and showing the defect-free ER texture that results from the total shrinkage of the chargeless ring defect at the end of the post-collision regime.

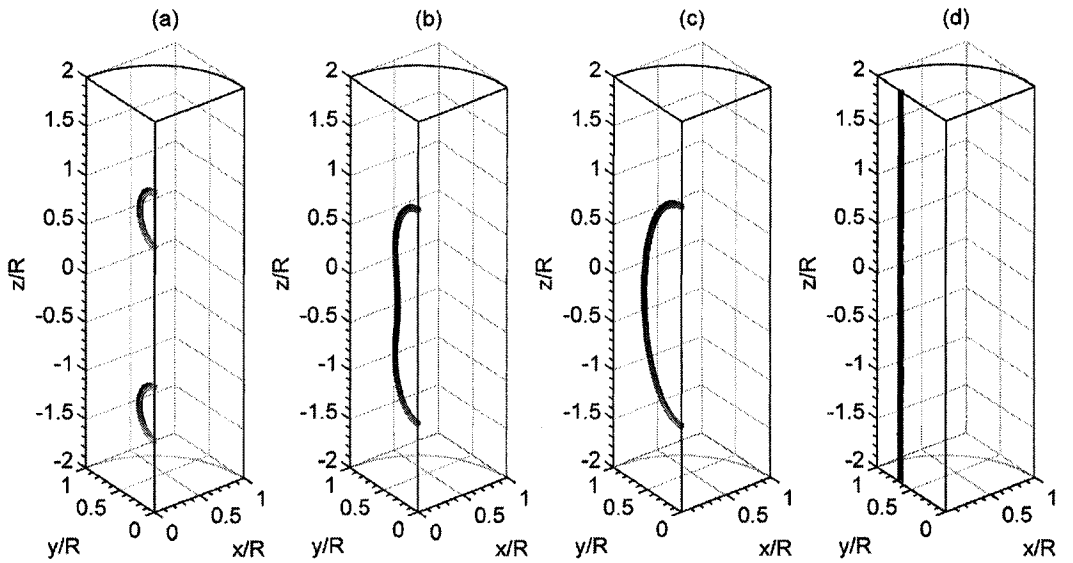

Figure 7–13: Topological transformations between two interacting ring defects confined into a cylindrical capillary of radius $R/\xi = 22.5$ leading to the PPLD texture. (a) corresponds to time zero and the late pre-collision regime. (b) shows the configuration in the early collision regime at dimensionless time 2800. The end of the collision regime in which a unique chargeless ring remains is given in (c) for time 3150. Finally, (d) occurs at dimensionless time 11450; the chargeless ring defect has expanded to give the PPLD texture (at least locally). Surfaces are given by the iso-levels $\beta^2 = 0.5$.

the rings are essentially circular and their geometry follows closely the one of the isolated rings (cf. Fig. 7–6). Fig. 7–13(b), shows the premise of the chargeless ring at dimensionless time 2800 in the early collision stage. At this point there is only one ring (with respect to the iso-surface of β^2) but one can still distinguish the two centers/cores of the old charged ring defects on both sides of the cavity midway. Figure 7–13(c) corresponds to time 3150 and the end of the collision regime when the chargeless ring has resumed formation. The chargeless ring is in this case larger that the one formed in the cavity of size $R/\xi = 25$ (cf. Fig. 7–7(c)). In fact, the size of the chargeless ring formed at the end of the collision regime and particularly its transversal radius seems to dictate whether there is going to be shrinkage or growth of the loop and therefore creation of the ER or PPLD texture, respectively. [30] The precise cavity critical radius at which the system goes from a shrinking (and vanishing) to a growing (and opening) chargeless defect has not been determined precisely yet but will be in our future work. At the present we know that the transition is within the narrow range $22.55 < R/\xi < 25$. Finally Fig. 7–13(d) illustrates the end of the post-collision regime at dimensionless time 11450 when the chargeless ring has opened to form the PPLD texture. It is important to note that, in the post-collision regime, the chargeless ring grows faster in the longitudinal direction then in the radial direction. The growth of the ring is however bounded in the radial direction as it stops once the PPLD critical radius of 0.666 is reached while in the longitudinal direction, the growth does not present any limit except at the end caps of the cavity. In a very long capillary, the PPLD texture can therefore be local

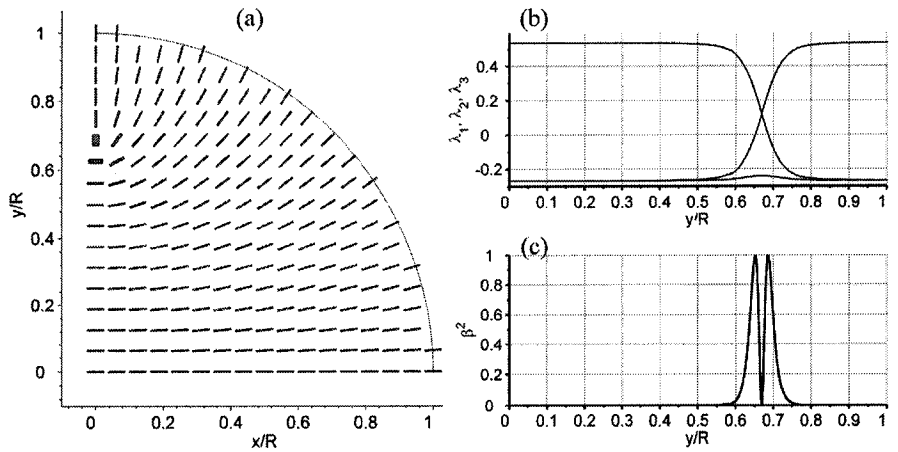

Figure 7–14: (a) Transversal cross section through the tensor order parameter field showing the PPLD texture that occurs when the chargeless ring defect opens at the end of the post-collision regime. (b) and (c) are the corresponding variations of the tensor order parameter eigenvalues and biaxial parameter β^2 along the radial direction.

and the time required to reach the equilibrium PPLD texture from the chargeless ring varies with the length of the cavity.

Figure 7–14(a) provides a transversal cross section through the tensor order parameter field at time 11450 when the cavity exhibits the PPLD texture (cf. Fig 7–1(b)). The field of cuboids resembles that of the chargeless ring defect given in Fig. 7–8(c); the essential difference is that now the line defects running parallel to the cavity axis are separated by a fixed distance of $\approx 1.333R$. Finally Figs. 7–14(b) and 7–14(c) indicate the variation of the tensor order parameter eigenvalues and the corresponding biaxial parameter β^2.

7.5 Summary and conclusions

We have investigated nematic ring defects occurring in cylindrical cavities with sidewalls imposing homeotropic anchoring (i.e. molecular orientation at the walls is radial) using three-dimensional Landau-de Gennes continuum type simulations. We have shown that ring defects, spontaneously emerging out of initially enforced isotropic point defects, most likely orient their axis perpendicular to the cavity axis. [31] The results agree with recent Brownian molecular dynamic simulations. [28–30]. It is also demonstrated that the size of the rings decreases as the radius of the cylindrical cavity increases. Isolated ring defects (i.e. rings separated by a distance greater than a cavity diameter from any other rings) are found to be stable in cavities of radius greater than 21.5ξ. In small cavities (radius between $21.5\xi - 50\xi$), the radius of the ring defects is found to be wider in the axial direction than in the radial direction. In large cavities (radius greater than 100ξ), the ring defects are perfectly circular and therefore characterized by a unique radius. In addition, our results indicate that in the large cavity regime, the radius of the ring defects adopt a finite value: $\delta \approx 4.083\ \xi$ (i.e. the radius of the ring is roughly four times the nematic coherence length). This suggests that *true* point defects cannot exist in cylindrical cavities as they are unstable and always split into loops. The reason why these ring defects are not necessarily detected in experiments is their nanometer length scale, i.e. at the order of magnitude of the nematic coherence length. Also, away from the defect core, molecular orientation is qualitatively identical in loops and points. Similar to point defects, both radial and hyperbolic ring-like defects exist. In the case of elastic isotropy, the degree of ordering (β^2) varies the same way in both defects

and only their director fields differ. Finally, the cross section of the biaxial torus surrounding the negative uniaxial ring is found to be always perfectly circular but decreasing as the cavity radius increases.

In addition to isolated ring defects, we have investigated the details of the annihilation process between two oppositely charged ring defects. We have denoted the texture formed by a periodic distribution of ring defects: escape radial with ring defects or ERRD texture. Similar to the ERPD texture, the ERRD is metastable with oppositely charged rings that, like points, attract and eventually annihilate each other. We have shown that the annihilation process of a representative ring pair may lead to two qualitatively different textures depending on the size of the cavity radius: the ER texture (as we would have expected from a metastable ERPD texture) and the PPLD texture. The latter texture cannot be nucleated from an ERPD texture as it lacks the necessary dimensionality (i.e. that of a line defect). A crucial intermediate step in the formation of the ER or PPLD textures is the merging of two oppositely charged rings into a single *chargeless* ring. Structural elements of both the ER and PPLD textures have been identified in the chargeless ring defect. The structure of the radial, hyperbolic and chargeless ring defects agree very well with the theoretical predictions made by Melzer and Nabarro based on their experimental observations. [25] Depending on its size and particularly its radius along the radial direction, the chargeless ring either shrinks until it disappears thereby producing the ER texture or expands until it opens thereby giving the PPLD texture. The precise threshold in the chargeless ring radius leading to either one of the textures has not been determined precisely but is known to occur when the cavity radius is

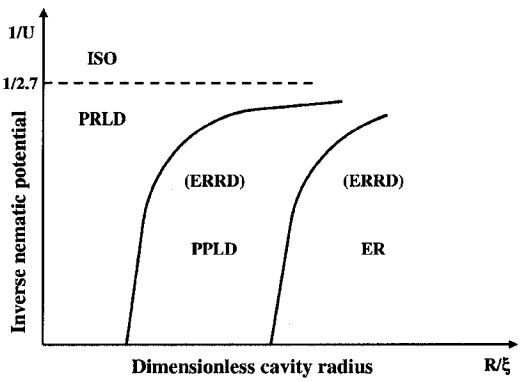

Figure 7–15: Schematic phase diagram of the nematic textures found in cylindrical cavities with sidewalls imposing homeotropic anchoring. The textures indicated in parentheses are metastable.

in the range $22.55\xi < R < 25\xi$. Figure 7–15 provides a schematic phase diagram summarizing the different textures that can be observed in a cylindrical cavity with sidewalls imposing radial anchoring.

The new results presented in this contribution should enrich the general understanding of nematic textures in cylindrical capillaries. These results should also be useful in the comprehension of textures in new advanced nematic based fibers such as nematic-filled carbon nanotubes [7] and in nematic colloids [46–48] in which ring and point defects are prevalent.

REFERENCES

[1] P.G. de Gennes and J. Prost. *The Physics of Liquid Crystals.* Oxford University Press, 1995.

[2] P.J. Collings. *Liquid Crystals: Nature's Delicate Phase of Matter.* Princeton University Press, 2001.

[3] M. Kleman and O.D. Lavrentovich. *Soft Matter Physics: An Introduction.* Springer, 2002.

[4] P. Oswald and P. Pieranski. *Nematic and cholesteric liquid crystals : concepts and physical properties illustrated by experiments.* CRC Press, 2005.

[5] L.H. Peebles. *Carbon Fibers - Formation, Structure, and Properties.* CRC, Boca Raton, 1995.

[6] J.E. Zimmer and J.L. White. *Advance in liquid crystals*, volume 5. New York: Academic Press, 1982.

[7] K. Jian, R.H. Hurt, B.W. Sheldon, and G.P. Crawford. *Appl. Phys. Lett.*, 88:163110, 2006.

[8] F. Vollrath and D.P. Knight. *Nature*, 410:541–548, 2001.

[9] J.E. Lydon. *Liq. Cryst. Tod.*, 13(3):1–13, 2004.

[10] J. Turner and C. Karatzas. *Natural Fibers, Plastics and Composites*, chapter 1, Advanced spider silk fibers by biomimicry, pages 11–23. Kluwer Academic Publishers, 2004.

[11] A.D. Rey. *Phys. Rev. E*, 51:6278–6281, 1995.

[12] L. Wang and A.D. Rey. *Modell. Simul. Mater. Sci. Eng.*, 5(1):67–77, 1997.

[13] L. Wang and A.D. Rey. *Liq. Cryst.*, 23:93–111, 1997.

[14] A.D. Rey. *Modell. Simul. Mater. Sci. Eng.*, 8:803–813, 2000.

[15] S. Kralj and S. Zumer. *Phys. Rev. E*, 51(1):366–379, 1995.

[16] G.P. Crawford, D.W. Allender, and J.W. Doane. *Phys. Rev. A*, 45(12):8693–8708, 1992.

[17] I. Vilfan, M. Vilfan, and S. Zumer. *Phys. Rev. A*, 43(12):6875–6880, 1991.

[18] M. Doi. *The Theory of Polymer Dynamics.* Oxford University Press, 1998.

[19] S. Mkaddem and E.C. Gartland. *Phys. Rev. E*, 62(5):6694–6705, 2000.

[20] R.B. Meyer. *Philos. Mag.*, 27(2):405–424, 1973.

[21] C. Williams, .P Pieranski, and P. E. Cladis. *Phys. Rev. Lett.*, 29(2):90, 1972.

[22] C.E. Williams, P.E. Cladis, and M. Kleman. *Mol. Cryst. Liq. Cryst.*, 21(3-4):355–373, 1973.

[23] S. Faetti. *Phys. Lett. A*, 237:264–270, 1998.

[24] M. Kleman and O.D. Lavrentovich. *Philos. Mag.*, 86(25-26):4117–4137, 2006.

[25] D. Melzer and F.R.N. Nabarro. *Philos. Mag.*, 35(4):907–915, 1977.

[26] A.D. Rey and M.M. Denn. *Annu. Rev. Fluid Mech.*, 34:233–266, 2002.

[27] A.M. Donald and A.H. Windle. *Liquid crystalline polymers.* Cambridge University Press, 1992.

[28] Z. Bradac, S. Kralj, M. Svetec, and S. Zumer. *Phys. Rev. E*, 67(5):050702, 2003.

[29] M. Svetec, Z. Bradac, S. Kralj, and S. Zumer. *Mol. Cryst. Liq. Cryst.*, 413:2179–2187, 2004.

[30] M. Svetec, S. Kralj, Z. Bradac, and S. Zumer. *Eur. Phys. J. E*, 20:71–79, 2006.

[31] G. De Luca and A.D. Rey. *J. Chem. Phys.*, 126:094907, 2007.

[32] A. Sonnet, A. Kilian, and S. Hess. *Phys. Rev. E*, 52(1):718–722, 1995.

[33] S. Kralj, E.G. Virga, and S. Zumer. *Phys. Rev. E*, 60(2):1858–1866, 1999.

[34] M. Zapotocky, P.M. Goldbart, and N. Goldenfeld. *Phys.Rev.E*, 51(2):1216–1235, 1995.

[35] T.J. Jankun-Kelly and K. Mehta. *IEEE Trans. Vis. Comput. Graph.*, 12(5):1045–1051, 2006.

[36] S. Kralj and E.G. Virga. *J. Phys. A*, 34:829–838, 2001.

[37] A.N. Beris and B.J. Edwards. *Thermodynamics of Flowing Systems.* Oxford University Press, 1994.

[38] G. Toth, C. Denniston, and J.M. Yeomans. *Phys. Rev. E*, 67:051705, 2003.

[39] B.J. Edwards and A.N. Beris. *J. Rheo.*, 33:1189–1193, 1989.

[40] A.G. Cheong and A.D. Rey. *Liq. Cryst.*, 31(9):1271–1284, 2004.

[41] L.M. Pismen and B.Y. Rubinstein. *Phys. Rev. Lett.*, 69(1):96–99, 1992.

[42] L. M. Pismen. *Vortices in Nonlinear Fields From Liquid Crystals to Superfluids, from Non-equilibrium Patterns to Cosmic Strings.* Clarendon Press, 1999.

[43] S. Kralj and E.G. Virga. *Phys. Rev. E*, 66:021703, 2002.

[44] J. Yan and A.D. Rey. *Phys. Rev. E*, 65:031713–1–14, 2002.

[45] J. Yan and A.D. Rey. *Carbon*, 40:2647–2660, 2002.

[46] J.C. Loudet and P. Poulin. *Top. Curr. Chem.*, 226:173–196, 2003.

[47] J.J. Feng and C. Zhou. *J. Colloid Interface Sci.*, 269:72–78, 2004.

[48] T. Yamamoto, Y. Tabe, and H. Yokoyama. *Thin Solid Films*, 509:81–84, 2006.

CHAPTER 8
General conclusions and original contributions to knowledge

8.1 General conclusions

This thesis explores the behavior of defects in engineering devices and biological processes involving nematic liquid crystal phases and contributes to their fundamental understanding. Three different types of defects are encountered and studied in this work: inversion walls, lines and points. These defects are studied using three different computational models which differ by their ability to describe singular defects as well as structural core details.

The inversion walls investigated in thesis occur in a thin nematic film found in a new electro-optical device, where it undergoes a sudden temperature-induced surface anchoring transition. The presence of these wall defects perturbs the light transmission properties of the device and therefore significantly alters its performances. The first question explored on this problem is: Is the creation of inversion wall defects a reversible process and is it possible to anneal them by tuning the temperature of the film? The answer is no. Our computational results and the experimental observations made in fluorescence confocal polarizing microscopy by our collaborators at Georgia Tech, which agree very well, show that once an inversion wall is created, modifying the temperature of the nematic film does modify the geometry of the defect but does not remove it from the system. Simulations clearly show that as the temperature of the film is raised and therefore anchoring strength decreased, the width of the wall

increases and extends throughout the film. On the other hand, when temperature is reduced and therefore anchoring strength increases, the width of the inversion wall shrinks and 'barrels' but does not completely disappear. The initially pure twist wall becomes a diffuse inversion wall. This phenomenon attributed to an energy storage mechanism is in agreement with previous theoretical predictions on the behavior of twist inversion wall defects by Ryschenkow and Kleman (1976). A practical implication of these results is that the design of the electro-optical device requires a very precise determination of the range of operating temperatures to avoid the formation and concomitant trapping of those irreversible defect structures. On the other hand it is also shown that when produced under controlled conditions, inversion wall defects can provide valuable information on the interfacial property of the nematic film which in turn are related to operating parameters like response time and switching voltage. Using basic variational calculations under the assumption of weak anchoring strength, it is shown that the width of the wall can be directly connected to the surface anchoring strength of the film through a simple model equation. This new relation captures well the non-linear behavior of the wall geometry and represents a significant improvement with respect to previous relations that were based on linear behavior and therefore were leading to error estimates of an order of magnitude.

The second type of defects studied in this thesis are points that are found periodically distributed along cylindrical cavities with sidewalls imposing homeotropic anchoring, as observed in the tubular extrusion duct of spiders. The presence of these defects in the spinning apparatus is deemed very important to silk processability and final mechanical properties but their emergence, behavior, and role is

unclear at present. Because in vivo observations of these defects in the spiders' abdomen is not yet possible and studying point defects in a controlled environment such as nematic-filled capillaries is still tedious, computational modelling provides an appealing alternative approach. A question of fundamental importance arising from the experimental observation of periodic distribution of these point defects is: Is there an equilibrium separation distance between the defects? In order to find a partial answer to this question, various scenarios of defect interactions are investigated. The first concerns the interaction between two point defects of opposite strength. Numerical results show that, in the absence of flow or geometrical effects (like capillary convergence), this interaction is always attractive. However, when the two defects are separated by more than a diameter, their speed of displacement is insignificant and they appear to be pinned to the capillary axis. On the other hand, when they are separated by less than a diameter and continue to approach each other their speed increases exponentially until they finally merge. The force of attraction follows a similar behavior. When two point defects of opposite strength eventually merge and annihilate they give rise to an escape structure free of any singularity. All these results are in agreement with experimental observations as well as the theoretical predictions reported in the literature. The second scenario investigated is the interactions between more than two defects. Here again, in the absence of external forces or geometrical effects or boundary effects it turns out that defects always attract and eventually mutually annihilate until producing an homogenous escape structure. These various results lead to the conclusion that if point defects effectively adopt an equilibrium distribution, external factors not taken into account

in the models used in this work must play a role.

The last type of defects encountered in this thesis is line defects, found in various industrial fibers involving nematic precursors. These line defects lead to various fiber textures and therefore various sets of mechanical properties. Understanding the way they form is crucial to control and optimize the product properties. Interestingly the textures found in industrial fibers never contain point defects as found during the processing of natural fibers. A question arising from this observation is: What are the possible topological connections between the textures found in industrial and natural fibers? In order to develop a partial answer to this question, the core details of point defects embedded in a cylindrical cavity are investigated. Simulation results show that point defect may in fact be, in reality, closed line defects or ring defects. In fact, according to our calculations point defects do not exist in cylindrical cavities if one considers core details. The far field molecular orientation of point and ring defects are however analogous. The importance of this detail resides in the fact that unlike point defects, ring defects offer the topological flexibility to mutate into the various other textures observed in industrial fibers. The ring-like nature of a point defect core presents therefore a fundamental connection between industrial and natural fiber textures. A natural reason why ring defects are not frequently experimentally observed is that their relatively small sizes prevent them from being resolved by any current observation techniques. Our calculations show that ring defects can be oriented with their axis along or perpendicular to the cavity axis. Ring defects with axis perpendicular to the cavity axis seem to be the most probable.

8.2 Original contributions to knowledge

The contributions of this thesis to original scientific knowledge are:

- A computational framework is developed to accurately model the geometric behavior of twist inversion wall defects occurring in thin nematic films following temperature induced surface anchoring transitions. The fundamental behavior of the wall defect is elucidated from simulations and show excellent agreement with experimental observations.
- A new, more accurate, model equation is derived to connect the geometry of the inversion wall defect to the surface anchoring strength of the nematic film.
- A computational model based on the tensorial Landau-de Gennes theory is for the first time employed to investigate the interaction between two point defects in cylindrical capillaries. The different stage of the annihilation process: pre-collision, collision, and post collision are thoroughly described.
- The interactions between multiple point defects along cylindrical tube are investigated for the first time with a model based on Frank elastic continuum theory.
- The prevalence of ring defects over 'true' point defects is demonstrated.
- The detailed structures of ring defects in cylindrical capillary are for the first time computed using three-dimensional simulations based on the Landau-de Gennes continuum theory.
- The topological transformations between the various structures found in industrial fibers and the one found along the spinning extrusion duct of spider are simulated and thoroughly described.

8.3 Recommendations for future work

In the future, this research can take various directions based on the results, developments and questions that have come about during the completion of this thesis.

With respect to the understanding of inversion wall defects in nematic thin films aimed at electro-optic devices, it would be, for example, interesting to develop a computational toolbox to complement the current computational model and be able to make direct comparisons with signals obtained from fluorescence confocal polarizing microscopy. Another interesting direction to be investigated would be the interactions between several inversion wall defects in the nematic film. The effect of elastic anisotropy on the geometry of the defect could also be interesting to explore.

With respect to the understanding of point defects in the cylindrical cavity in the context of spider silk processing, it could be interesting to include flow effects and examine how it affects the distribution of many interacting point defects. Inspecting the effect of the cavity convergence could also be fruitful. Another exciting, related, problem would be to examine the mechanisms of the emergence of point defects along the cavity: do they appear through a front propagation mechanism or emerge from nucleation and growth? Elastic anisotropy effects could also be wise to investigate. Finally, a phase separation model could be added to the current model.